UNIVERSITÀ
DEGLI STUDI
FIRENZE

PhD in
Earth Sciences

CYCLE XXXIII

Strain partitioning between border faults and axial magmatic segments in the Afar Rift

Doctoral Candidate
Alessandro La Rosa

Supervisor
Prof. Carolina Pagli

Co-Supervisors
Prof. Derek Keir

Prof. Federico Sani

Coordinator
Prof. Francalanci Lorella

Years 2017/2020

Contents

Abstract

Continental break-up is a key stage of the rifting process as it marks the transition to ocean seafloor spreading. Predictive models of the rift-to-seafloor spreading transition suggest that, during incipient continental break-up, the rift margins deactivate and extension focuses at the rift axis along a series of en-echelon magmatic segments which are offset by either transform or non-transform faults. However, how strain is partitioned between the rift margins and axial magmatic segments during the last phases of the rifting process remains poorly understood. Furthermore, how and when transform and non-transform offsets form during the rifting process is still unclear. Northern Afar, in the East African Rift System, is the ideal place to address these open questions as it shows these processes occurring during the final stages of continental rifting exposed at surface. In this thesis, I adopted a multi-disciplinary approach based on InSAR, seismicity and structural analyses to investigated the tectonic deformation and the fault kinematics at the offset between the two axial magmatic segments of Erta Ale and Tat'Ali (Afrera Plain) and also along the North-Western Afar Margin.

The results show that the Afrera Plain is an active rift-linkage zone characterized by en-echelon, oblique, left-lateral faults striking in a ~NS direction. The structural architecture of the Afrera Plain is characterized by dominant East-dipping faults at the center and dominant West-dipping faults at the eastern tip, close to the Tat' Ali segment. Such structural architecture is consistent with a kinematic model of rift-linkage where Erta Ale and Tat' Ali segments interact trough a right-lateral transfer zone characterized by en-echelon oblique faults, striking in a ~NS-direction. Furthermore, InSAR time-series and models, combined with seismic data, have revealed great variability in the fault behavior. Faults at the center of the Afrera Plain are characterized by dominant stick-slip faulting with episodic slip events accompanied by $M_L \geq 5$ earthquakes. Conversely, a more complex fault behavior encompassing creep, micro-seismicity and episodic slip characterize the tips of the linkage zone. Such heterogenous fault behavior could be likely influenced by the high heat flows and the strong hydrothermal circulation at the Afrera Plain.

Intense seismicity also characterizes the North-Western Afar Margin. Here ongoing tectonic extension along active border faults generate moderate seismicity with several $M_w > 5$ earthquakes occurred in the past decades. Recently, a M_L 5.3 seismic sequence occurred in

March-April 2018 rupturing the deep portion (15-30 km) of crustal border faults. The analysis of focal mechanism and relocated seismicity shows that slip occurred along major West-dipping faults and minor conjugate East-dipping faults. The fault kinematics has dominant normal component associated with both minor left- and right-later components. Deep seismicity in the area is focused below the Dergaha marginal graben where there is geophysical evidence of partial melt in the lower crust. Such observations suggest that deep seismicity along the North-Western Afar Margin could be triggered by fluids migration in the lower crust associated with magmatic processes. Conversely, seismicity outside the Dergaha graben is shallower (< 15 km) and likely associated to brittle faulting in the upper crust.

The results of this thesis provide one the few direct observations of the tectonic processes occurring at the interaction between two magmatic segments in Afar. Furthermore, they provide new contributions towards the understanding of the kinematic of rift margins in Afar during incipient continental break-up suggesting that fluid migration in the crust may play a role in influencing the fault activity along the North-Western Afar Margin.

1. Introduction

The rifting of continents is a key stage in the plate tectonic cycle as it can cause the break-up of continents and eventual formation of new oceans. As two plates separate, thinning of the lithosphere by brittle normal faulting and ductile stretching (McKenzie, 1978) induces decompression melting of the asthenospheric mantle and upwelling of magma. The buoyant magma is intruded in the lithosphere and erupted at the surface assisting tectonic extension (White & McKenzie, 1989). The magmatism accommodates extension and also modifies the composition and thermal structure of the lithosphere (e.g. Mackenzie et al., 2005; Maguire et al., 2006; Hammond et al., 2011). In the final stages of rifting the continental lithosphere is broken and extension is focused to narrow magmatic segments that are linked by transform faults. However, key unknowns are how and when strain migrates and localizes at the segmented zones of extension, and also how strain is partitioned between the rift margins and the axis as continental rifting progresses to continental rupture. Furthermore, transform zones have long been observed to connect mid-ocean-ridge segments (Wilson, 1965; Macdonald et al., 1988; Grindlay et al., 1991; Wetzel et al., 1993), yet how discrete extensional segments interact during the previous rifting stage, as also the formation and fault kinematics of transform zones remain unclear.

In the last few decades, the study of active spreading centres, such as the Afar continental rift in East Africa and the Iceland oceanic ridge has strongly improved our knowledge of rifting processes. A wide and still growing body of geophysical, geological and geodetic observations has been allowing scientists to better understand how extensional plate boundaries evolve (e.g. Sigmundsson, 2006; Einarsson, 2008; Wright et al., 2006; Wright et al., 2012; Metzger et al., 2013; Metzger and Jonsson; 2014; Green et al., 2014; Pagli et al., 2014; Drouin et al., 2017; Pagli et al., 2018; Drouin & Sigmundsson 2018; Sigmundsson et al., 2015, 2020a, 2020b). It has been shown that, during the first stages of continental rifting, mechanical extension occurrs along large-offset border faults which bound the shoulder of the forming rift floor (e.g. Ebinger et al., 1993; Modisi et al., 2000). As plate stretching proceeds and magma enters the system, the extension migrates along a series of axial magmatic segments. The border faults progressively deactivate turning to passive margins (e.g. Hayward & Ebinger, 1996; Wolfenden et al., 2005; Ebinger, 2005; Corti, 2009, 2012) while the magmatic segments accommodate extension through major

diking episodes similar to those occurring at mid ocean ridges (e.g. Sigmundsson, 2006; Wright et al., 2012; Sigmundsson et al., 2015, 2020a). However, recent seismic surveys at mature continental rifts have shown intense seismicity characterizing rift margins during incipient break-up (e.g. Keir et al., 2006; Illsley-Kemp et al., 2018a). This posed questions about the timing of fault deactivation, the causes of seismicity, and the related seismic hazard at the rift margins.

Magmatic segments also grow and link, playing a key role in the geometry of the rift axis (e.g. Corti, 2008; Green et al., 2014; Illsley-Kemp et al., 2018b; Pagli et al., 2018). In Iceland, geodetic and seismic data provided new insights on a variety of rift linkage mechaninsms. In the South Iceland Seismic Zone, through shear along strike-slips faults subparallel to the volcanic rift zones were detected seismically and in the field and in the '80s, these observations led to the birth of the "bookshelf" linkage model (Einarsson et al., 1981; Einarsson, 2010), which has also been invoked more recently to explain rift linkage in the Northern Volcanic Zone (e.g. Green et al., 2014; Drouin et al., 2017). Conversely, complex transform zones with both extensional and strike-slip motions were observed to form in the Tjiornes Fracture Zone of Northern Iceland, when plate divergence acts obliquely to the spreding centers (Einarsson, 2008). InSAR, GPS and seismic studies have been also carried out to investigate rift linkage processes in Afar (e.g. Sigmundsson, 1992; Doubre et al., 2017; Pagli et al, 2018). However, there are still several open questions about the mechanisms of interaction between magmatic segments in Afar: The fault kinematics of linkage zones is poorly understood and it is not clear if and when transform faults form (e.g. Pagli et al., 2015; Doubre et al., 2017; Illsley-Kemp et al., 2018b; Pagli et al, 2018).

Investigating the strain partitioning between the border faults and the axial magmatic segments is thus key for understaning the kinematics of rifting during its final stages. Northern Afar, which is believed to represent the incipient stage of continental break-up, is the perfect study area as it shows rifting processes exposed at the surface. In this thesis, I analysed the ongoing deformation at the offset between two axial magmatic segments and across the North-Western Afar Margin by using InSAR and seismicity, and by comparing these results to structural geology. I performed InSAR analysis of the Afrera Plain in the rift axis, by studying an episodic fault slip in 2007 and doing inverse modelling of co-seismic deformation and combining this with structural measurements and seismicity (Chapter 3). My results showed that the Afrera Plain is an active transfer zone. Then, in order to

understand the plate-boundary kinematics of the entire transfer zone, I did a multi-interferogram analysis producing time-series of incremental deformation and average maps of surface velocity using the vast catalouge of ENVISAT and Sentinel-1 data from 2005 to 2019 (Chapter 4). I also studied the defomation of the North-Western Afar Margin using seismicity and analisys of focal mechanisms to understand the kinematics of faulting and its causes (Chapter 5).

1.1 The East African Rift System

During the last 40-45 Ma, plate divergence has been tearing apart the Eastern African continent. Faulting and magmatism are widespread across the East African Rift System (EARS) from the Red Sea and Gulf of Aden Rifts, all the way to the Okavango Rift (Figure 1.1) (McKenzie et al., 1970). Continental rifting in EARS developed above a topographically elevated region characterized by low seismic velocities in the upper mantle, negative Bouguer gravity values and strong volcanic activity, which have been explained with the presence of one (or multiple) mantle plume(s) emplaced beneath the African continent (e.g. White & McKenzie, 1989; Ebinger & Sleep, 1998; George et al., 1998; Rooney et al., 2012). Following the impingement of the mantle plume below the current Afar region ~ 30 Ma ago, rifting initiated with the approximately coeval opening of the Gulf of Aden and Red Sea rifts and the separation of the Arabian Plate, likely assisted by tensional stresses imposed by the slab-pull below the Arabian-Eurasian convergent margin (Wolfenden et al., 2005; Leroy et al., 2010; Koptev et al., 2018). During the Miocene (~11 Ma), tectonic extension started along the northern sector of the EARS, known as Main Ethiopian Rift (MER), due to the separation of Somalia from the Nubian Plate (Wolfenden et al., 2004, 2005). Plate divergence then propagated southward across the EARS through the diachronous opening of the Eastern, Western Branches, Malawi and Okavango Rifts (Figure 1.1) (Ebinger, 2005). The diachronous onset of extension in the EARS allows scientists to observe at the surface the different stages of continental rift development.

Figure 1.1 shows the main rift segments currently active across the EARS. The Okavango Rift in Botswana is the youngest section of the EARS where incipient continental extension occurs through normal faulting along poorly developed half-grabens and without evidence of magmatic activity (Modisi et al., 2000). To the North, the Malawi rift has a similar half-graben architecture bounded to the East by major high-angle border faults and accompanied by volcanic activity at the Northern tip, close to the Wester Branch (Ebinger et

al., 1993). The latter is still characterized by dominant mechanical extension focused along well-developed normal border faults cross-cutting a strong intruded continental crust (Ebinger et al., 1991). In the Western Branch, faults activity generated hundreds of kilometers-long grabens filled by lakes (e.g. Lake Tanganyika) and showing anomalously deep seismicity at the base of the lower crust (Shudofsky, 1985; Albaric et al., 2009; Lavayssière et al., 2019). A more evolved phase of continental rifting is observed at the Eastern Branch. Increased magmatism and shallower seismicity characterize the ~8 Ma North Tanzania-South Kenia rifts where extension is accommodated along the border faults but also along younger fault systems within the grabens (Ebinger, 2005; Le Gall et al., 2008). The northward increase in magmatic activity is accompanied by the progressive decrease in crustal thickness suggesting that magmatism is an important mechanism for accommodating crustal extension in this region (Ebinger, 2005).

The MER represents a mature continental rift stage. Large border faults separate the rift floor from the uplifted Ethiopian and Somalian plateaus yet divergence between Nubia and Somalia is mainly accommodated across Quaternary-Recent, ~60 km-long, en-echelon, axial magmatic segments, striking in ~NE direction (Boccaletti et al., 1998; Ebinger & Casey, 2001; Corti, 2008). Recent GPS measurements across the MER show eastward horizontal movements of Somalia with respect to Nubia at velocities of ~6 mm/yr (Birhanu et al., 2016). The 80% of the full spreading velocity is currently accommodated at the rift axes while the other 20% is accommodated at the margin. A combination of geochemical and seismic data has shown the presence of great amounts of melt beneath the MER feeding systems of dikes and alignments of volcanoes within the magmatic segments, suggesting that dominant magmatism and diking at the rift axis accommodate plate divergence (Keir et al., 2006; Keir, Hamling, et al., 2009). The dominant magmatism and the rift-architecture of the rift segments, indicate that the MER represents a phase of ongoing break-up before the inception of seafloor spreading.

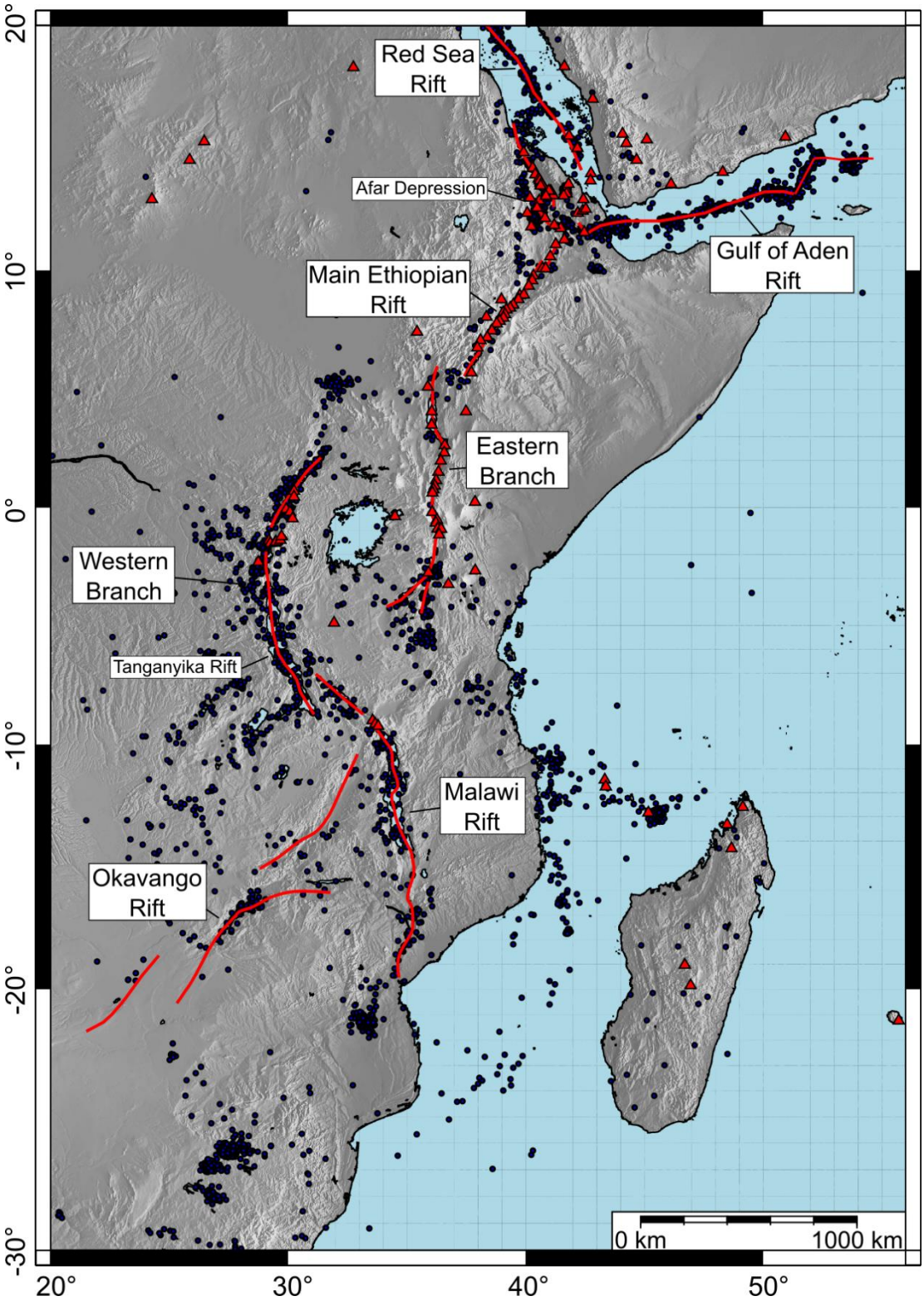

Figure 1.1 – The East African Rift System. The red solid lines represent the main rift branches. The red triangles are the Holocene volcanoes (Volcano Discovery project, https://www.volcanodiscovery.com) while the blue dots are the Mw > 4.5 earthquakes between 1950-2017 (USGS-NEIC earthquake catalogue, https://earthquake.usgs.gov/earthquakes).

Geological and geophysical studies at the EARS have been also accompanied by several experimental studies investigating the time-evolving kinematics of continental rift systems with a focus on the factors controlling their architecture at different stages (e.g. Allken et al., 2012, 2013; Corti, 2008, 2012; Gerya, 2013a; 2013b; Philippon & Corti, 2016; Le Pourhiet et al., 2017). In particular, lithospheric-scale models reproducing narrow rift systems (as the EARS) showed how the border faults acting during the first stages can be segmented and connected by transfer zones characterized by complex patterns of oblique- and strike-slip faults, transferring extension between the adjacent border fault segments (Corti, 2012). The along-axis segmentation can persist during the mature stages when extension migrates to the rift axis along systems of en-echelon magmatic segments (Figure 1.2). Linkage zones between magmatic segments ranges in width from a few tens to hundreds of kilometers and can show a great variety of structural architectures encompassing proto-transform faults (e.g. Gerya, 2013), book-shelf faults (e.g. Einasson, 1981; Mandl, 1987;. Einarsson, 2008; Green et al., 2014) or transfer zones with oblique faulting (e.g. Corti, 2008, 2012; Allken et al., 2011, 2013; Le Pourhiet et al., 2017) (Figure 1.3). The architecture of rift linkage zones, as also their possibility to evolve to transform margins, have been suggested to be influenced by several factor encompassing pre-existing weaknesses, rift obliquity with respect to the extension direction, width of the linkage zone and degree of overlap between magmatic segments (e.g. Corti, 2008, 2012; Brune et al., 2017).

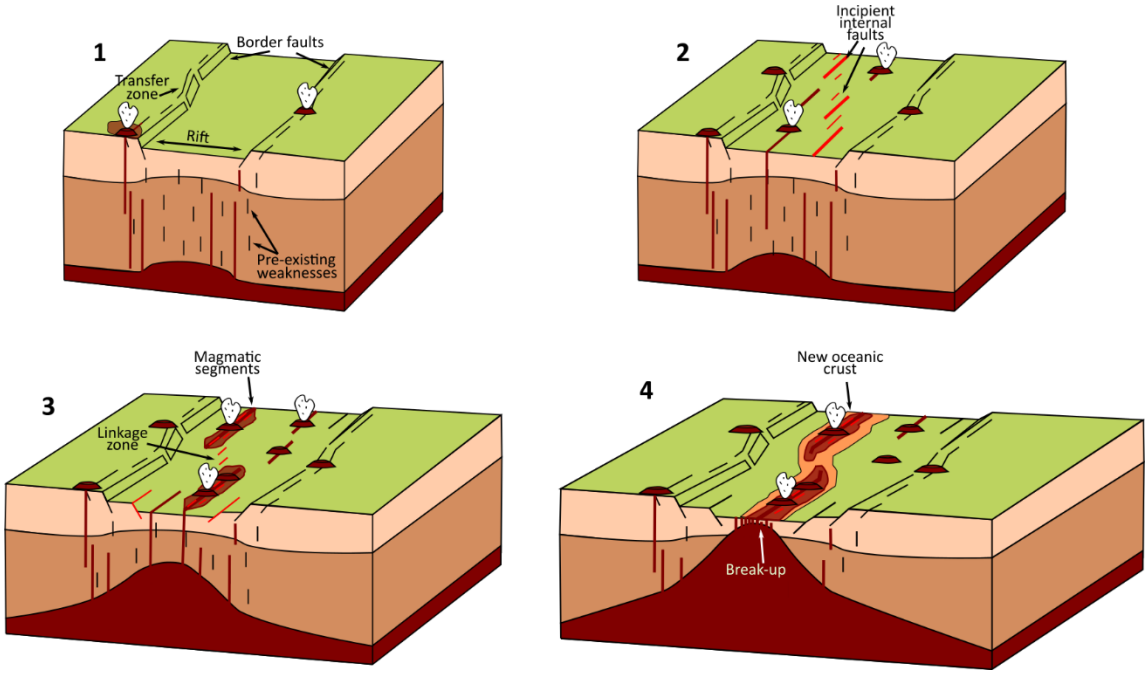

Figure 1.2 – Model of continental rifting. Various stages of the rifting evolution can be observed from 1 to 4 (modified from Corti, 2012). Stage 1 is the rift initiation with extension accommodated along border faults. Stages 2 and 3 are intermediate stages with extension increasingly accommodete at the axis by magmatic segments at stage 3. Stage 4 is the break-up and the inception of seaflor spreadig.

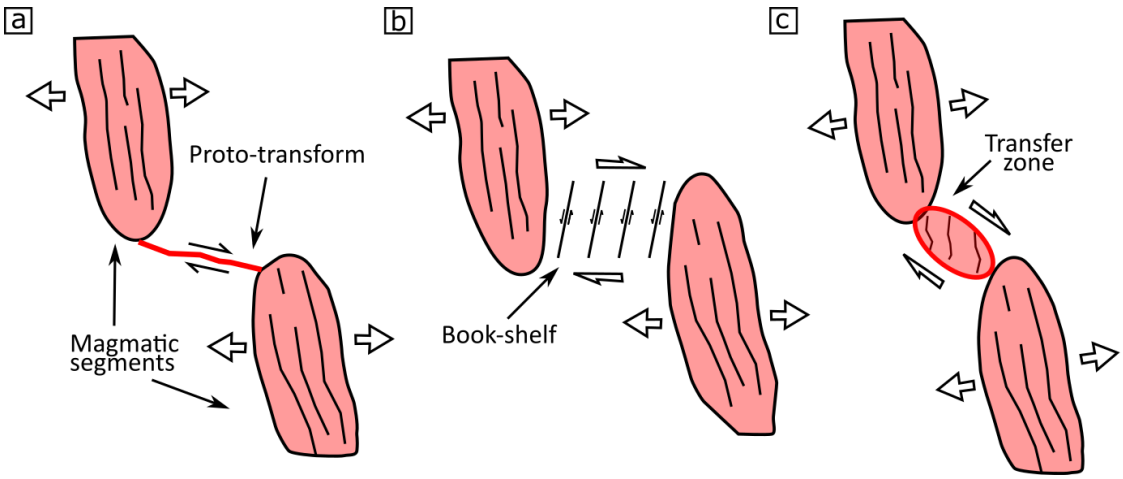

Figure 1.3 – Simplified sketches of rift linkage types. a) Proto-transform fault modelled by Gerya (2013). b) Book-shelf faulting as observed in Iceland by Green et al. (2014). Transfer zone characterized by internal oblique faults as observed along the MER by Corti (2012).

1.2 Rifting in Afar

The Afar depression results from the divergence of Nubia, Arabia and Somalia along the Red Sea, Gulf of Aden, and Main Ethiopian rift arms which meet in Afar, forming a rift-rift-rift triple junction (Barberi & Varet, 1970; Beyene & Abdelsalam, 2005) (Figure 1.4). Following the impingement of the mantle plume at ~30 Ma, extension began across the Southern Red Sea and Gulf of Aden rift arms. The on-land propagation of these two rift arms in Afar have been causing the separation of a micro-plate, known as Danakil Block, and the opening of the Danakil depression (in Northern Afar) and the Central Afar (Figure 1.4) (e.g. Eagles et al., 2002; McClusky et al., 2010; Stab et al., 2016). To the South, the development of the Northern MER during the last ~11 Ma also occurred (e.g. Tesfaye et al., 2003) (Figure 1.4). It is suggested that the Northern MER is separated from the other Red Sea and Gulf of Aden rift arms by an oblique fault system, the Tendaho-Goba'ad Discontinuity (TGD), striking NW-SE and marking a change in the extension direction and plates' kinematics within the different sectors of Afar (Tesfaye et al., 2003; Acocella et al., 2008) (Figure 1.4).

Kinematic models from GPS data collected for the Northern Afar indicate current extensional rates increasing from ~7 mm/yr, at N16°, to ~20 mm/yr at 13°N and directed ~N60°E (Figure 1.4a) (McClusky et al., 2010). Similar velocities and direction characterize extension in Central Afar (Doubre et al., 2017) while lower extensional rates of 3-5 mm/yr, directed ~N90°E, have been measured in Southern Afar (Birhanu et al., 2016) (Figure 1.4a).

Since ~30 Ma, the beginning of extension in Afar was accompanied by diffuse volcanism across the Ethiopian and Somalian plateaus, with the emplacement of the Trap Series, a 2 km-thick sequence of basalts and rhyolites (Trap Series) that covers today a ~600.000 km^2-wide area of the Ethiopian and Somalian plateaus (Figure 1.5) (Hofmann et al., 1997; Kieffer et al., 2004). Tectonic extension accompanied volcanism and focused along large-scale border faults which bound today the depression to the West and Southeast, marking the transition from the rift valley to the Ethiopian and Somalian plateaus (Figure 1.4 and 1.5) (Beyene & Abdelsalam, 2005). Since ~25 Ma, extension has been migrating from the Afar rift margins to the rift axis (Beyene & Abdelsalam, 2005). Such migration was also accompanied by the migration of magmatic and volcanic activity (Lahitte et al., 2003). The Trap basalts were followed by the eruption of the Mabla rhyolites

basalts (16-9 Ma) which today outcrop just South of the Gulf of Tadjoura (Varet, 1978; Vidal et al., 1991) and at the Danakil Block (Figure 1.5). The eruption of the Dahla basalts followed at 8-6 Ma, outcropping today at the at the Western Afar Margin (WAM), at the Danakil Block, and South of the Gulf of Zula (Figure 1.4 and 1.5). Since then, magmatism focused mainly at the axis with a series of basaltic fissural eruptions that produced a ~1.5 km-thick sequence of lava flows, known as Stratoid Series, which covers a ~55.000km^2 - wide area across the Afar depression (Varet, 1978) (Figure 1.5). Barberi et al. (1975) dated the Stratoid Series between 4.4 and 0.4 Ma while recent-most studies suggest an age between ~3-1 Ma (Kidane et al., 2003; Lahitte et al., 2003). In Afar extension and magmatism currently occur along a series of < 1 Ma old (Lahitte et al., 2003), ~NNW-SSE-striking, ~70-km-long en-echelon magmatic segments (Figure 1.4b and 1.5). In the on-land Southern Red Sea two main axial magmatic segments are currently active: the Erta Ale and Tat'Ali segments (Figure 1.4b and 1.5). The axes of these segments are characterized by small-offset faults across an ~30-km wide area, along with eruptive fissures and alignments of basaltic and rhyolitic volcanoes (Barberi & Varet, 1970; Barberi et al., 1972; Keir et al., 2013; Wolfenden et al., 2004) (Figure 1.4b and 1.5).

Continental extension at the magmatic segments occurs through rifting episodes when major dyke intrusions and eruptive episodes accompanied by faulting occurs over relatively short periods of times, 1-10 years, and then it decays over time-scales of years to decades (e.g. Vigny et al., 2007; Ebinger et al., 2010; Wright et al., 2012; Pagli et al., 2014; Sigmundsson et al., 2015). These events have been first documented in Iceland between 1975-1984 when twenty diking episodes and nine eruptions extended the crust by ~9 m at the Krafla fissure swarm (Krafla Fires) (e.g. Brandsdóttir & Einarsson, 1979; Einarsson & Brandsdóttir, 1979; Tryggvason, 1984; Opheim & Gudmundsson, 1989). In Afar, the first documented rifting episode occurred at Asal-Ghoubbet in 1978 (e.g. Ruegg & Kasser, 1987; Ruegg et al., 1979). More recently, a major rifting episode occurred at the Dabbahu–Manda–Harraro magmatic segment, during 2005–2011. Such episode has been monitored by combining a dense seismic network, GPS, InSAR and field observations (e.g. Ebinger et al., 2008; Hamling et al., 2009; Keir et al., 2009; Belachew et al., 2011; Wright et al., 2012; Pagli et al., 2014) which provided the first comprehensive view on the dynamics of magmatic segments in a continental rift.

In the Danakil depression, eruptions and intrusions also occurred on several active volcanoes of the Erta Ale rift segment in recent years. A dyke intrusion with subsidence of the central Dallol proto-volcano occurred in October 2004 in Northern Afar (Nobile et al., 2012). In November 2008 an eruption occurred in the Alu-Dalafilla segment (Pagli et al., 2012) and in January 2017 the Erta Ale lava lake experienced an eruption lasting until June 2019 (Xu et al., 2017; Moore et al., 2019).

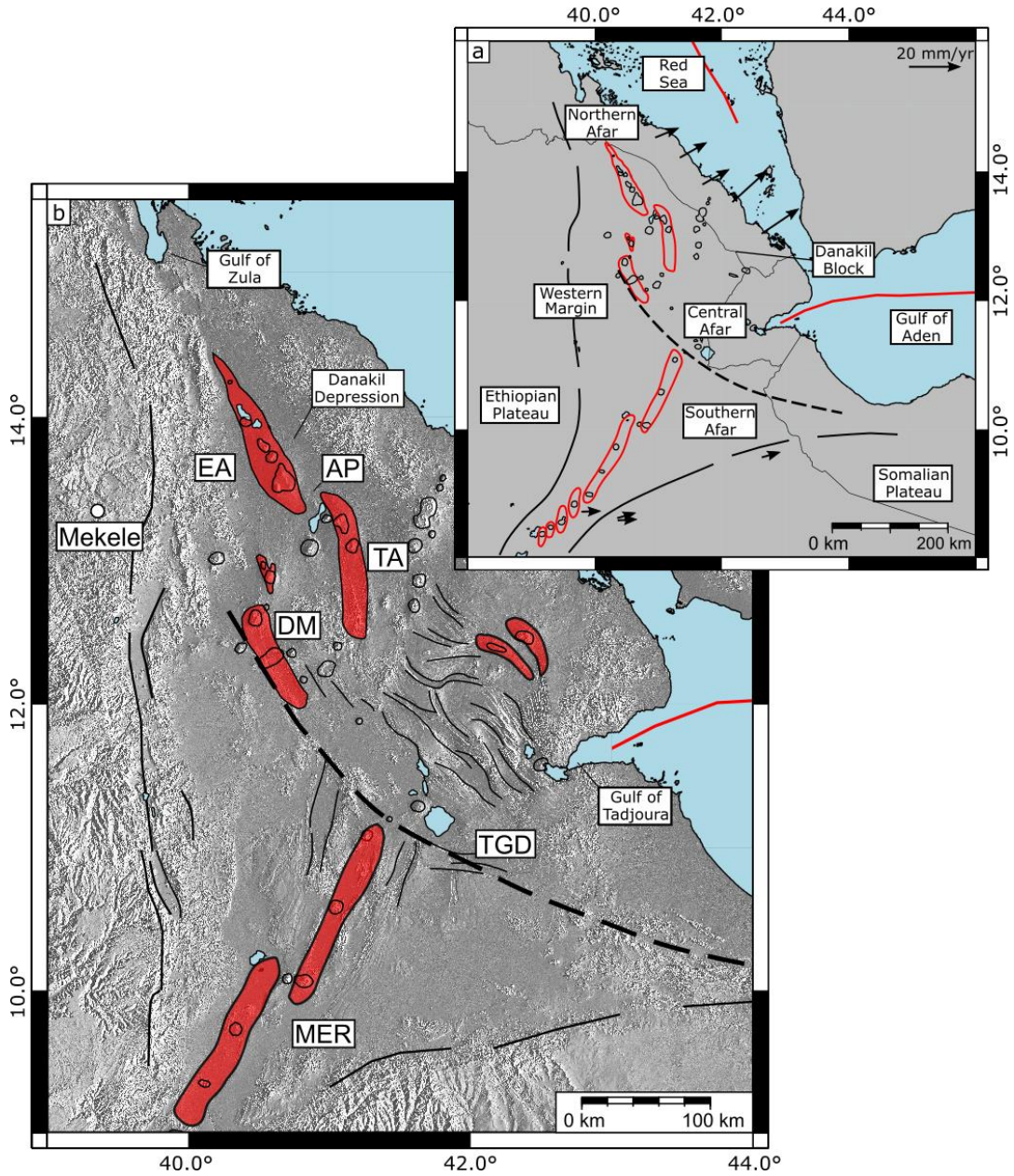

Figure 1.4 – Tectonic Setting of Afar. Solid black lines are the major faults while the axial magmatic segments are highlighted in red. The black dashed line represents the Tendaho-Goba'ad-Discontinuity (TGD). Black arrows are GPS velocities from McClusky et al. (2010) and Birhanu et al. (2016). EA = Erta Ale segment, AP = Afrera Plain, TA = Tat'Ali, DM = Dabbahu-Manda-Harraro, MER = Main Ethiopian Rift.

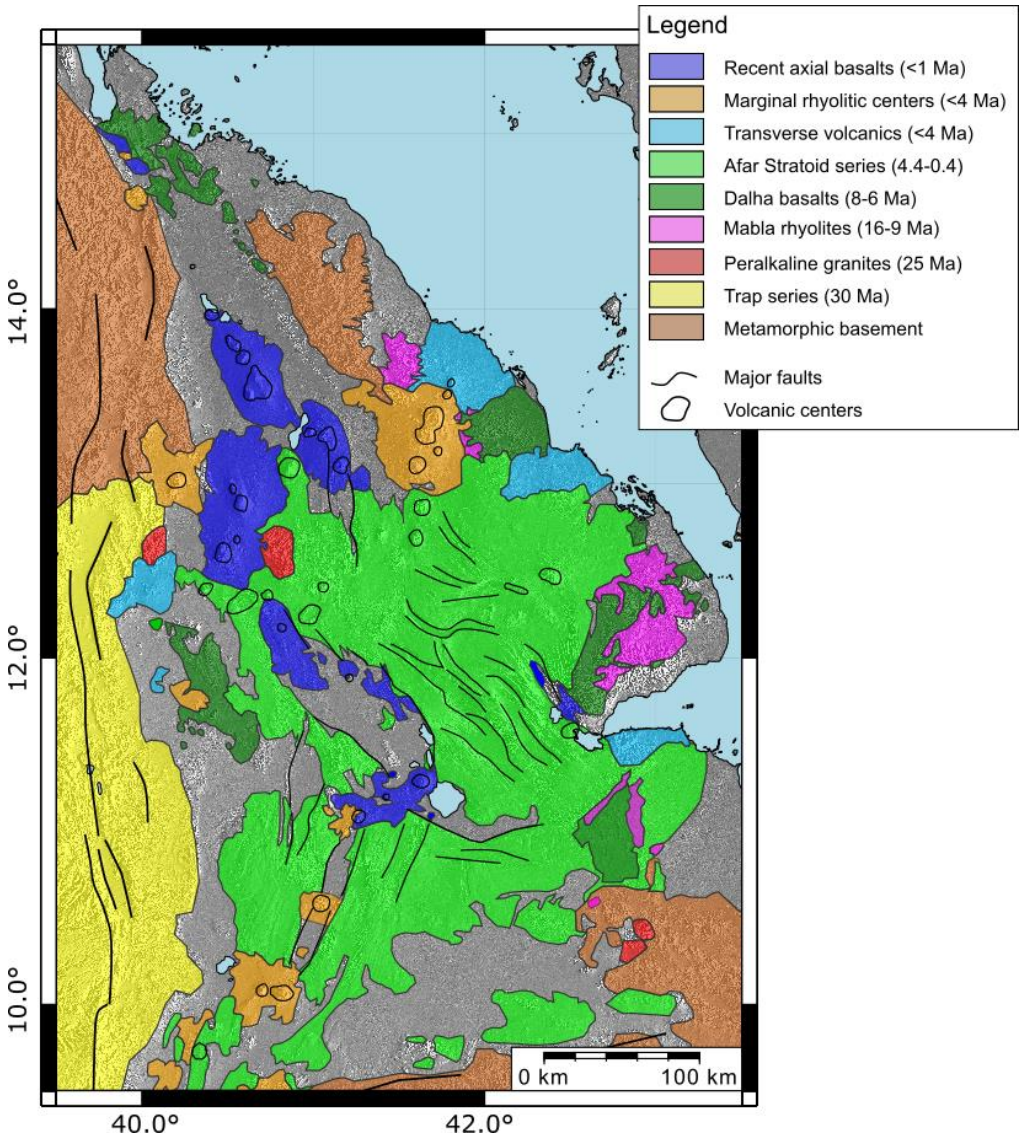

Figure 1.5 – Simplified geological map of the Afar depression (modified from Varet, 1978 and Stab et al., 2016). The Stratoid Series widely outcrops in Afar marking the migration of magmatism at the axis. It is also evident how the most recent magmatic and volcanic activity, highlighted in blue, is focused along the active magmatic segments.

The continental crust in Afar has been deeply modified by thinning, extension and magma intrusions (Figure 1.6). Seismic studies by Makris & Ginzburg (1987), Maguire et al. (2006) and Hammond et al. (2011) highlighted strong differences in crustal properties below different sectors of the Afar depression. In Northern Afar (North of N13°), the crust thins eastward from ~38 km below the Ethiopian plateau to ~16 km beneath the Danakil depression. An abrupt lateral thinning has been observed at the WAM at ~E39.5° where thickness decreases to < 20 km across a distance of 30 km (Hammond et al., 2011). Conversely, at latitudes of ~N11°, the crust below the plateau is thicker (~40 km) and gradually thins eastward to ~20 km at E40°. The crustal thinning in Afar is accompanied

by strong variations in Vp/Vs and topographic elevations. Low Vp/Vs ratios (1.7-1.8) characterize the thick felsic crust at the plateau which also show the highest elevation (2-3 km above the sea level). The crustal thinning at the WAM is mirrored by a decrease in topographic elevation toward the rift valley caused by the activity of the border fault systems. Similarly, progressive crustal thinning and decreasing elevation toward the rift axis characterize the rift floor which reaches minimum elevations between 50-100 m below sea level at the Danakil depression. High Vp/Vs ratios (1.9-2.0) across the WAM and the rift valley have been interpreted as related to melt and fluids emplaced in a mafic crust (Hammond et al., 2011).

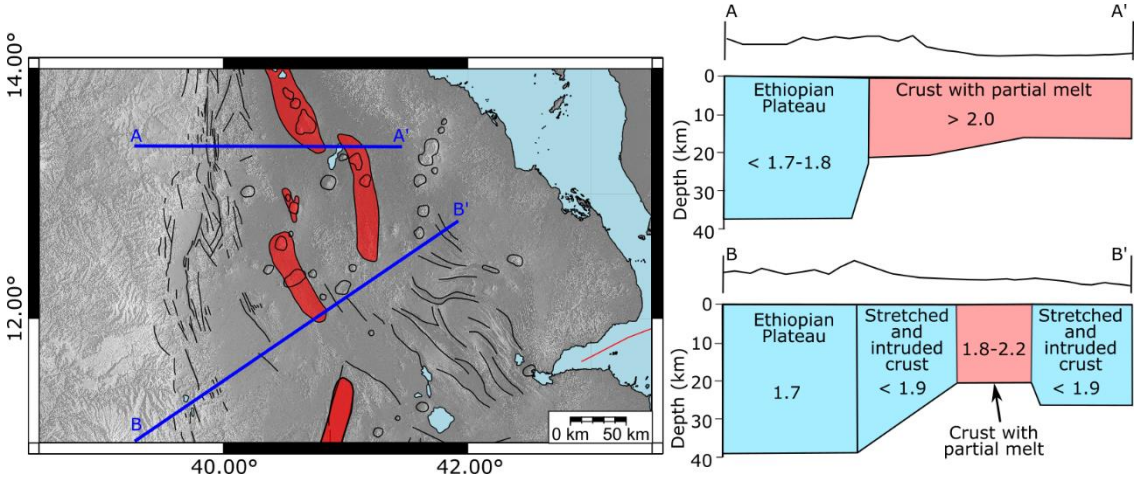

Figure 1.6 - Simplified profiles displaying the crustal structure and the relative Vp/Vs ratios across the Norther and Central Afar (modified from Hammond et al., 2011).

1.3 Current strain distribution in Afar

During the last decades, seismicity and InSAR have probed the distribution and magnitude of strain in Afar. In particular InSAR has been succesfully used to investigate rift segments in Afar with unpreceded temporal and spatial detail (e.g. Ebinger et al., 2008; Ebinger et al., 2010; Keir et al., 2011; Wright et al., 2012; Pagli et al., 2014). Seismic recordings from both temporary and global seismic stations were combined (Figure 1.7) to show the cumulative seismic moment release across Afar between 1950 and 2017. Figure 1.7 shows that a great amount of the seismic moment is released at the rift axes, across the Southern Red Sea and Gulf of Aden Rifts, indicating that these areas accommodate the majority of deformation in Afar. In the Southern Red Sea, seismicity clearly focuses along the Erta Ale, Tat'Ali and Dabbahu- Manda-Harraro segments according to a right-stepping geometry. Similarly, the seismicity distribution marks the active segments South of N12° highlighting the junction between the Southern Red Sea, the Gulf of Aden rifts and MER.

In the Northern Afar, the highest seismicity is observed at Dabbahu-Manda-Harraro during the diking episode of 2005-2009 (e.g. Ebinger et al., 2008; Belachew et al., 2011) while the high cumulative seismic moment release at the Nabro volcano corresponds to the eruption of June 2011 (Hamlyn et al., 2014; Goitom et al., 2015). Excluding these two episodic events from the seismic moment release in Afar, two other areas show intense seismic activity: The North-Western Afar Margin (NWAM), between N13°-N14°, and the offset between the Erta Ale and Tat'Ali segments, also known as Afrera Plain. Seismic activity is characterized by events with Mw > 5.0 accompanied by continuous low earthquakes (e.g. Ayele et al., 2007; Illsley-Kemp et al., 2018a), indicating ongoing deformation in these two areas. Furthermore, Illsley-Kemp et al. (2018b) used seismicity combined with InSAR and GPS derived strain maps to show high shear at the Afrera Plain, which they explain as evidence of an incipient WNW-ESE-striking, right-lateral transform fault.

Anomalously deep seismicity has been observed at the NWAM (USGS National Earthquake Information Center (USGS-NEIC); Belachew et al., 2011). Sparse moderate earthquakes have been also reported by global catalogs elsewhere across the WAM, between N10° and N12° (NEIC; Craig et al., 2011), yet the lower seismic activity compared to the Northern sector is likely related to a poor seismic networks coverage (Illsley-Kemp et al., 2018a; Zwann et al., 2020a). The intense seismicity in the NWAM and at the Afrera Plain and the large volume of available data have made these two regions the best candidate to investigate the tectonic activity of border faults and the mechanisms of interaction between rift segment during incipient continental break-up.

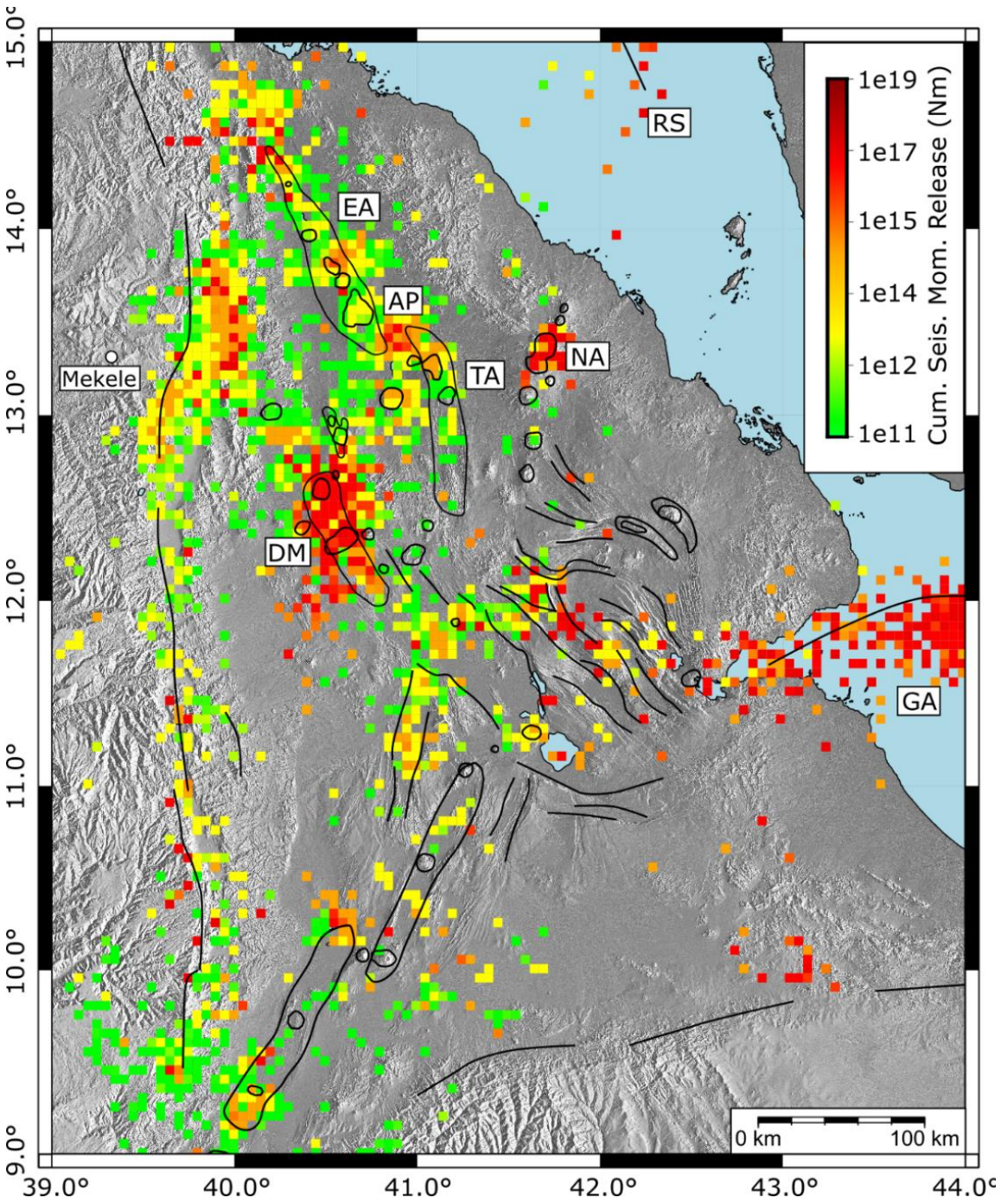

Figure 1.7 – Map of the cumulative seismic moment release during 1950-2017. The binning of the map is 0.05° in both latitude and longitude, corresponding to a pixel size of ~20 km^2. Seismicity is from both global and local catalogues (NEIC, Belachew et al., 2011, Illsley-Kemp et al., 2017). RS = Red Sea Rift, EA = Erta Ale segment, AP = Afrera Plain, TA = Tat'Ali, DM = Dabbahu-Manda-Harraro, GA = Gulf of Aden rift, NA = Nabro volcano, MER = Main Ethiopian Rift.

2. Data and Methods

In this chapter I provide a description of the methods and datasets used in this thesis. I first present the InSAR technique, with a focus on the multi-interferogram methods and the software used. A description of the seismic methods and dataset follows, with details on the seismic network and seismic velocity model used for earthquake location.

2.1 Interferometric Synthetic Aperture Radar (SAR)

Synthetic Aperture Radar (SAR) is radar system, mounted on satellites or other platforms, that emits an electromagnetic signal directed towards the Earth and is able to precisely determine the distance to a target on the surface of the Earth. In particular, SAR systems are imaging radars that measure the phase and amplitude for each pixel in the illuminated area by the radar footprint and therefore producing an image (Massonnet & Feigl, 1998; Hanssen, 2001; Simons & Rosen, 2007; Ferretti et al. 2007). SAR is an active system equipped with its own energy source for emitting a signal that can obtain measurements irrespective of weather conditions and daytime. Furthermore, SAR systems use sensors in the microwave frequency band, hence avoiding the attenuation of electromagnetic waves in the atmosphere (Massonnet & Feigl, 1998; Hanssen, 2001; Simons & Rosen, 2007).

A sketch of an imaging radar mounted on a satellite is shown in Figure 2.1. SAR is a side-looking system where the antenna is mounted on a moving platform (the satellite) and the signal is transmitted at right angles to the direction of flight and directed towards the Earth (Figure 2.1). In a SAR satellite the flight path defines the *azimuth direction* while the antenna sends a signal along the direction perpendicular to the flight path (*slant range*) with an inclination θ (*look angle*) with respect to the vertical (Figure 2.1a). The transmitted signal power is partially absorbed by the ground and partially scattered in different directions. A part of the transmitted signal is scattered back to the antenna, where the amplitude and phase are measured (Ferretti et al. 2007).

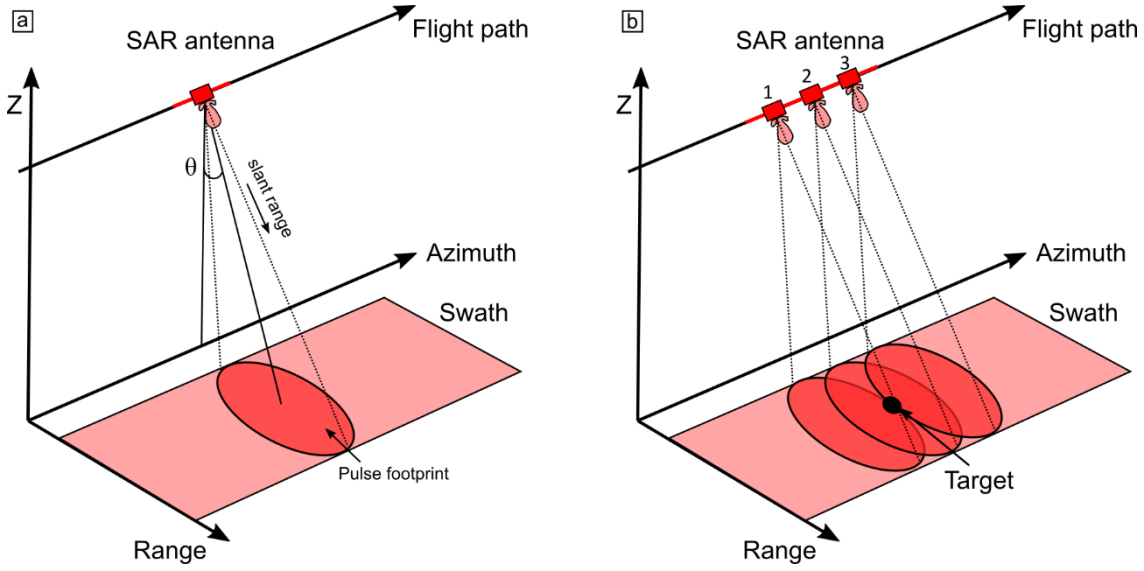

Figure 2.1 – a) Scanning geometry for a right-looking SAR system (modified from Simon & Rosen, 2007). b) Target positioning by exploiting the Doppler effect due to the relative motion between the target and the antenna.

SAR systems illuminate the Earth's surface by transmitting a series of electromagnetic pulses at a certain *Pulse Repetition Frequency* (PRF). The spatial resolution of SAR systems along the range and azimuth directions is controlled by several factors encompassing the pulse duration and the antenna length. Two targets can be discriminated along the range just if they are separated by a distance which is greater than half a pulse length (Dzurisin & Lu, 2007). The shorter the pulse length, the higher the resolution. However, pulses with short length cannot reach targets located at long distances. To get the finest resolution in range direction and preserve the energy content of the pulse, the SAR signal is modulated by increasing the frequency during the time period of the pulse (Hein, 2004). Such process, known as *range compression*, generates short pulses characterized by a quadratic phase progression, called *chirps* (Hein, 2004). A fine resolution along the azimuth direction is instead determined by the length of the antenna. In particular, the longer the antenna, the finer the azimuth resolution. SAR systems "synthetize" a long antenna by exploiting the frequency shifts generated by the relative motion between the antenna and the target on the ground (*Doppler effect*). The pulse footprints partially overlap such that every pixel on the ground is illuminated several times during the forward motion of the satellite (Figure 2.1b). The Doppler effect allows SAR systems to precisely position the pixels along the satellite azimuth (Dzurisin & Lu, 2007). The Doppler analysis process of the raw SAR image is referred to as *Focusing* and the

resulting image is called Single Look Complex (SLC) (e.g. Dzurisin & Lu, 2007; Simons & Rosen, 2007). The along-track or azimuth resolution that can be achieved with SAR is about half the physical antenna length, while the across-track or range resolution is a function of the transmitted radar bandwidth. For the European satellites the finest resolution is about 20 m x 20 m cells.

SAR satellites continuously operate while orbiting the Earth following near-polar orbits (Ferretti et al. 2007). Therefore, repeated SAR measurements of the entire Earth's surface are achieved. When a SAR satellite observes the Earth moving from South to North is called on an *ascending pass* while when moving from North to South is called on a *descending pass*. The SAR antenna is fixed on the same side of the orbital plane with respect to the vector velocity, and it is commonly pointing to the right side of the track hence defined *right-looking* (Dzurisin & Lu, 2007;).

SAR satellites generally operate in the microwave frequency bands, whose wavelengths ranges from 1 mm to 1 m. The frequency bands commonly used by SAR systems are: C-band (4 to 8 GHz, 3.75 cm to 7.5 cm), L-band (1 to 2 GHz, 15 cm to 30 cm) and X-band (8 to 12 GHz, 2.5 cm to 3.75 cm)

Amplitude and phase are the main measurements of SAR systems. The amplitude can be used to produce an amplitude SAR image, whose brightness depends on the incidence angle of the signal and the scattering and diffusion of the terrain (Ferretti et al., 2007). The phase is the most important component of the SAR measurement as the total phase rotations precisely measure the length of the path travelled by the signal between the satellite and the surface Earth. Therefore, by calculating the phase difference between two SAR images (SAR Interferometry or InSAR) of the same area but acquired at different times, we can obtain an image of the ground motions that occurred between the two acquisitions for each pixel on the ground, such an image is called an *interferogram* (Figure 2.2) (Hanssen ,2001; Dzurisin & Lu; 2007; Ferretti et al., 2007). The phase difference is the complex multiplication between a phase image acquired at *date 1* and the phase image acquired at a *date 2* (with date 2 > date 1) (Figure 2.2). In the past the two acquisitions were referred to as *master* and *slave*, respectively. The processing steps required to obtain an interferogram are described in detail in section 2.4.

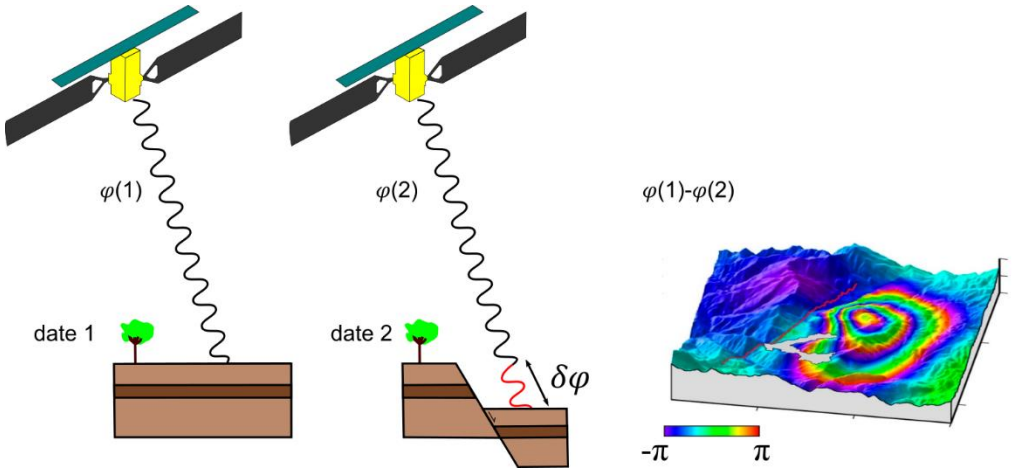

Figure 2.2 – Schematic example of phase difference between two SAR acquisition. An interferogram is generated using two acquisitions made at date 1 and date 2. Normal faulting occurred during the time interval and the ground motion is expressed by the interferometric fringes. The interferogram is a real example of normal fault modified from Cheloni et al. (2019)

In an interferogram the ground motions are measured in the satellite geometry, along the satellite Line-Of-Sight (LOS), and are expressed as cycles of *fringes*, where each fringe (a full cycle of color, i.e. blue-green-yellow-red) represents a phase rotation of 2π. The phase change, is known in the (-π, π) domain (wrapped phase) (Figure 2.2). Furthermore, since SAR satellites commonly have rather steep incident angles, they are most sensitive to the vertical component of ground motion, less sensitive to the E-W component and least sensitive to the N-S component as this is parallel to the satellite orbit. It's important to underline that the orbits covered by the satellite during the acquisitions of the same area can be slightly different. The spatial separation between the two orbits is called *spatial baseline* and its projection perpendicular to the slant range is called the *perpendicular baseline*. The time separation between two acquisitions is called *temporal baseline* (Ferretti et al., 2007). Large perpendicular and temporal baselines corrupt the signal resulting in noise in the interferogram, called incoherence (Hanssen, 2001). Thus, the selection of SAR images for crustal deformation studies must favor short perpendicular and temporal baselines.

The first experiments on SAR sensors have been conducted in the early 60s, but the first scientific applications started in 1978 when the Seasat satellite was launched (Massonnet & Feigl, 1998). In July 1991, the European Space Agency (ESA) launched ERS-1 (European Remote Sensing Satellite 1), the first satellite equipped with a SAR sensor. ERS mission was enhanced in April 1995 with a second satellite, ERS-2 (ESA,

2000-2020; Ferretti et al. 2007). ERS-1 operated until 2000 while ERS-2 officially terminated his mission in 2011. ERS was followed by the ENVISAT satellite, launched in 2002 in order to continue and improve the previous ERS missions. In Earth Science ERS and ENVISAT data have been successfully used to study earthquake and volcanic deformation (Massonnet et al., 1993; Massonnet & Feigl, 1998; Wright et al., 2001, 2004, 2006). ERS-1,2 and ENVISAT were near-polar Earth observation satellites equipped with a SAR sensor operating in C-band and acquiring in Stripmap mode (Monti Guarnieri et al., 2003; Ferretti et al, 2007; ESA, 2000-2020). In Stripmap mode, the antenna always points in a fixed direction (fixed azimuth) and at a constant incidence angle (Figure 2.3a) and the SAR image is acquired through continuous sequences of pulses. The standard Stripmap acquisition mode results in an image swath width in range direction of ~100 km (Ferretti et al. 2007), while in azimuth acquisition is not limited as the satellite acquisition is continuous. However, ESA disseminated data in scenes about 100 km x 100 km. Both ERS and ENVISAT data have been also acquired with different swath width and different incidence angles varying from 15° (I1 track) to 45° (I7) (ESA, 2000-2020). The finest satellites acquisitions have a ground resolution of 4 m (in azimuth) x 20 m (in range), but for Earth deformation studies the final pixel size is commonly averaged to 80 m x 80 m. The revisit cycle of each orbit was 35 days yet both missions did not acquire images systematically around the Earth but only at places where these were ordered, hence continuous catalogues exist only at some locations. ENVISAT mission ended on April 2012 following a loss of contact with the satellite.

The Sentinel-1 (S1) mission comprises a constellation of two polar-orbiting SAR satellites (Sentinel-1A and Sentinel-1B) sharing the same orbital plane and operating day and night (ESA, 2000-2020). S1A was launched on 3rd of April 2014 followed by the second satellite, S1B, on the 25th of April 2016. The mission operates at the C-band with four acquisition modes at different spatial resolutions (from 5 m x 5 m to 25 m x 100 m) and coverage (width ranging from 80 km to 400 km). The Sentinel mission is improved compared to the previous SAR European satellites in terms of spatial coverage, orbit control and the frequent revisit time (12 days with S1A only and 6 days since launch of S1B). The satellites operate in four acquisition modes: Stripmap (SM), Interferometric Wide swath (IW), Extra-Wide swath (EW), and Wave mode (WV). The Interferometric Wide (IW) swath is the default acquisition mode over land as it preserves the 12 days revisit

time. IW allows combining a large swath width (250 km) with a resolution of 5 m in azimuth by 20 m in range. Wide swaths images are obtained by combining three sub-swaths acquired using the TOPS (Terrain Observation with Progressive Scans) mode (De Zan & Guarnieri, 2006; Meta et al., 2010) (Figure 2.3b). In TOPS the wide-swath coverage is obtained by switching the antenna beam along the range direction from burst to burst so that several sub-swaths are acquired quasi-simultaneously, but also the antenna sweeps in the azimuth direction from backward to forward so that all targets are imaged by the entire azimuth antenna pattern (Figure 2.3b) (De Zan & Guarnieri, 2006; Meta et al., 2010). The series of bursts overlap over an area of ~10 km in both azimuth and range direction. After the last burst of the first sub-swath is acquired, the antenna changes elevation and switch back to imaging the following sub-swath (De Zan & Guarnieri, 2006; Prats-Iraola et al., 2012; Yague-Martinez et al., 2016). The change in the antenna elevation during the acquisition of the three sub-swaths results in a variable incidence angle with values ranging between 30°-42° (Geudtner & Torres, 2012). Since each target on the ground is observed by the whole azimuth antenna pattern, the TOPS mode increases the width of the acquired swaths and reduce disturbing amplitude modulations of the signal along azimuth (scalloping effects) (De Zan & Guarnieri, 2006; Meta et al., 2010). On the other hand, the steering of the antenna generates linear variations of Doppler frequency and a reduction of the azimuth resolution respect to the previous Stripmap acquisition mode (De Zan & Guarnieri, 2006; Yague-Martinez et al., 2016). The standard L1 Sentinel products are provided by ESA in slices which are ~170 km-long and made by nine bursts per sub-swath.

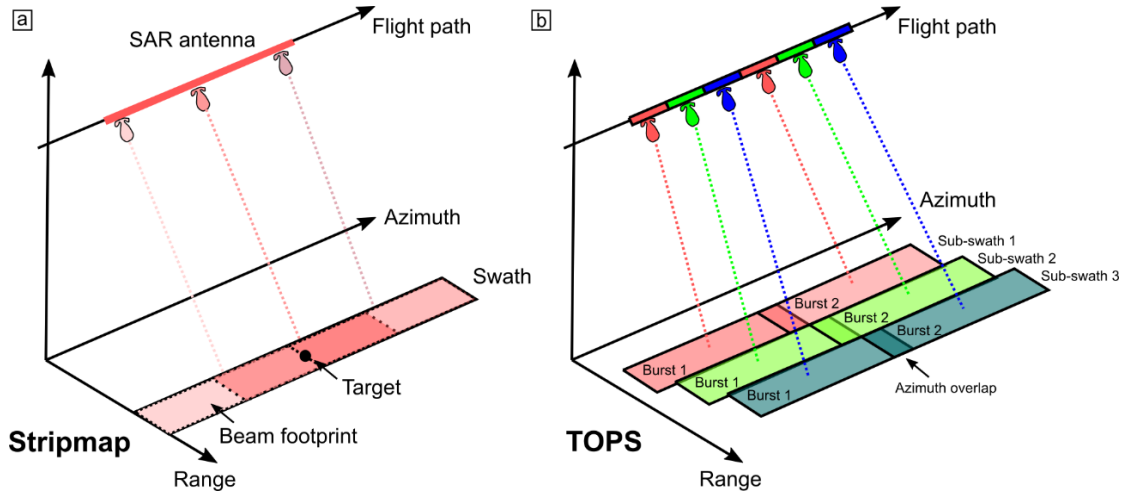

Figure 2.3 - Stripmap (a) and TOPS (b) acquisition modes adopted by ESA's satellites (modified from Merryman Boncori, 2019).

2.1.1 InSAR phase contributions

The interferometric phase does not only include the phase component related to the ground motion but several sources of noise also contribute to the total phase change. Some of these contributions cause a degradation of the interferometric phase as they introduce dissimilarities in the two SAR acquisitions (Hanssen, 2001). The quality of the interferometric phase is expressed in terms of *coherence* which is a measure of the similarity between two SAR acquisitions (Hanssen, 2001). Following Berardino et al. (2002), give two SAR images acquired at date 1 (t_1) and date 2 (t_2) the general expression of an interferogram in terms of phase change ($\delta\varphi$) is:

$$\delta\varphi \approx \frac{4\pi}{\lambda}[d(t_1) - d(t_2)] + \frac{4\pi}{\lambda}\frac{B_{\perp}\Delta z}{r sin\vartheta} + \frac{4\pi}{\lambda}[d_{atm}(t_1) - d_{atm}(t_2)] + \Delta n \quad (1)$$

where λ is the transmitted signal central wave-length, d is the phase component related to deformation, $B_{\perp}$ is the perpendicular baseline, Δz refers to errors in the DEM, ϑ is the incidence angle and d_{atm} is the phase component related to atmospheric artifact. The first term of the equation thus represents the LOS change caused by ground displacements. The second term accounts for topographic artefacts introduced by errors in the DEM (Δz) used for the interferogram generation. Such component also depends on the perpendicular baseline $B_{\perp}$ and the incidence angle ϑ. The third term accounts for atmospheric phase artefacts d_{atm} at the times of both acquisitions, and the last term is the decorrelation effects. The last term (Δn) accounts for other artifact caused by decorrelation effects.

Decorrelation effects causes coherence loss (Hanssen, 2001). These effects are related to both spatial separation between the two acquisition orbits (*spatial decorrelation*) and to changes in the reflectivity of the ground surface that occurred between two sensor's passes (*temporal decorrelation*). *Spatial decorrelation* occurs when the same ground resolution element ($\Delta\rho$) is imaged from too different looking directions, as a change in the look angle leads to a spectral shift between the two SLCs (Rosen et al., 2000). The phase change (and the resulting fringes frequency) is directly proportional to the perpendicular baseline ($B_{\perp}$): If the phase change is equal to or greater than 2π it will results in decorrelation of the interferometric phase and coherence loss (Rosen et al., 2000). The value of $B_{\perp}$ at which a phase change of 2π is generated and spatial decorrelation occurs is called *critical baseline* ($B_{\perp crit}$), which is defined as $B_{\perp crit} \propto \lambda/\Delta\rho$ (Rosen et al., 2000). As can be seen, the critical baseline also depends on the signal wavelength (λ) which means

that the longer the wavelength, the lower the fringe frequency. *Temporal decorrelation* is related to changes in the electromagnetic response of the ground such as caused by vegetation humidity changes, snow cover and variation in soil humidity (e.g. rural areas) (Hanssen, 2001). Decorrelation effects may be minimized by selecting SLC images characterized by small temporal and perpendicular baselines.

Atmospheric artefacts, also referred to as *Atmospheric Phase Screen* (APS), are due to interaction between the radar signal and the atmosphere. The atmospheric phase delay depends on the refractive index, which is a function of pressure and temperature (the 'dry' component) and water-vapor content (the 'wet' component) (Hanssen, 2001). The most variable and significant factor is the water vapor contained in the troposphere (Biggs et al., 2007). It generates a time delay on the transmitted signal and, as a consequence, artefactual fringes in the interferogram. There are two types of APS, based on their physical origin: Turbulent and Layered. *Turbulent mixing* is due to different turbulent phenomena in the atmosphere such as solar heating of the Earth's surface (causing convection), differences in wind direction or velocity and forming storm clouds (Hanssen, 2001). It affects both the flat terrain and mountainous areas. *Layered atmosphere* causes variation of the refractivity along the vertical during the two SAR acquisition. This effect is correlated with topography and affects areas with relief only (Hanssen, 2001). Accordingly, phase patterns typically mimic the topography.

Ionospheric variations can also affect the radar propagation. *Ionospheric effects* can interfere with SAR data focusing and may distort signal polarization and phase. The severity of signal distortion depends on the spatial variability of the ionospheric Total Electron Content (TEC). Ionospheric noise mostly affect L-band SAR data and mainly occur in equatorial regions and at high latitudes (Meyer, 2011). The largest contribution (tens of centimeters) to the atmospheric phase delay comes from the layered atmosphere (Hassen, 2001) and the resulting phase pattern makes it difficult to separate the deformation from the atmospheric signal. This particularly occurs in area where topography and deformation are correlated, like volcanic or tectonically active areas and, if deformation are characterized by low rates (e.g. inter-seismic deformation), they can be masked by atmospheric signals (Biggs et al., 2007; Elliott et al., 2008; Jolivet et al., 2011).

Others sources of noise are related to thermal or the natural ground features of the area (e.g. thick vegetation cover, snow or water) as well as the signal wavelength (Hanssen

2001). In particular, longer wavelengths can penetrate vegetation cover better than shorter wavelengths. This means that L-band radar can receive a signal from the ground and be coherent in a forest area, while C- and X-bands do not penetrate vegetation and remain incoherent.

2.1.2 InSAR processing: ROI_PAC and ISCE

In the following section, I describe the main steps of the procedure adopted for generating an interferogram. In this thesis, ERS and ENVISAT data have been processed by using the Repeat Orbit Interferometry Package (ROI_PAC) software developed by the Jet Propulsion Laboratory (JPL), and Caltech University (Rosen et al., 2004). Sentinel-1 interferograms have been processed using the new JPL/Caltech/Stanford InSAR Scientific Computing Environment (ISCE) software (Rosen et al., 2012). The processing of Stripmap ERS and ENVISAT data is the same, since the satellites share the same acquisition mode. Conversely, Sentinel-1 IW data were acquired in TOPS mode and require a different interferogram generation procedure. For Sentinel-1, I adopted the standard *topsApp* ISCE workflow. The procedures for processing Stripmap and TOPS data are discussed below and consist of Co-registration, Interferogram generation, Orbital and Topography corrections, and Filtering. Finally, the post-processing of ERS, ENVISAT and Sentinel-1 interferograms remain the same.

Co-registration and Interferogram generation

The two SAR images need to be referred to the same spatial grid to allow the correct combination of the phase contribution associated to each pixel of the images. However, corresponding pixels in the two SAR images could be offset owing to the slightly different viewing geometry and topography. Accordingly, the images need to be 'slided off' one another and distorted to achieve the best possible alignment of corresponding pixels (Dzurisin & Lu, 2007). This operation, called *co-registration*, consist in determining the transformation which brings the image at *date 2*, to be superimposed on the image at *date 1*. To this aim, several approaches can be adopted (e.g. Fornaro & Franceschetti, 1995; Sansosti et al., 2006; Dzurisin & Lu, 2007).

In ROI_PAC, Stripmap images are co-registered by applying a polynomial fit approach. Such method consists in estimating the polynomial azimuth and range warp functions which describe the transformations needed to resample the *date 2* SLC to the

date 1 SLC (Fornaro & Franceschetti, 1995). The matching is usually performed in two steps. First, a coarse co-registration is performed starting from a series of tie points and by assessing the shifts with an accuracy of a few pixels. Then, a fine co-registration is performed to refine the matching by comparing approximately corresponding areas in the two images and solving for the set of local transformation parameters.

Due to the strong variations in Doppler frequency introduced by the TOPS antenna steering, Sentinel-1 interferograms require a high co-registration accuracy of ~0.0009 pixels (1.3 cm) which is not ensured by polynomial fit approaches. To account for this, ISCE performs the co-registration at the burst level, by adopting a two-steps approach. A first coarse co-registration is carried out by means of a pixel-by-pixel method (Sansosti et al., 2006) which geometrically positions the ground targets in the interferometric pair using the orbital information and an external DEM. The higher the resolution of the DEM, the more precise is the positioning and the evaluation of the warp functions. In this thesis, I used a standard Shuttle Radar Topography Mission (SRTM) 1 arc sec (30 m) DEM (Farr et al., 2007). A residual misregistration can remain due to errors in the orbit calculation. The most common effect of such misregistration in Sentinel-1 interferograms is the occurrence of phase discontinuities between two bursts. A finer co-registration step thus follows with the application of the Enhanced Spectral Diversity (ESD) method (Prats-Iraola et al., 2012). The ESD obtains the residual azimuth shift by creating interferograms for the burst overlaps (along azimuth) and calculating the Doppler frequency difference in these areas. The bursts of *date 2* are thus resampled and the fine co-registration performed. Just after the burst-level fine co-registration, the Sentinel-1 interferogram is generated by merging the burst interferograms (Sansosti et al., 2006; Prats-Iraola et al., 2012).

The interferogram generation consists is the complex multiplication between the image acquired at *date 2* and the image acquired at *date 1*. The complex signal value of a SAR image, for each resolution element *b*, is expressed as $A_b e^{j\varphi_b}$, where A is the amplitude, while the phase term results from the sum of the surface backscatter phase φ_b and the propagation phase delay, $-j(4\pi/\lambda)\, r$. The term *r* is the distance (*range*) between the satellite and the ground element (Dzurisin & Lu, 2007). The total surface contribution results from the sum of contributions from any scatterer within the resolution element. Since the scatterers have a random arrangement in each resolution element, the phase term φ_b is also random. Thus, if two SLCs are acquired from the same geometry, their random

component will be the same and it will be removed by differencing the two SLCs. By considering the complex signal value for two SLCs, the complex multiplication (*I*) of the co-registered *date 2* (I_2) and *date 1* (I_1) images can be thus expressed as:

$$I = I_1 I_2^* = A_1 A_2 ej(\varphi_1 - \varphi_2) = |I_0| e^{j\varphi} \quad (2)$$

Where the asterisk '*' indicates the complex conjugate and $\varphi = \varphi_1 - \varphi_2$ is the *interferometric phase* (Dzurisin & Lu, 2007).

Orbital and Topography corrections

The different viewing geometry between the two SAR images produces a pattern of phase difference. If the target area were perfectly flat, these differences would be represented in the interferogram by a series of nearly parallel bands called *orbital fringes*. These can be removed by using the information about orbit geometry. The result is called a *flattened interferogram*.

Surface topography observed from two different points also contributes to the phase difference. Topographic artifacts are proportional to the perpendicular baseline and can be minimized by choosing image pairs characterized by short perpendicular baselines. During the interferogram generation, topographic artifacts are also removed from a flattened interferogram by constructing a synthetic interferogram based on known topography and by subtracting it from the flattened one (i.e. using a DEM) (Dzurisin & Lu, 2007).

Filtering

Decorrelation and noise affecting the interferograms can be minimized by applying an adaptive power spectrum filter (Goldstein & Werner, 1998). It has been demonstrated that such filter dramatically reduces the phase noise allowing for better phase unwrapping procedure and increasing the measurements accuracy (Goldstein & Werner, 1998). In ROI_PAC and ISCE, such filtering is thus performed before the unwrapping step. The filter strength is controlled by a parameter varying between 0 and 1, corresponding to no filter and strong filter, respectively. The reader is referred to Goldstein & Werner (1998) for a mathematical description of the filtering procedure.

Phase Unwrapping

The phase change, expressed by a cycle of fringes within an interferogram, is only measured modulo 2π. To retrieve the full phase variation and consequently, the total magnitude of the ground motion, the wrapped phase needs to be unwrapped and the cycles of fringes counted. This problem is called *phase unwrapping*. In the ideal cases of complete coherence, the phase unwrapping would simply consist in integrating the wrapped gradients from an arbitrary starting point to other pixels in the images, through random paths (Dzurisin & Lu, 2007). The unwrapping will be thus independent by the path connecting the pixels. The unwrapped phase can be then converted into ground deformation (cm) by means of the radar wave-length. However, in case of phase noise causing low coherence, or under-sampling phenomena due to high fringe rates, phase discontinuities between adjacent pixels, can occur. In this case the phase unwrapping is strongly dependent from the integration path and it can be very difficult to unwrap an interferogram correctly. Several approaches to this problem have been proposed (e.g. Goldstein et al., 1988; Zebker & Lu, 1998; Chen & Zebker, 2002).

In this thesis, I adopted the ICU Branch-cut method proposed by Goldstein et al. (1988) and implemented in both ROI_PAC and ISCE software packages. The Branch-cut algorithm start from the assumption that, for perfectly coherent interferogram regions, the sum of phase differences between adjacent pixels, in a loop of four pixels is zero. If phase discontinuities occur, such sum will not be zero, giving residuals. The algorithm solves the discontinuities by connecting residuals with opposite polarities through segments, called *cuts*, and delimiting areas where the phase unwrapping cannot occur. Doing so, the algorithm forces the integration path to avoid these areas and lead to a correct phase unwrapping across the other coherent areas.

Geocoding

As a final step, the interferograms are referenced to a geographic reference frame. This is achieved by geocoding the interferograms with respect to the DEM used in the previous steps. The final pixel spacing of the interferograms will depend on the DEM resolution. In the processing, I geocoded the ERS and ENVISAT interferogram by using 3arc-sec (90 m) SRTM DEM, while Sentinel-1 interferograms have been geocoded at higher resolution using the 1arc-sec (30 m) SRTM DEM (Farr et al., 2007).

2.1.3 The dataset used in this thesis

In this thesis I used the SAR data acquired by the European Space Agency (ESA) ERS, ENVISAT and Sentinel-1 satellite to study the deformation in the North-Western Afar Margin and in the Afrera Plain. Figure 2.4 show the spatial coverage of the SAR dataset used in this thesis. ERS interferograms from descending track 321 have been processed to identify possible co-seismic deformation across the margin in 2002. I then processed ENVISAT acquisitions from three I2 ascending (028) and descending (278, 049) tracks (incidence angle of ~26°) along with data from the I6 descending track 464 (incidence angle of ~42°) to investigate deformation during the time-period 2005-2010 in Afrera. Sentinel-1 IW acquisitions from two ascending (014) and descending (079) tracks have also been used to investigate deformation at Afrera during the time period 2014-2019.

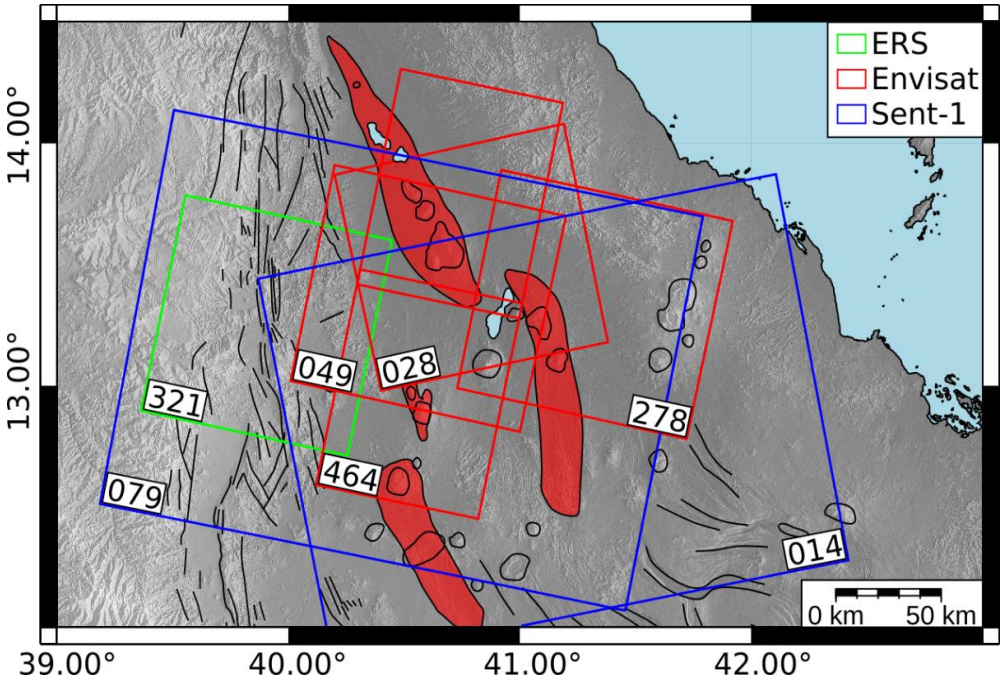

Figure 2.4 – SAR dataset used in this thesis. The colored squares represent the footprints of the SAR tracks, with the relative orbit number.

2.1.4 Multi-interferogram methods: Π-Rate time-series analysis

It has been demonstrated that the atmospheric and orbital contributions to interferograms characterized by long temporal baseline (e.g. 1 year) can be many times larger than the contribution from deformation (Biggs et al., 2007). The simplest method to minimize this problem is the *Stacking*, which works on the principle that the deformation signal in an interferogram has a systematic pattern, while the atmospheric noise is random. In Stacking, *n* interferograms are added together, hence the deformation signal will be *n*

times larger than in a single interferogram, while the noise will be $\sqrt{n}$ times larger. The addition of *n* interferograms lead the signal-to-noise ratio $\frac{S}{N}$ to increase by a factor of $\frac{n}{\sqrt{n}}$ (Figure 2.5). Stacking is suited to study continuous time-progressive deformation (e.g. inter-seismic strain) (Peltzer et al., 2001; Wright et al., 2001; Wright et al., 2004). However, with a simple Stacking method it is not possible to discriminate between continuous and episodic deformation. Therefore, more advanced time-series analysis methods, which aim at constructing a series of short-period interferograms to retrieve both average and incremental deformation (Figure 2.5) as well as their associated RMS misfits on a pixel-by-pixel basis have been developed (e.g. Ferretti et al., 2001; Berardino et al., 2002; Wang et al., 2012).

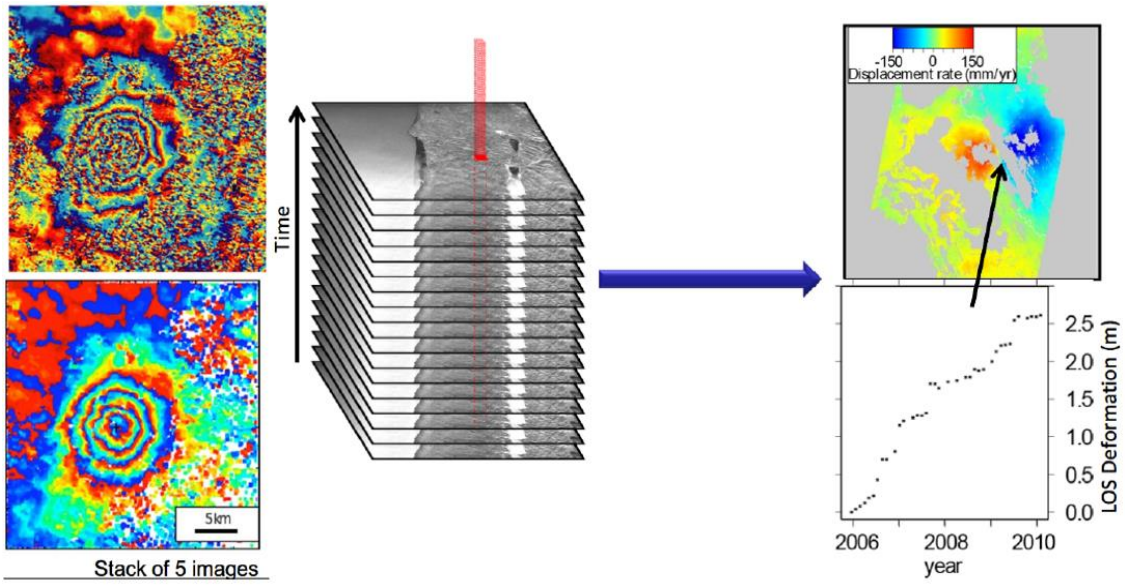

Figure 2.5 – S/R increases by stacking 5 SAR acquisitions. Average velocity maps are obtained by using the stacking method and incremental deformation time-series obtained from the phase information of each acquisition (Wright, 2001).

Given a dataset of geocoded interferograms, such methods invert for a time-series by solving the system of equations:

$$G\boldsymbol{m} = d \tag{3}$$

Where $\boldsymbol{d}$ is the InSAR data vector. $\boldsymbol{G}$ is a design matrix directly dependent on the set of interferograms generated from the available dataset (Wang et al., 2012). Considering an

interferogram $I_{i,j}$ made by two images *i* and *j* acquired respectively at *date 1* and *date 2*, the corresponding raw within the design matrix ***G*** is

$$G_{i,j} = \begin{bmatrix} 0 & \Delta t_i \dots \Delta t_{j-1} & 0 \end{bmatrix} \quad (4)$$

Where $\Delta t_i = t_{i+1} - t_i$, t is the acquisition date, and *n* is the total number of acquisitions. The matrix ***G*** is 0 for acquisitions not covered by the interferogram $I_{i,j}$. ***m*** is the model vector is obtained by converting the incremental range change to incremental velocity v between adjacent acquisitions as follow:

$$\boldsymbol{m} = [v_1 v_2 \dots v_{n-1}]^T = \left[\frac{\varphi_1}{t_1 - t_0}, \frac{\varphi_2}{t_2 - t_1} \dots, \frac{\varphi_n - \varphi_{n-1}}{t_n - t_{n-1}}\right]^T \quad (5)$$

If all the acquisitions belong to a single subset, the system (3) is well- or over-determined and its solution can be obtained by adopting a least-square approach, eventually aided by a Laplacian smoothing operator (e.g. Schmidt & Bürgmann, 2003; Wang et al., 2012). Conversely, when large baselines do not allow the formation of continuous and connected set of interferograms, equation (3) is rank-deficient and admits infinite solutions. In this case, the system can be solved through a Singular Value Decomposition (SVD) method (Berardino et al., 2002).

In this thesis, time-series have been produced by adopting the Poly-Interferogram Rate and Time-series Estimator (Π-Rate) method developed by Wang et al. (2012). Such method is implemented into a series of Matlab routines for the estimation of displacement rates, time-series and related uncertainties from a dataset of unwrapped interferograms. Furthermore, in this thesis, the interferogram networks do not present multiple subsets. I thus inverted for the time-series by adopting a least-square approach.

Π-rate Time-Series workflow

1 - Interferogram Network creation

For a dataset of *N* SAR acquisitions, one can create *N(N-1)/2* interferograms, with *(N-1)* being non-redundant interferograms. Π-Rate produces time-series and average velocity maps by using only the non-redundant interferograms. In a close loop made by three interferograms φ_{ln}, φ_{lm} and φ_{mn} sharing three acquisitions *l*, *m* and *n*, the complete information of phase variation is provided by two interferograms. Π-rate select the best interferogram pair on the basis of the interferogram quality, using a Minimum Spanning

Tree (MST) algorithm. The MST chooses the non-redundant interferograms using two different approaches. The first approach is based on the maximum fraction of coherent pixels. Furthermore, for incoherent areas, Π-Rate re-apply the MST to get coherent pixels from the redundant interferogram and increase the final spatial coverage (Wang et al., 2012). Alternatively, the MST algorithm can create the network of interferogram based on their minimum phase variance. In this thesis, I tested both approaches and I found better results by creating the interferograms network with minimum phase variance.

2 - Unwrapping errors removal

Due to noise and incoherence, the interferograms used for time-series analyses could be affected by unwrapping errors which consist in *n* times 2π phase jumps. Such errors could be detected and corrected manually. However, when working with large data-sets, a manual approach could be time consuming. Π-Rate use phase closure algorithms on multiple interferograms sharing common *date 1* or *date 2* acquisitions to automatically identify and remove unwrapping errors in large data-sets (Wang et al., 2009). Such algorithms (e.g. Kruskal, 1956; Dijkstra, 1959) assume that phase contributions related to tectonics, orbital and atmospheric errors are conservative. Thus, considering a close loop of three interferograms φ_{ln}, φ_{lm} and φ_{mn}, their phase difference is

$$\varphi_{ln} - \varphi_{lm} - \varphi_{mn} = 0 \quad (6)$$

If unwrapping errors occur equation (6) will not be equal to zero but to *n* times 2π. Unwrapping errors can be thus be detected by summing interferograms in a closed loop. In Π-Rate, pixels with unwrapping errors are identified and removed from the processing.

3 - Reference phase

InSAR time-series are usually calculated with respect to a fixed stable point whose deformation is set to zero (e.g. Berardino et al., 2002; Lanari et al., 2007). For a correct estimation of the deformation field, this point must be indeed located in a non-deforming area (e.g. Lanari et al., 2007). Thus, for a proper selection of a stable reference point, external measurements, such as GPS, are usually required. Furthermore, the refence pixel (or group of pixels) must maintain high coherence and low level of noise through the time-series. However, such conditions are hard to meet since noise contributions, as atmospheric noise, can create phase instability above the reference area (e.g. Beauducel et al., 2000). As a result, the estimated deformation field will be affected by errors. Π-Rate offers the

option to overcome this problem by setting the average deformation of each unwrapped interferogram to zero (Finnegan et al. 2008). Doing so, the measured deformation is referred to the entire scene.

4 - Orbital errors filtering

Differences in the satellite orbit during acquisitions result in long-wavelength orbital phase ramps in the interferograms. To remove orbital artifacts, precise orbit information is used during interferogram processing to reconstruct the position of the satellite and remove the effect of baseline separation (flattening). However, residual orbital noise can remain due to imprecise calculations of the satellite position during acquisition. Orbital parameters can be empirically re-estimated by finding the parameters of a linear or a quadratic function that best fit the observed orbital phase ramps. In Π-Rate this operation can be performed for each single interferogram, or epoch by epoch following a network approach (Biggs et al., 2007). The estimated orbital parameters are then used to produce an orbital ramp for each interferogram and removed. A network approach has been demonstrated to better estimate the parameters of the orbital ramp at each acquisition and discriminate long-wavelength deformation signals from orbital artifacts (Biggs et al., 2007). However, part of the real deformation might still be filtered out during the procedure. In Π-Rate such issue can be overcome by masking out the deforming areas before applying the orbital filter. It has been also shown that linear approximations work well for areas which are 100-200 km-long (along azimuth), while quadratic functions are recommended for longer areas (Biggs et al., 2007). In this thesis, the whole Afrera Plain, along with the imaged portions of the active Erta Ale and Tat'Ali rift segments, have been masked before the orbital filtering, furthermore a network-based approach has been adopted to estimate the parameters of a plane function, as the investigated area is shorter than 200 km (along azimuth). An example of good orbital phase removal performed in this thesis can be seen in Figure 2.6.

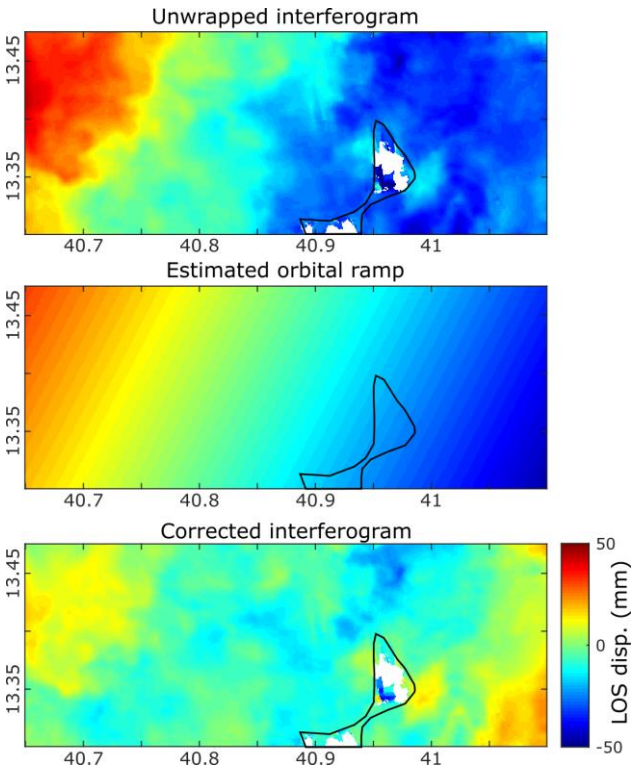

Figure 2.6 – Example of orbital phase ramp removal performed during the processing.

5 – Filtering of topo-correlated delay errors

Layered atmospheric noise is linearly related with topography as the path of the SAR signal illuminating areas of topographic low is longer with respect to the areas of topographic highs. The topographically-correlated atmospheric noise can be estimated and removed by fitting a linear function of the DEM to the phase delay. In Π-Rate this can be performed either interferogram by interferogram (Cavalié et al., 2007) or following a network approach (Elliott et al., 2008). When deformation is correlated with topography, as occurs with volcanic or tectonic signals, removing topographically-correlated noise also remove part of the deformation signal. In this case, part of the deformation can be removed during correction. However, this problem may be overcome by masking all deforming areas before topo-correlated filtering. Alternatively, atmospheric filtering can be performed in Π-Rate by using external atmospheric models from the European Centre for Medium-range Weather Forecast (ECMWF). Previous studies on adjacent regions around the Erta Ale volcano have found that linear fitting with the elevation provides better results respect to the application of external atmospheric models (e.g. Moore et al., 2019). Accordingly, I opted for the linear fitting approach after applying the same mask that I used in the previous step. The good results obtained from such procedure can be seen in Figure 2.7.

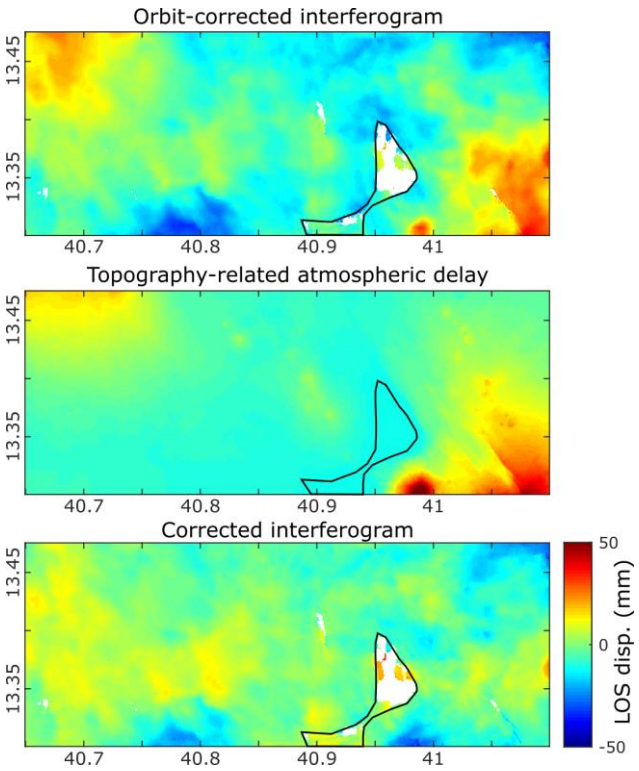

Figure 2.7 – Example of topo-correlated noise filtering by estimating atmospheric delays from the DEM.

6 – Removal of sudden deformation

Sudden deformation can be removed from a time-series in Π-Rate by using the cross-correlation method as also applied in Pagli et al. (2014) to remove the deformation caused by dyke intrusions and retrieve the tectonic deformation. This method consists of three steps: 1) At least two independent interferograms covering the sudden deformation are identified in the series based on the date of occurrence of the sudden event 2) The cross-correlation between the independent interferograms is calculated (Pagli et al., 2014). Pixels affected by the sudden deformation will have high correlation values while poorly correlated pixels will have low correlation (correlation is 0 for complete lack or correlation and 1 for perfect correlation) 3) The sudden deformation is then subtracted from the interferograms covering the event by removing the signal which correlates above a certain threshold. To this aim, the method uses an arc-tangent function:

$$f = 0.5 + \frac{1}{\pi} * tan^{-1}[D * (C - C_T)] \quad (7)$$

where D is the slope of the function f, C is the correlation value obtained in step 2 and C_T is a correlation threshold. A residual Δ_φ interferogram will be then obtained from

$$\Delta_\varphi = \varphi - f * \varphi \quad (8)$$

Where φ represents the shortest interferogram covering the sudden deformation. For a perfect correlation f is 1 and the correlated deformation is completely removed ($\Delta_{\varphi} = 0$). For low correlation f approach zero and the signal is not successfully removed ($\Delta_{\varphi} \approx \varphi$). In the processing I tested several correlation thresholds and I found that C_T between 0.65 and 0.8 successfully removed the sudden deformation, while good D values ranged between 20 and 25, as also reported by Pagli et al. (2014). Figures showing the results of cross-correlation will be provided in Appendix B.

7 - APS estimation and removal

Residual stratified and turbulent mixing components of APS (described in section 2.1.1) can still remain within the time-series and must be filtered out. This can be performed by exploiting the spatial and temporal properties of APS. Such components are in fact poorly correlated in time (i.e. temporally random) but strongly correlated in space. Due to these features, APS can be estimated and removed through a combination of high-pass filter in the time domain followed by low-pass filter in the space domain (Figure 2.8) (Ferretti et al., 2001; Wang et al., 2012). In Π-Rate, a high-pass filter in time can be applied by smoothing the time-series with different types of filters encompassing Gaussian, triangular or mean filter. These filters smooth the short-term fluctuations of the time-series but they do not affect the deformation signal that continues for longer periods. In the processing, I tested both Gaussian and triangular filters and I preferred the first one as it smooths better unrealistic sharp fluctuations of deformation between adjacent epochs. The high-pass component of the signal is then filtered through a low-pass Butterworth filter in space. Instead of applying a spatial filter of fixed size Π-Rate uses a variable window size equal to the e-folding wave-length (α) of a 1D covariance function (Parsons et al., 2006). Alternatively, as for Step 5, external atmospheric ECMWF model can be applied for the APS filtering.

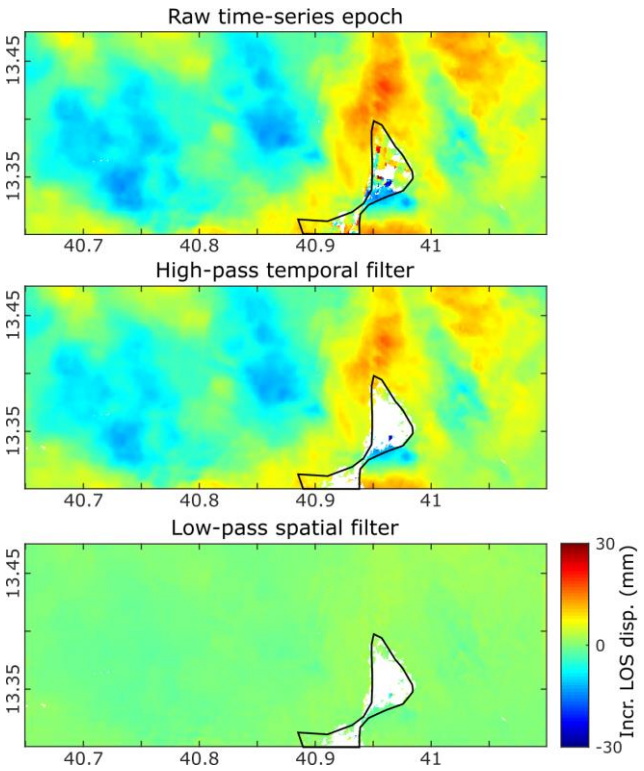

Figure 2.8 – Example of APS filtering in the time-series processing of Sentinel-1 track 079. Here just a single epoch is shown. Further comparisons between complete raw ad filtered time-series are also shown in Chapter 4.

8 – Rate-maps

As a last step a weighted least-square best-fit rate-map is estimated from the time-series for each pixel and using a Laplacian smoothing operator (Schmidt & Bürgmann, 2003; Wang et al. 2009; Wang & Wright, 2012; Wang et al., 2012). The weight is determined by the full temporal variance-covariance matrix. I found the value of the smoothing factor by selecting a value that minimizes the trade-off between the solution roughness vs the RSS of the measured phase **d** and the modeled incremental range change **m** (RSS=$|\mathbf{d}-\mathbf{Gm}|_2$). Inverting the interferogram without smoothing results in time-series with sharp fluctuations between epochs. Conversely, a too strong smoothing could result into an underestimation deformation withing the time-series.

2.1.5 InSAR Modelling

Deformation signals in interferograms can be inverted to understand the sources that caused the deformation and its characteristics, using analytical models buried in elastic medium. To this aim, the Earth is approximated as a homogeneous, isotropic, elastic half-space. Various analytical expressions can then be adopted to mathematically describe the deformation source. An analytical model largely used in Earth Science is the rectangular Okada dislocation (Figure 2.9) (Okada, 1985), which describes the surface deformation caused by fault slips, dike and sill intrusions/contraction (e.g. Wright et al., 2006; Ruch et

al., 2008; Nobile et al., 2012; Pagli et al., 2012; Wang et al., 2014). In this thesis, I used the Okada model to investigate the kinematics of the faults in Afrera associated to the earthquakes of October 2007 and January 2018. A set of simulated interferograms were also produced to constrain the focal depth of the earthquake on March 24, 2018 on the border fault near Mekele.

The Okada model approximates faults, dikes and sills to a finite planar surface (Figure 2.9) with given width (W) and length (L) and located at certain position (x, y) and depth (d). The orientation of the source within the half-space is described by its strike (s) and dip (δ). Depending on the source type the displacement can be expressed by either two or three components: Displacements due to shear faults have strike-slip (ss) and/or dip-slip (ds) components, while only the tensile component (op) is normally used to describe dikes and sills opening/contraction.

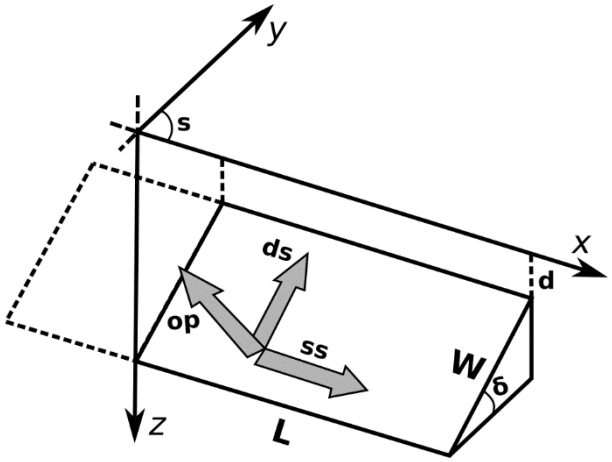

Figure 2.9 - Okada dislocation model

The parameters of the source model describing the surface deformation can be found through inversion of the observed data. Starting from the general eq. (4), the deformation field and the source parameters can be related by solving the system of equations

$$d = G(\boldsymbol{m}) + \varepsilon \qquad (9)$$

where *d* is the deformation data, ***m*** is a vector of the model parameters (i.e. location, length, width, depth, strike, dip and the three displacement components) and G is the function that relates the deformation to the source parameters. Finally, **ε** is the vector of observation errors. The best-fit model will minimize the weighted misfit between prediction and observation. Since the source geometry is not linearly related to the observations, the

estimation of its parameters is a non-linear optimization problem. Such problem can be solved by finding the global minimum of the misfit function for the **m** parameters. Several approaches can be adopted to solve non-linear optimization problems, such as derivative-based (e.g. Arnadottir et al., 1992), random search or Monte Carlo algorithms (Cervelli et al., 2001). Derivative-based approaches are the most effective from a computational point of view. Such methods search for the global minimum of the misfit function by deriving it and moving from high to minimum misfit values. Though very effective, such methods depend on high-order derivatives and, for high gradients of the function, they can remain within local minima, never finding the global one. This often occurs with data characterized by low Signal-to-Noise ratio which results in a misfit function with multiple local minima (Cervelli et al., 2001). A solution is represented by the Monte Carlo algorithms which combine derivative-based methods with random search algorithms. The latter occasionally move back the research to higher misfits allowing the algorithm to escape from local minima. In this thesis, I adopted a Monte Carlo Simulated Annealing method followed by a quasi-Newton algorithm (Cervelli et al., 2001; Wang et al., 2014). Using this approach, the valley containing the global minimum is first identified through simulated annealing. Then the bottom of the valley corresponding to the absolute minimum is reached through the quasi-Newton method.

Before inverting for the best-fit model, the interferograms are sub-sampled using a quadtree partitioning algorithm based on the data variance (Jonsson et al., 2002). The algorithm divides the images into smaller quadrants and the mean of the phase change (in mm) is calculated in each of them. If its standard deviation is higher than a given threshold, a quadrant is further divided into four. This reduces the dimension of the input data without losing significant information and less computing time is needed for the inversion procedure.

The simulated annealing procedure has three main steps: 1) the bounds for each model parameters are set on the basis of a priori geological or geophysical information. This allows to reduce the number of candidate models and, consequently, the complexity of the misfit space. 2) for each model parameter, the algorithm compiles a list of possible solutions, starting from a random model. 3) the probability distribution for each model is then calculated as

$$p_k = e^{\frac{-WRSS}{T}} \quad (10)$$

The probability distribution depends on the misfit between the model and the observation. In this case, the misfit is calculated as the total weighted RMS ($WRMS_{TOT}$) and it depends on the residual sum of squares of the sub-sampled interferograms (I), weighted for the total number of quadtrees

$$WRMS_{TOT} = \sqrt[2]{\frac{RSS(I_1)+RSS(I_2)\ldots+RSS(I_n)}{n_{Tot}Quadtrees}} \quad (11)$$

The term T in equation (11) represents the temperature of the annealing process. Such term quantifies the state of the annealing process at the time of the identification of the minimum and controls the behavior of the algorithm. At high temperatures the algorithm behaves as a random search, and all the models have similar probability distribution. By decreasing the temperature, the algorithm excludes high misfit models and the uphill movements decrease until the model with high probability is identified. The final, derivative-based, quasi-Newton procedure leads to the real global minimum.

Uncertainties on each parameter of the source model have also been evaluated by using a Monte-Carlo simulation of the noise correlated to each input interferogram, following Wright et al. (2003) and Wang et al. (2014). This approach consists in adding noise to the original observed data and generating 100 perturbed simulations of the spatially correlated noise having the same variance-covariance matrix of the original observed data. The perturbed simulations are then inverted and the uncertainties on the source parameters are estimated from the distribution of the model solutions. In particular, I calculated the 90% confidence intervals from the probability distribution of the individual fault parameters. The approach also permits to evaluate the degree of correlation between pairs of parameters by comparing the distribution of their solutions.

2.2 Seismic Analysis

2.2.1 Earthquake location

The source location of an earthquake is described by its three spatial hypocentral coordinates (x_0, y_0, z_0) and by its origin time (t_0) (e.g. Shearer, 2009; Stein & Wysession, 2009; Havskov & Ottemoller, 2010; Lomax et al., 2009). To locate an earthquake, these four unknown variables are commonly constrained using the observed phase arrival times at a network of seismic stations, and travel times predicted from a seismic velocity model. Since the equation has 4 unknowns, a minimum of 4 observed arrival times from at least 3 station are required for the hypocenter determination. Assuming a homogeneous wave propagation medium, the observed arrival times(t^{Obs})at each station (*i)* can be written as

$$t_i^{Obs} = t_0 + u\sqrt{\left[\left(x_i^{Obs} - x_0\right)^2 + \left(y_i^{Obs} - y_0\right)^2 + \left(z_i^{Obs} - z_0\right)^2\right]} \tag{12}$$

where u is the seismic slowness, expressed as the inverse of the seismic velocity 1/v and $\left(x_i^{Obs}, y_i^{Obs}, z_i^{Obs}\right)$ are the coordinate of the recording station i (Lomax et al., 2009). However, the medium through which seismic waves propagate is not homogeneous, resulting in spatially inhomogeneous velocities and slowness. Following Lomax et al. (2009) The eq. (19) can thus be expressed accordingly as

$$t_i^{Obs} = t_0 + \int_{r_0(s)} u\,(r_0)ds \tag{13}$$

where $r_0(s)$ indicates the position of a point at distance s along a ray path connecting the earthquake and the seismic station. A well-located earthquake will have minimum misfit between observed and predicted arrival times, expressed as a least-square norm (Havskov & Ottemoller, 2010):

$$\varepsilon = \sum_{i=1}^{n}\left[t_i^{Obs} - t_i^{P}\right]^2 \tag{14}$$

The equations (13) and (14) show that the earthquake origin time (t_0) does not scale linearly with its position. A change in the earthquake position results in fact in a nonlinear change of (t^{Obs}) along with a change in the ray path. This reduces the earthquake location to a problem of non-linear optimization. Non-linear (or direct search) earthquake location can be performed through either a regular or a stochastic search within a space of possible solutions

(e.g. Tarantola & Valette, 1982; Sambridge & Drijkoningen, 1992; Mosegaard & Tarantola, 1995; Lomax et al., 2000) .

2.2.2 Non-linear Earthquake Location: NonLinLoc

In this thesis, earthquake location has been performed through a non-linear probabilistic inversion (Tarantola & Valette, 1982; Moser et al., 1992; Wittlinger et al., 1993) implemented into the NonLinLoc (NLLoc) software by Lomax et al. (2000). As showed by Tarantola and Valette (1982), assuming errors in the observed arrival times and in the calculated travel times to be Gaussian, the four-dimensional problem of earthquake location can be reduced to a three-dimensional problem. Starting from this assumption, NLLoc uses a posterior probability density functions (PDF) or a misfit function to constrain the unknown parameters describing the earthquake location within a 3D, x, y, z, spatial grid**.** The best hypocenter location will be the maximum likelihood solution (or minimum misfit) of the non-linear location PDF. In NLLoc, the PDF can be constrained using either a L2-Norm Least Square or an Equal Differential Time (EDT) likelihood function (Lomax et al., 2000, 2009). The latter offers a more robust estimation of PDF in the presence of outliers within the observed arrival times, i.e. when observations have residuals higher than their nominal errors. Using N observations, the PDF for a location **x** estimated with the EDT approach is

$$\mathrm{PDF(x)} \propto k \left[\sum_{obs_a, obs_b} \frac{1}{\sqrt{{\sigma_a}^2+{\sigma_b}^2}} \, e^{\left(-\frac{\{[Tobs_a(x)-Tobs_b(x)]-[TT_a^P(x)-TT_b^P(x)]\}^2}{{\sigma a}^2+{\sigma_b}^2} \right)} \right]^N \qquad (15)$$

where TT_a^P and TT_b^P are the predicted travel time estimated using pairs of observation obs_a and obs_b, σ_a and σ_b are the standard deviations associated with the observations. In the equation (15) the first term in the square brackets of the exponent is difference between the observed travel times, while the second term is the difference between the predicted travel times. The best-fit location **x** should have the exponential term equal to 1 and this occur the two differences are equal (Equal Differential Time) (Lomax et al., 2000, 2009). NLLoc also perform statistical analyses of the best-fit solution quality by calculating the semi-axes of the 68% confidence error ellipsoid which best approximate the PFD function. Furthermore, it calculates the weighted root-mean-square of residuals obtained by differencing the observed and the predicted travel times.

In this thesis, the great variability in the geological features of the study area (e.g. crustal thickness, lateral variation of Vp and Vp/Vs ratios), which cannot be fully reproduced in a velocity model, favors the presence of outliers. For this reason, I adopted the EDT likelihood function which ensured more stable solutions for the located events. In NLLoc, an accurate mapping of the location PDF in the 3D space can be carried out through the Oct-Tree sampling method. A graphic depiction of the method can be seen in Figure 2.10.

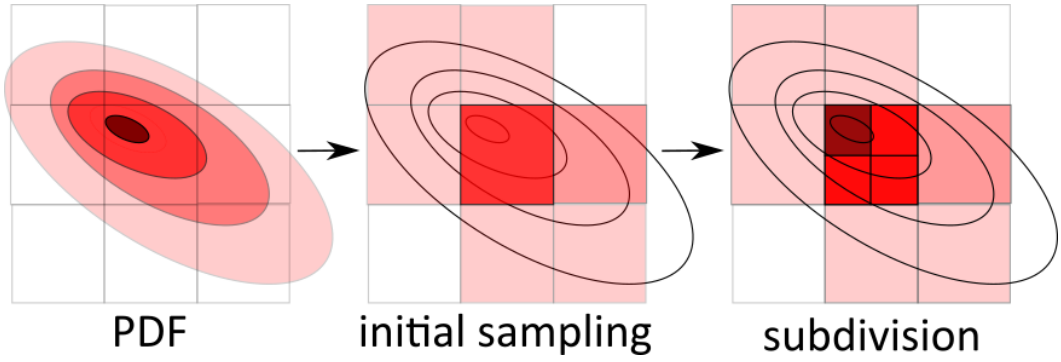

Figure 2.10 – Main steps of the Oct-tree sampling method (in 2D view). The Circles represent a section of the tridimensional PDF while the squares represent the progressive sampling performed by the Oct-Tree algorithm.

Following an approach similar to the quad-tree algorithm previously described for InSAR inversion, the Oct-Tree method recursively divides the 3D spatial grid in eight smaller three-dimensional cells (Figure 2.10). The probability *P* that a given cell *i* contains the earthquake location is calculated as

$$P_i = V_i PDF(x_i) \tag{16}$$

Where *Vi* is the cell volume and $x_i$is a vector containing the coordinates of its center. An initial global sampling is initially performed to search through the entire 3D grid and the probability and misfit values at each cell are calculated. The cells with the highest probabilities are then recursively divided into eight smaller cells and the probability is again calculated until a minimum cell size (100 m^3 in this thesis) or a maximum number of iterations is reached. At the end of the procedure, the center of the cell with maximum probability will be the optimal earthquake location.

2.2.3 Relative Double-Difference Earthquake Location: HypoDD

In active tectonics studies, relative relocation methods are often used to improve the resolution of hypocenter locations and investigate in detail the geometry of active tectonic structures (e.g. Waldhauser & Ellsworth, 2000; Dunn et al., 2010; Sigmundsson et al., 2015, Lavayssière et al., 2019). In this thesis, I used the Double-Difference method implemented into the HypoDD software (Waldhauser & Ellsworth, 2000; Waldhauser, 2001) to relocate the seismic sequence occurred at the North-Western Afar Margin in March 2018.

As shown in the previous section, the precision of the hypocenter determination depends on various factors, such as the number of picked phases for each event, the distribution of seismic stations around the study area, and/or the accuracy of the seismic velocity model. Double-Difference relocation allows us to reduce the effect of difference between the velocity model and the real Earth by comparing the travel times for pairs of earthquakes at each station. This method assumes that the hypocentral distance between two earthquakes *i* and *j*, pertaining to the same cluster is much smaller than that separating the events and the seismic stations. These events are thus characterized by similar ray-paths to a given seismic station *k* and any difference in their travel times$\left(t_k^i - t_k^j\right)$ depends on their hypocentral distance. Using a 1D velocity model and assuming a constant slowness vector for close events, the residual between the observed and predicted travel times is

$$dr_k^{ij} = \left(t_k^i - t_k^j\right)^{obs} - \left(t_k^i - tj_k\right)^{cal} \tag{17}$$

the equation (19) can be also express by considering the vector of differences in the hypocentral parameters between two the events $\Delta m^{ij} = \left(\Delta dx^{ij}, \Delta dy^{ij}, \Delta dz^{ij}, \Delta dt^{ij}\right)$ as

$$dr_k^{ij} = \left(\delta\, t_k^i/\delta\, m\right)\Delta m^i - \left(\delta\, t_k^j/\delta\, m\right)\Delta m^j \tag{18}$$

By extending the equation (18) to all the events and all the seismic stations HypoDD form a system of linear equations and readjusts the hypocenters in order to minimize the residuals by solving through a L2-norm least-square approach. Readjusting the hypocenters tends to result in a collapse of the earthquakes along narrow zones allowing to highlight the main structural trends.

2.2.4 Amplitude measurements and Magnitude determination

The magnitude is the estimate of the earthquake size based on the amount of ground motion recorded by seismometers. Several magnitude scales exist with the most common used for earthquakes recorded on nearby seismic stations is the Richter scale (Richter, 1935) which measures the local magnitude (M_L) of an earthquake as:

$$M_L = \log(A) - \log(A_0) + C \quad (19)$$

Where A is the zero-to-peak amplitude on the body waves (P- or S-wave) wave recorded by the instrument; $\log(A_0)$ is a correction term which consider the distance of the seismometers from the epicentral area and C is a correction term for each component of the seismometers. According to this scale, a M_L 3 would result in a ground motion of 1 mm, measured at a distance of 100 km from the hypocenter by a standard Wood-Anderson seismometer. However, the Richter scale is influenced by local attenuations of seismic waves and tends to under- and over-estimates magnitudes at near and distant stations, respectively (Hutton & Boore, 1987). A solution has been provided by Hutton & Boore (1987) which found the way to calculate local attenuation rates and estimates distance corrections for each study area as:

$$-\log(A_0) = n\log(r/17) + K\,(r - 17) + 2 \quad (20)$$

Where *n* and *K* must be calculated and depend on geometrical spreading and attenuation of seismic waves, while *r* is the hypocentral distance. According to the resulting local magnitude scale, a M_L 3 earthquake would produce a deflection of 10 mm on a Wood-Anderson seismometer located at 17 km from the hypocenter. Based on this equation, Illsley-Kemp et al. (2017) developed the local magnitude scale for the Danakil depression by inverting more than 30000 zero-to-peak amplitudes measurements on the east-west and north-south components of local seismic stations, to calculate the *n, K* and M_L values. The resulting distance correction for the Danakil depression is equal to:

$$-\log(A_0) = 1.274336\log(r/17) - 0.0002731\,(r - 17) + 2 \quad (21)$$

In this thesis, I estimated local magnitudes (M_L) for the located earthquakes by measuring the zero-to-peak amplitude of the body-waves on both the EW and NS components of the simulated Wood-Anderson seismograms. I then computed the magnitude of both

components at all stations with a phase measurement, and then averaged these to compute the overall earthquake magnitude. For the calculation of local magnitude I used the distance correction for the Danakil region calculated by Illsley-Kemp et al. (2017) and reported in equation (21). Following Kanamori (1977) and Aki & Richards (1980), I used the estimated magnitudes to calculate the seismic moment released by each earthquake, in Newton-meter (Nm) as:

$$Moment = \left[10^{\left(\frac{3}{2}M_L + 16.1\right)}\right] * 10^{-7} \quad (22)$$

The obtained values have been finally used to calculate the cumulative seismic moment release for the investigated areas.

2.2.5 Focal mechanisms

A seismic source is geometrically described by three angles: the *strike* is the angle between the North and the line resulting from the intersection between the fault and a horizontal surface (Figure 2.9); the *dip* is the angle between the fault plane and a horizontal surface (Figure 2.9); finally, the *rake* is the direction of slip along the fault plane. Such geometrical setting can be fully represented by considering the seismic source as related to a double-couple, a system of acting forces characterized by equal moment and opposite directions. In three dimensions, a double-couple is mathematically described by a 3-by-3-components, symmetrical tensor, known as moment tensor (Aki & Richards, 1980). For a double-couple earthquake, the three main orthogonal axes of its moment tensor provide for the directions of maximum compression (P axis), maximum tension (T axis) and null axis (N axis). The fault plane related to the earthquake will be at 45° respect to the P and T axes and will contain the N axis. The full description of the seismic source includes a fourth component, the slip vector (D), that defines how the double-couple act on the fault plane. A focal mechanism is the graphical representation of the moment tensor geometry (Stein & Wysession, 2009; Havskov & Ottemoller, 2010) . The associated double couple divides the three-dimensional space around the seismic source into four quadrants that can be characterized by motions either toward or away from the source. Due to the symmetrical nature of the double-couple moment tensor, the two surfaces dividing the quadrants, known as the main and auxiliary nodal plane, are both oriented 45° respect to the P and T axis and both potentially represent the fault surface (Stein & Wysession, 2009; Havskov & Ottemoller, 2010). The simplest way to solve for an earthquake focal mechanism is to

analyze the polarities of the first P-wave arrivals at a number of stations around the seismic source. Positive P-wave polarities are observed at the stations located within the compressive quadrants while negative polarities are observed at the tensional ones. Thus, by knowing the hypocentral location, the take-off angles and the ray-paths of the P-wave to each station it is possible to calculate the three-dimensional orientation of the two nodal planes (Stein & Wysession, 2009; Havskov & Ottemoller, 2010). The accuracy of the focal solution depends on the number of observed polarities and the distribution of the seismic stations around the source. Usually, a minimum of ten observations are required and the station should be distributed all around the source. In a focal mechanism, the two nodal planes are usually represented through stereographic projections onto a lower hemisphere, known as beachballs (e.g. Stein & Wysession, 2009) (Figure 2.11). Compressive quadrants are usually colored while the tensional ones are white.

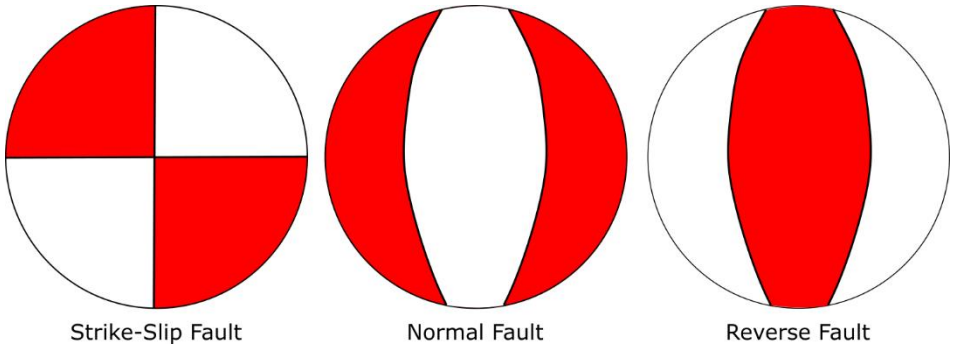

Figure 2.11 – Fault types as represented by focal mechanisms. Here I show a projection onto the lower hemisphere of the focal sphere.

In this thesis, I computed 20 focal solutions for earthquakes pertaining to the seismic sequence of Mar-Apr 2018 along the North-Western Afar Margin. To this aim, I used the software FOCMEC (Snoke, 2003) which exploit the observed P-wave polarities, the take-off angles, the stations and hypocentral locations to perform a grid-search for the best-fit double-couple solution.

2.2.6 Seismic dataset used in this thesis

In this thesis, I analyzed continuous seismic data recorded by three temporary networks active in Ethiopia during 2007-2009 and 2017-2018. Seismic recordings during 2007-2009 have been collected by the Afar Consortium networks, made by 44 IRIS-PASSCAL and SEIS-UK 3-component, broad seismometers, acquiring at a sampling rate of 50 Hz (Ebinger et al., 2008; Belachew et al., 2011). The Afar Consortium data have been used to investigate

the seismicity in Afrera between July 2007 and August 2008 when 18 seismic stations where operational across the Afar depression (Figure 2.12).

Seismicity during 2017-2018 has been recorded during the most recent seismic experiment performed in Ethiopia, following a collaboration between the Universities of Southampton (UK), Addis Ababa (Ethiopia), Strasbourg (France), CNRS/Sorbonne (France), and Pisa (Italy). The experiment was conducted across the Western Afar Margin (WAM) with the main aims of investigating the tectonic activity and the crustal structure of the rift margin. To these aims, two seismic profiles have been installed across the Northern and Central sectors of the WAM, at latitudes ~N13.5° and ~N12°, respectively. The two profiles encompassed 10 SEIS-UK and 20 French Sismob-RESIF 3-component, broadband seismic stations, acquiring at sampling rates of 100 Hz. Further technical details on the network and the survey procedure can be found in Keir et al. (2020). The involvement of the University of Pisa in the project also included my direct participation in the last phases of the seismic survey, during the download of the data and the recovery of the seismic stations. In this thesis, the network has been also used to locate the seismicity accompanying fault slip at the Afrera Plain in January 2018. To this aim, I inspected 31 day of continuous recordings during January 2018 (Chapter 4). During this period, 24 seismic station from both profiles were operational (Figure 2.12). The same network has been used to investigate the seismic sequence of March 2018 East of Mekele (Chapter 5). In this case, I inspected 41 days of continuous seismic recordings (between 20 March 2018 and 29 April 2018).

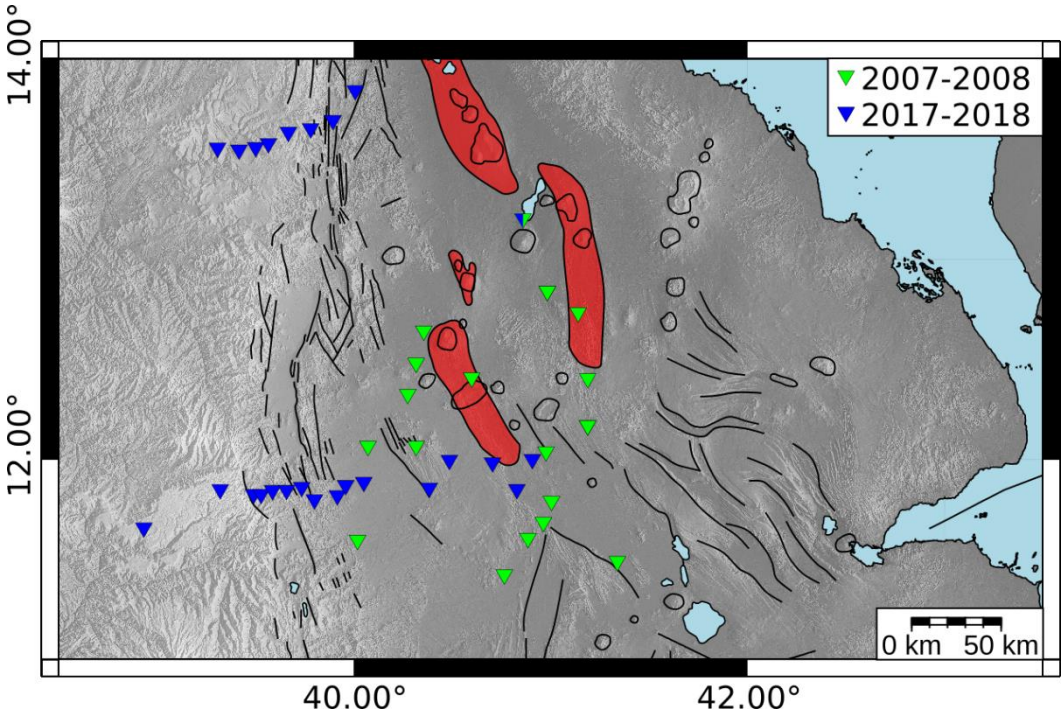

Figure 2.12 – Temporary seismic networks used in this thesis for the earthquake location. The green reversed triangles are part of Afar Consortium network active during 2007-2008. The blue reversed triangles are instead the two local networks active during 2017-2018.

2.2.7 Seismic Velocity Model

The earthquakes identified in the continuous seismic recording have been located by using a new 2.5D P- and S-wave velocity model specifically created for this project. A correct model reproducing the crustal structure of the investigated area and a proper Vp/Vs ratio are crucial for a precise earthquake location. However, these could be challenging to obtain when working on areas characterized by complex crustal structures and strong variations in Vp/Vs ratios, as it has been observed in Afar by Makris & Ginzburg (1987), Maguire et al. (2003) and Hammond et al. (2011). Starting from these observations, I created a 2D velocity profile cross-cutting both the Afar margin and axis in an EW direction, along a distance of 250 km. The profile has been then extended to 350 km along the third dimension (NS in this case) to create a 2.5D grid. Since lateral variations along the third dimension are not allowed by NLLoc, I made a model characterized by crustal features intermediate between the Northern and the Central Afar, where the seismic stations and the study areas are located. The reader is referred to Section 1.2 for a detailed description of the Afar crustal structure while the 2D velocity profile is shown below in Figure 2.12. The velocity model has a crustal thickness of 35 km below the Ethiopian plateau which gradually decreases to 18 km at the rift axis (Figure 2.12). The topography has been also reproduced with elevations

varying from 2 km at the plateau to 0.5 km at the axis. The crustal structure is made by 4 layers encompassing the cover rocks, the basalts, the upper and lower crust, with velocities gradually increasing from 4.4 km/s at the cover rocks to 6.8 km/s at the base of the lower crust. An additional upper low velocity layer (3.3 km/s) has been introduced in the rift zone to reproduces the recent sediments. Finally, an upper mantle with uniform velocity of 7.4 km/s complete the model (Figure 2.12).

Vp/Vs ratios can vary significantly across Afar depending on the crustal structure and composition. Here, I modified the Vp/Vs ratios on the basis of the seismic network adopted for the earthquake location. In detail, the Afar Consortium network (2007-2009) was located entirely within the rift floor where values < 1.9 have been measured except for the rift segments where magma and fluids increase the Vp/Vs to values > 2.0. By comparing the preliminary seismic locations with the InSAR co-seismic deformation of 2007, I found that a Vp/Vs of 1.8 provided the best results, with earthquakes located closest to the deformation patterns identified using InSAR.

In contrast, for the study of seismicity on the rift margin I used a different Vp/Vs, since high variability in Vp/Vs ratios characterizes the margins where the two most recent networks (2017-2018) were located. In this case, I tested several Vp/Vs ratios and produced Wadati diagrams using a subset of 600 events in order to find a value corresponding to an average through the model (Figure 2.13). I found minimum residuals for Vp/Vs ratio of 1.74 which average those measured by Hammond et al. (2011) at the stations along WAM (Figure 2.13).

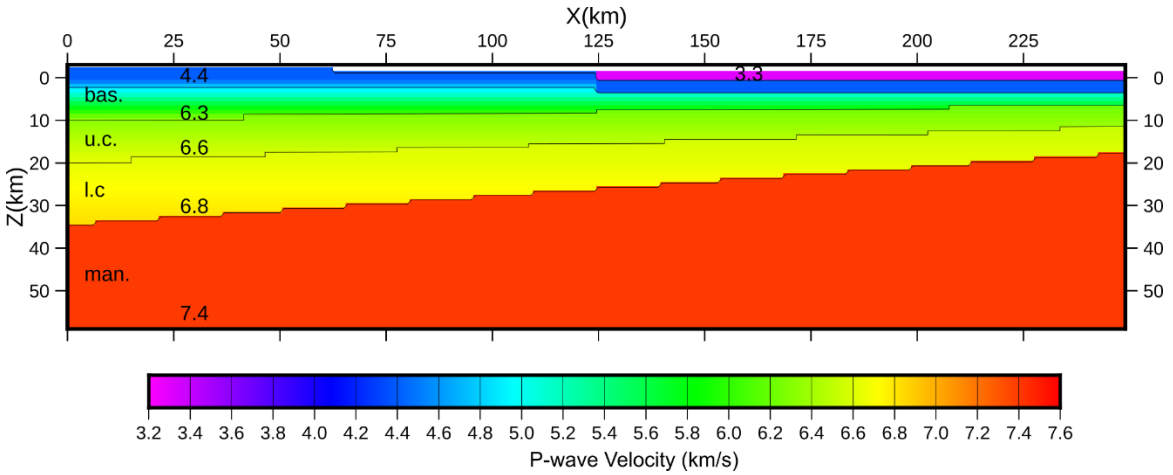

Figure 2.12 – Seismic P-wave velocity model created in this thesis.

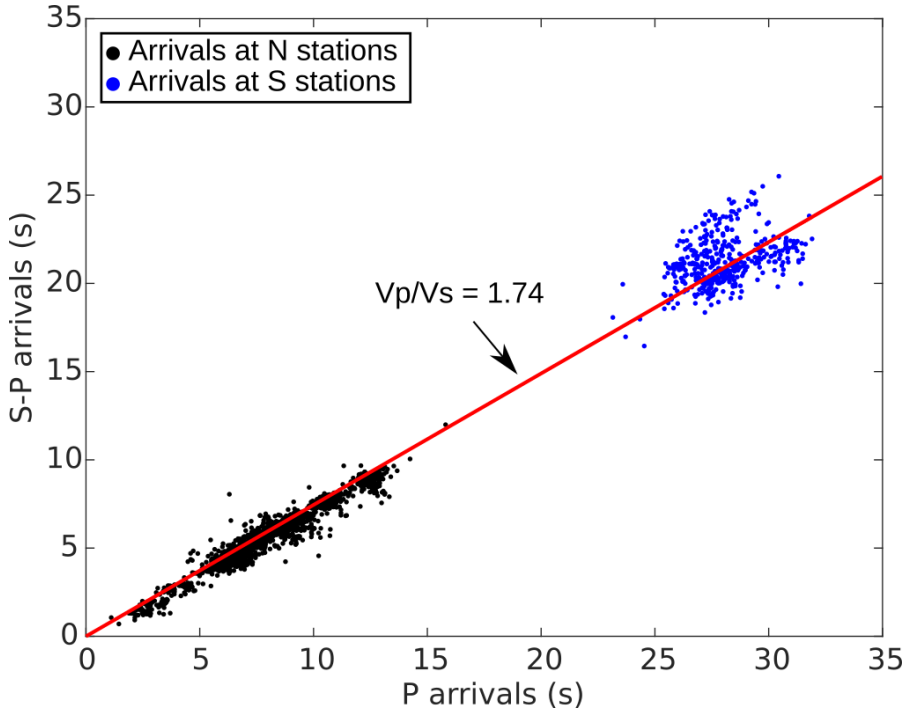

Figure 2.13 – Wadati diagram obtained by using P and S arrival of 600 earthquakes at the stations of the most recent network (2017-2018).

3. Episodic oblique slip in the Afrera rift-linkage in Northern Afar

In this chapter, I combined InSAR measurements with seismicity and structural analyses to investigate the kinematics of the Afrera Plain (AP) linkage zone, between the Erta Ale (EA) and Tat'Ali (TA) segments (Northern Afar). To this aim, I first performed a detailed structural mapping by interpreting high-resolution satellite imagery and elevation data from the Shuttle Radar Topography Mission Digital Elevation Model (SRTM-DEM). Remotely acquired data have been complemented with a series of structural field measurements collected during the geophysical campaign performed in Afar in October 2018. I then processed InSAR data from ENVISAT (ENV) acquisitions and identified a deformation patterns related to fault slip occurred the 2 October 2007. The kinematics of faults which ruptured during this event has been thus investigated by performing fault modeling through non-linear inversion of three co-seismic interferograms. I also analyzed the seismicity accompanying the main events by using data recorded by the temporary seismic networks active during 2007-2009 (AFAR consortium project, Ebinger et al., 2008; Belachew et al., 2011).

3.1 The Danakil Depression and the Afrera Plain

In Northern Afar, the Danakil depression started opening following the southward propagation of the Red Sea rift branch approximately ~30 Ma. Two main magmatic segments, the EA and TA segments, are currently active in Northern Afar (Figure 3.1). Here, extension occurs through dominant magmatic activity characterized by repeated diking episodes along with faulting (e.g. Nobile et al., 2012; Pagli et al., 2012; Xu et al., 2017; Moore et al., 2019). The EA and TA segments strike are arranged en-echelon, with the EA segment left-stepped with respect to TA. The two segments partially overlap within a ~20km-wide area known as Afrera Plain (AP) (Figure 3.1b). The AP is a strongly depressed region reaching elevation of 100 m below the sea level, and hosting a salty water lake (Afrera Lake) fed by hydrothermal springs (Figure 3.1) (Bonatti et al., 2017). The AP is bounded to the East by systems on West-dipping normal faults which represent the northernmost portion of TA and control the evolution of the eastern lake's shore (Bonatti et al., 2017). Conversely, the Western termination of the AP, close to the EA segment, is not clearly defined. Evaporitic

deposits and basalts broadly cover the AP (Keir et al., 2013) with alignments of scoria cones and lava flows suggesting that magmatic activity occurred in the past. Furthermore, high V_P/V_s ratios (> 2.0) have been also measured in the area by Hammond et al. (2011) and have been interpreted as due to the presence of great amount of magmatic fluids between EA and TA. At the center, the AP is dissected by systems of ~NS-striking faults which accommodate the interaction between EA and TA (Figure 3.1). Seismic recordings from temporary networks in Afar (Belachew et al., 2011; Illsley-Kemp et al., 2018) have shown continuous seismicity along these fault systems indicating that the AP is tectonically active (Figure 3.1). Seismicity at AP is characterized by low-magnitude earthquakes accompanying moderate events with $M_w > 5$. The most recent event reported in global catalogs is the M_w 5.1 occurred the 2 October 2007.

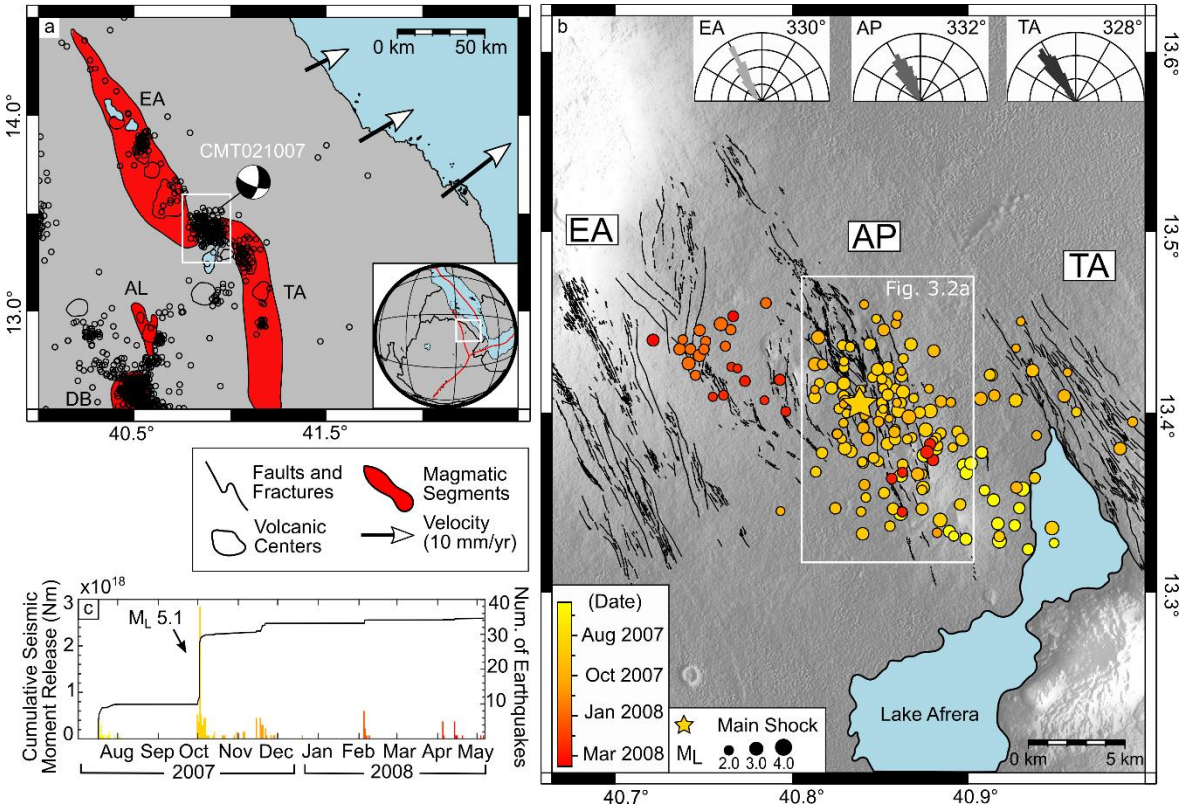

Figure 3.1 - Tectonics and seismicity of Afar. (a) Magmatic segments in northern Afar and seismicity during 2005–2009 (black circles; Ebinger et al., 2008). Focal mechanism is from the Global Centroid Moment Tensor (GCMT) catalogue (Ekström et al., 2012). GPS velocities are from McClusky et al. (2010). The white box marks the location of Figure 3.1a and 3.2. (b) Relocated seismicity between July 2007 and May 2008 with faults and fractures (black lines). The rose diagrams show the faults orientations of the EA and TA rift segments and the AP offset. (c) Cumulative seismic moment release and number of earthquakes as in (b).

3.2 Structural Mapping

I carried out the structural mapping by interpreting 1m-resolution satellite imagery (Digital Globe) along with the 30m Shuttle Radar Topography Mission Digital Elevation Model (SRTM-DEM) (Farr et al., 2007) available on ArcMap 10.6 and Google Earth Pro. I identified more than 2000 faults and fractures across the Northern TA and Southern EA segments and the AP. For each zone, I measured the fault strikes using the tip-to-tip approach and reported them within 4° binned rose diagrams (Figure 3.1b). The faults in the AP have also been analyzed with further detail to identify different populations and possible kinematics indicators. Following Acocella & Korme (2002), I made direct field measurements of opening directions on pairs of asperities across extensional fractures to retrieve the local extension direction (Figure 3.2 and 3.3, Table 3.1). Measurements have been collected at the Southern tip of the main fault system that I previously identified from satellite imagery and it hosts a system of horsetail type fractures (Figure 3.2).

Faults within the two rift segments of EA and TA show the same regional NNW trend with structures having average strike of N330°E and N328°E, respectively (Figure 3.1b). Conversely, I observed a less homogeneous strike of faults and fractures at AP, with the major faults having an average strike of ~N340°E (Figure 3.1b). I identified a main fault system at the center of the Afrera Plain, between longitude ~E40.85° and E40.91°, showing more developed fault segments, with respect to the tips of the linkage zone. Here, the fault system consists of a set of main faults connected by complex patterns of fractures and minor faults that form a lozenge-shaped releasing bend (Figure 3.2a). Similar fault geometries have been observed in oblique extensional settings, such as San Andreas fault (California), or Salina del Fraille (Argentinian Andes) (Reijs & McClay, 2003; Cunningham & Mann, 2007) and experimental models are also able to reproduce these faults (Kim et al., 2004; Corti, 2012; Dooley & Schreurs, 2012; Philippon et al., 2015; Corti & Dooley, 2015). Horsetail type fractures system at the southern tip on the fault system have average opening direction of N47°E (Figure 3.2b and Figure 3.3, Table 3.1). Horsetail structures tend to develop where slip gradually dies in regions of lateral shear. Since this pattern tends to propagate when extension is perpendicular to the fracture planes, the fault grows with a path that is curved with respect to fault strike (Kim et al., 2004) as observed at AP. This suggests that a motion with a left-lateral component characterizes the faults at AP (Kim et al., 2004; Kim & Sanderson, 2006).

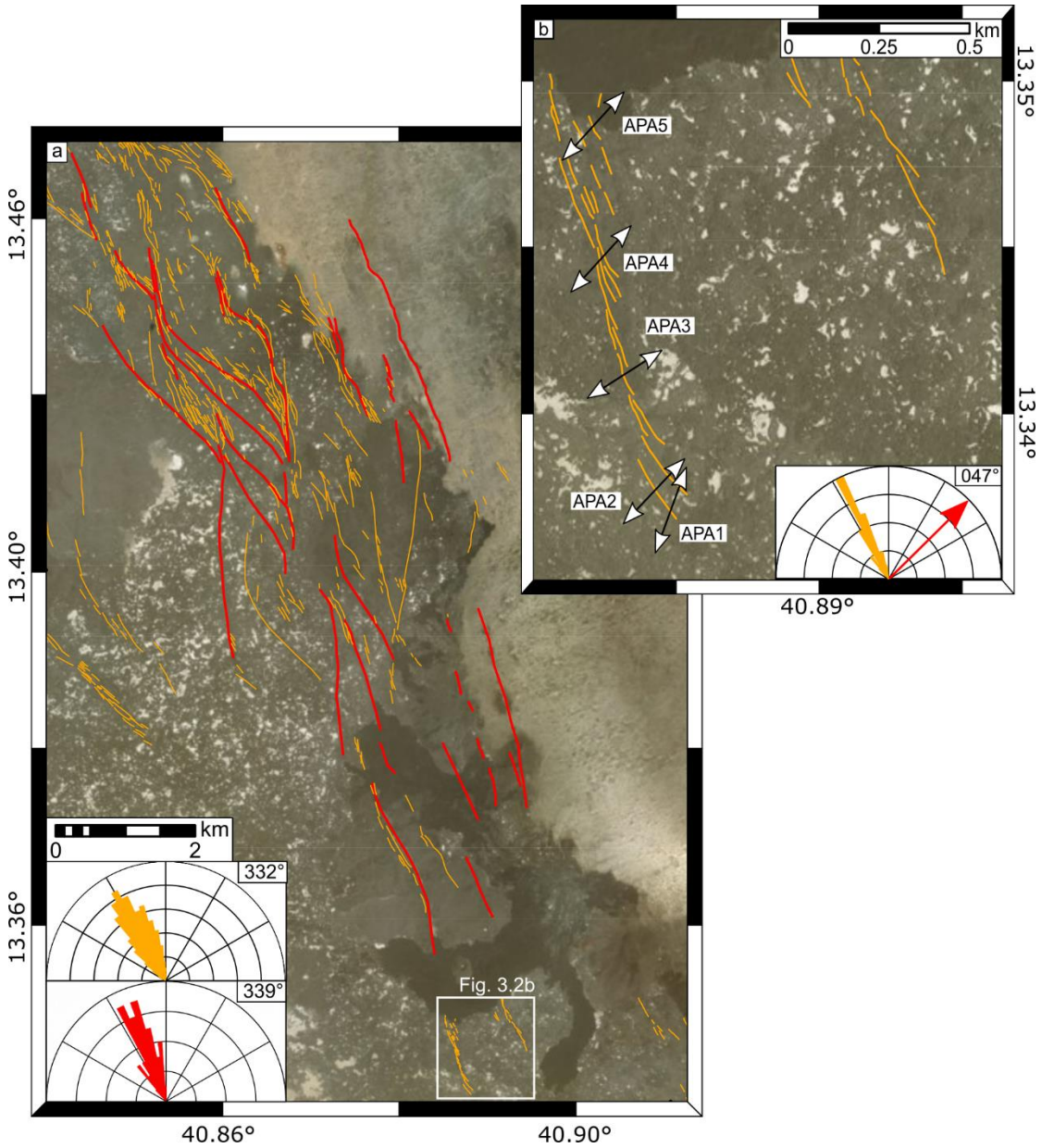

Figure 3.2 - Structures at Afrera Plain (see Figure 3.1b for location). (a) Faults (red lines) and fractures (orange lines). The rose diagrams show the strikes of the structures using the same colors as in the map. (b) Field measurements of opening direction along extensional fractures. The rose diagram shows an average opening direction of N47°E, oblique to the average fractures' direction of N332°E.

Site code	APA1	APA2	APA3	APA4	APA5
Opening direction	N30°E	N45°E	N70°E	N45°E	N45°E

Table 3.1 - Fracture opening directions measured in the field. Site codes as in Figure 3.2b and 3.3

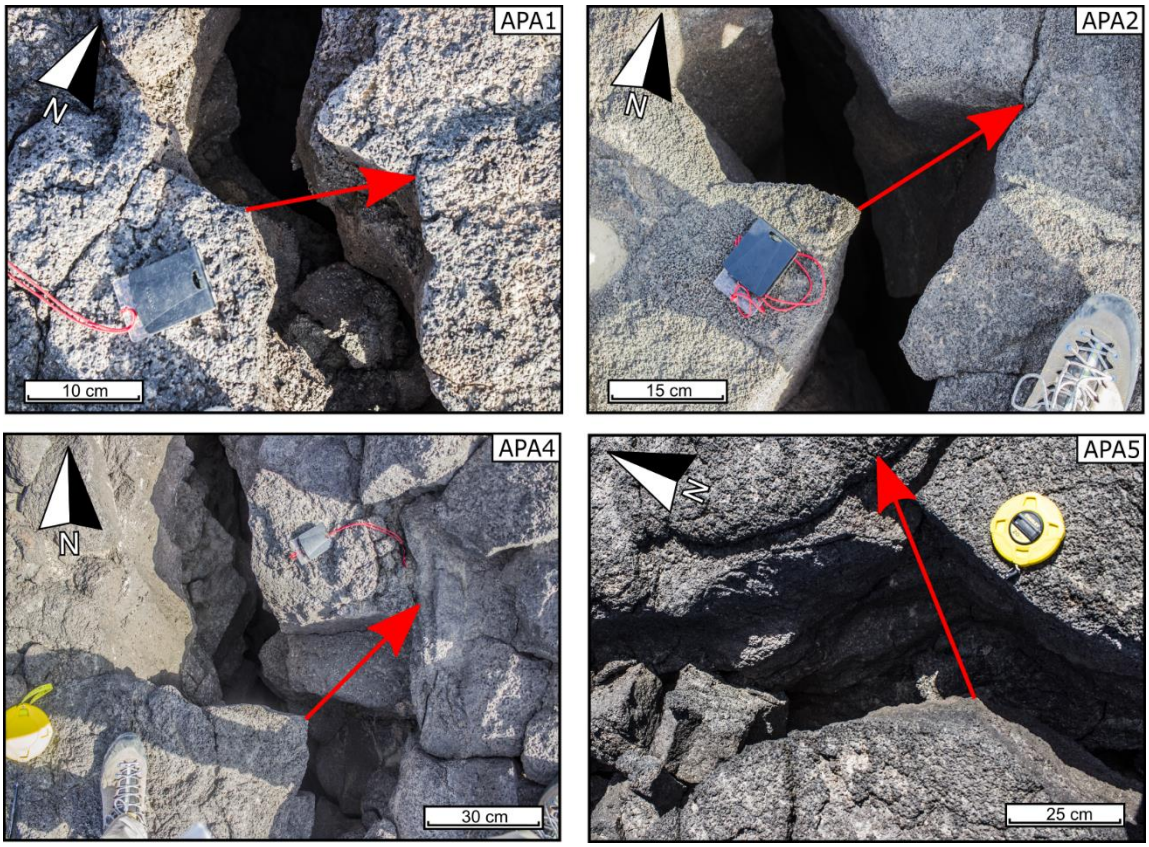

Figure 3.3 - Field measurements at the Southern tip of the Afrera Plain fault system (see Figure 3.2b for location). I reconstructed the opening direction of the fractures by finding the matching pairs of asperities on either side of fractures, following the approach of Acocella & Korme (2002). The site codes are marked in the upper right corners.

3.3 InSAR Modeling

I investigate the co-seismic deformation during the main-shock of 2 October 2007 by produced four co-seismic interferograms from ENV acquisitions in both ascending (028) and descending (278, 049, and 464) geometry (Figure 3.4). The track 464 is in I6 acquisition mode (average incidence angle 41°) while the other tracks are in I2 mode (average incidence angle 23°). The co-seismic interferograms have been processed using the JPL/Caltech ROI_PAC software (Rosen et al., 2004) and 3-arc sec SRTM DEM (Farr et al., 2007). I also produced four pre- and post-seismic interferograms to highlight eventual deformation before and after the main-shock (Figure 3.5).

The surface deformation associated to the M_w 5.1 of 2 October 2007 are shown in Figure 3.4. Both ascending and descending interferograms are characterized by a main lobe with 32 mm of range increase in the satellite Line-Of-Sight (LOS), elongated in NNW direction (Figure 3.4). A second minor lobe is also present to the North of the main lobe and it displays about half a fringe of range increase corresponding to ~15 mm of LOS displacement. The

deformation pattern in both ascending and descending tracks is similar and the elongation of the lobes perfectly matches the ~NS-striking faults (Figure 3.4), suggesting a fault slip with a normal component along a NS-striking structure. Furthermore, the pre- and post-seismic interferograms (Figure 3.5) do not shown any significant deformation before and after the main earthquake, indicating that the deformation measured by InSAR is caused by the main shock.

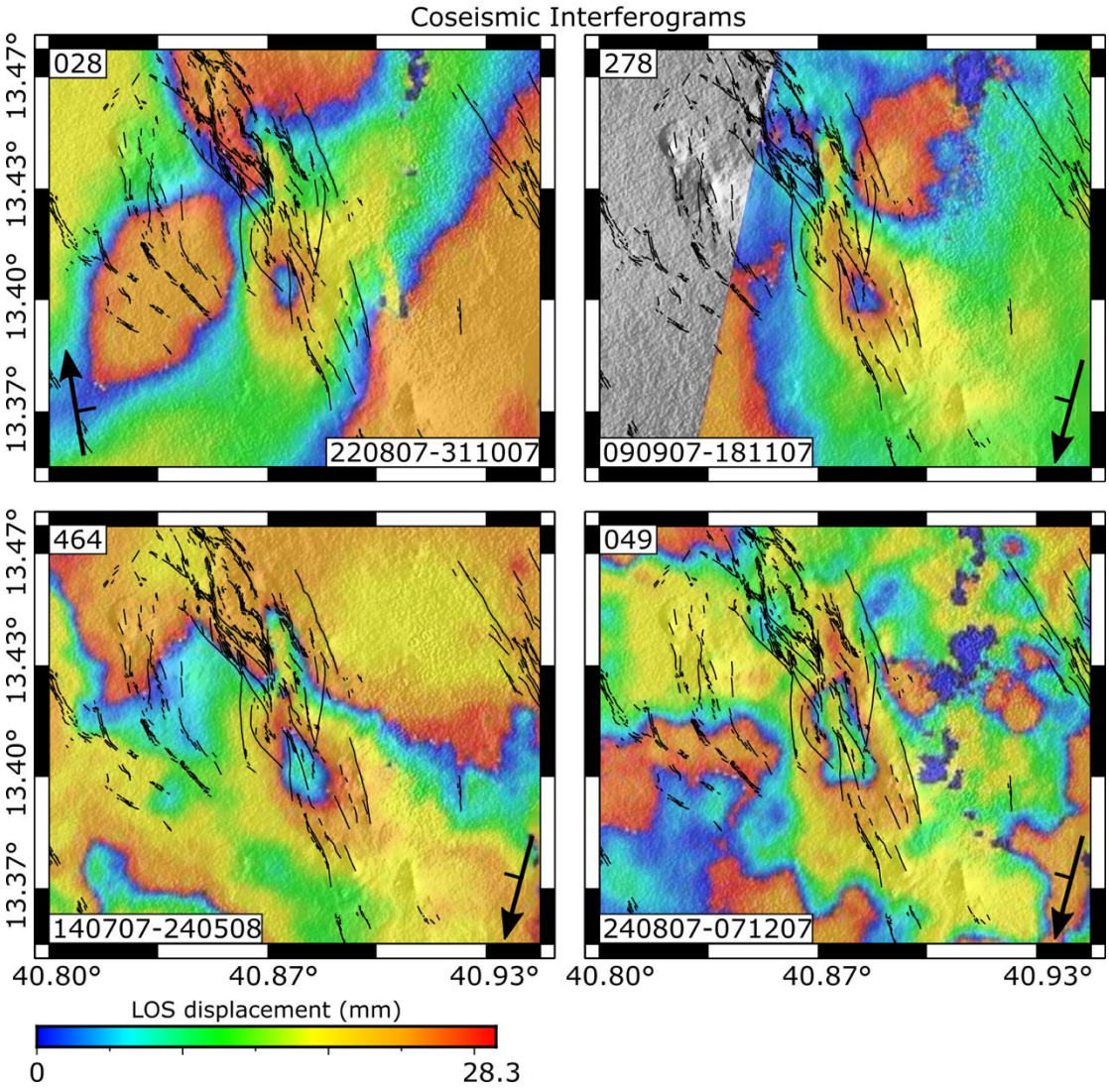

Figure 3.4 – Co-seismic interferograms processed in this study. The interferometric phase is wrapped and the colormap is given in the lower left corner. The deformation signal is located at the center with a pattern of concentric fringes indicating range increase respect to the satellite Line-of-Sight (LOS) (from blue to red). Range increase in both ascending and descending track indicates deformation characterized by a subsidence component. The patterns of irregular fringes present elsewhere in the interferograms are due to residual atmospheric and orbital noise affecting the SAR signal.

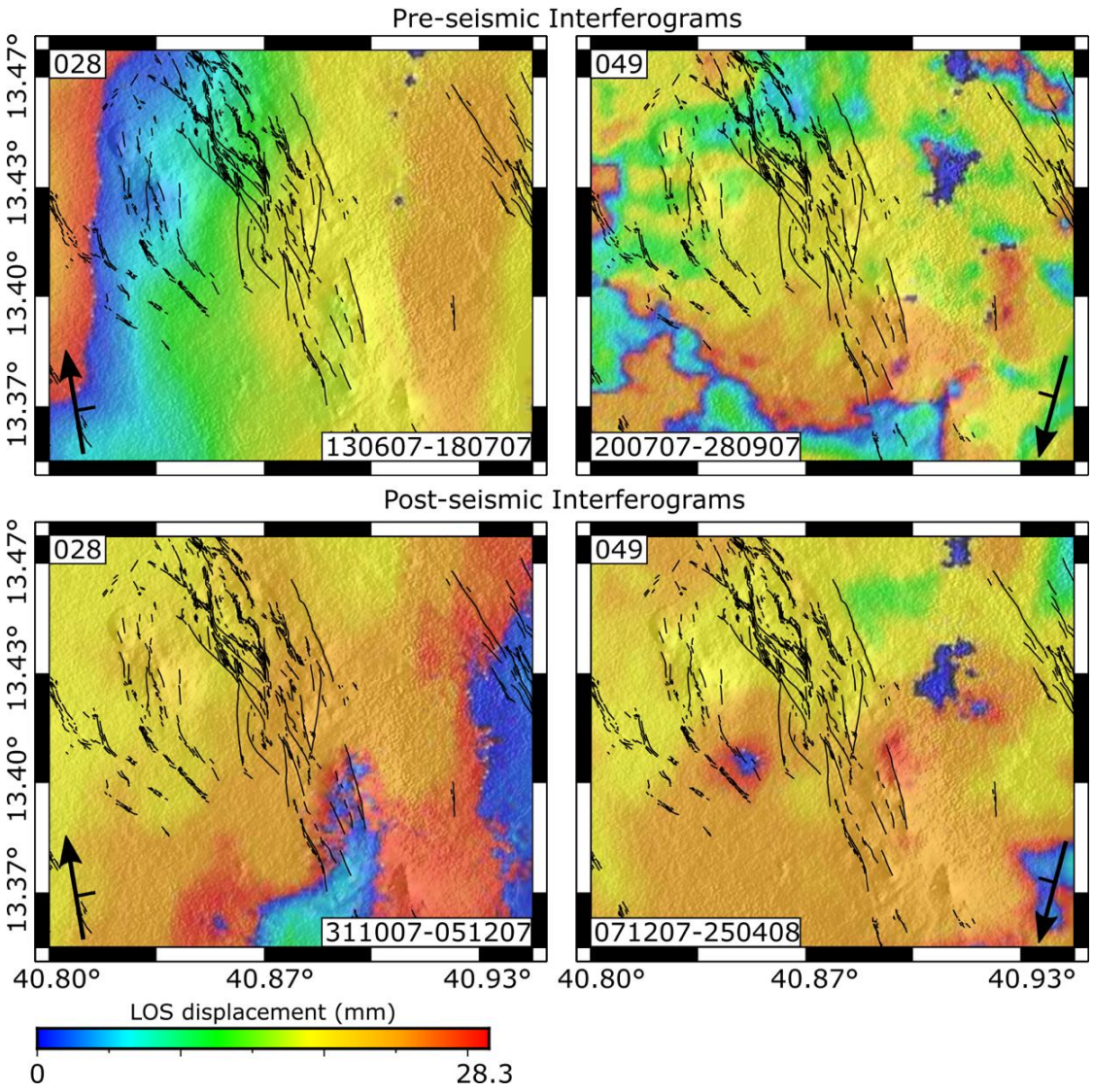

Figure 3.5 - Pre- and post-seismic interferograms processed for tracks 028 and 049. As can be seen, no deformation is present before and after the main shock.

I investigated the kinematics of fault ruptures of October 2007 by jointly inverting three ENV interferogram with the lowest level of noise (tracks 028, 278, 464). I assumed an Okada shear dislocation model (Okada, 1985) with uniform slip, within a homogeneous, elastic half-space with standard shear modulus (μ) of 3.2 x 10^{10} Pa and Poisson's ratio of 0.25. Before the inversion, I sub-sampled the interferograms using a quadtree partitioning algorithm and maximum standard deviation threshold of 1.0 mm (Figure A1) (Jonsson et al., 2002). I then estimated the best-fit fault parameters by inverting the sub-sampled interferograms through a non-linear inversion approach followed by a derivative based-procedure (Cervelli et al., 2001). This approach finds the best-fit solution by minimizing the weighted misfit between the observed data and the predicted model. The weight matrices have been calculated using a one-dimensional covariance function that approximate the

noise in each interferogram (Hanssen et al., 2001; Parsons et al., 2006). Residual orbital errors have been also removed by solving for a planar correction. In the inversion, I set relatively large bounds on the fault parameters to explore a wide range of solutions. In particular, I set the strike bounds between N270°E to N20°E. The bounds on the dip angle were set 20°–90° while I let the fault length vary between 1–7 km. I finally calculated the uncertainties on the model parameters using a Monte Carlo simulation of correlated noise (Wright et al., 2003; Wang et al., 2014). I also produced 100 simulations of the spatially correlated random noise based on the variance covariance matrices of the original interferograms. The simulated noise was added to observed data and then inverted and the 90% Confidence Interval (C.I.) for each fault parameter was finally calculated from the distribution of the model solutions. The results of the 100 nonlinear inversions and the 90% C.I. on the model parameters are shown in Figures A2, A3 and table A1, A2

The best fit model consists of two fault segments where slip is primarily accommodated by a ~3.9-km long and ~2.4-km-wide fault, striking N358°E and dipping ~37° to the east (Figure 3.6 and Table 3.2). A second smaller ~1.8-km long fault also accommodates some deformation North of the main fault. The main fault has 46 mm of normal dip slip and 103 mm of left-lateral strike slip (Figure 3.6 and Table 3.2). The main fault geometry is rather well constrained with the length and width showing narrow 90% C.I. of 3.6–4.2 km and 1.5–3.5 km, respectively. Strike-slip and normal components also have narrow 90% C.I. of 75–139 mm and 35–71 mm, respectively, while the dip is less well constrained with values ranging between 29° and 45° (Table A1). Similar kinematics characterizes the minor fault segment with dominant normal dip slip of 47 and 13 mm of left-lateral strike slip (Table 3.2). The best fit model has a total RMS of 4 mm and it gives a geodetic moment of 3.6 × 10 16 Nm corresponding to a M_w 5 earthquake (Table 3.2), in excellent agreement with the GCMT catalogue of M_w 5. Furthermore, the best fit fault model corresponds to mapped structures in the area and the oblique kinematics is similar to that of the focal mechanism from the GCMT solution (Figure 3.1a).

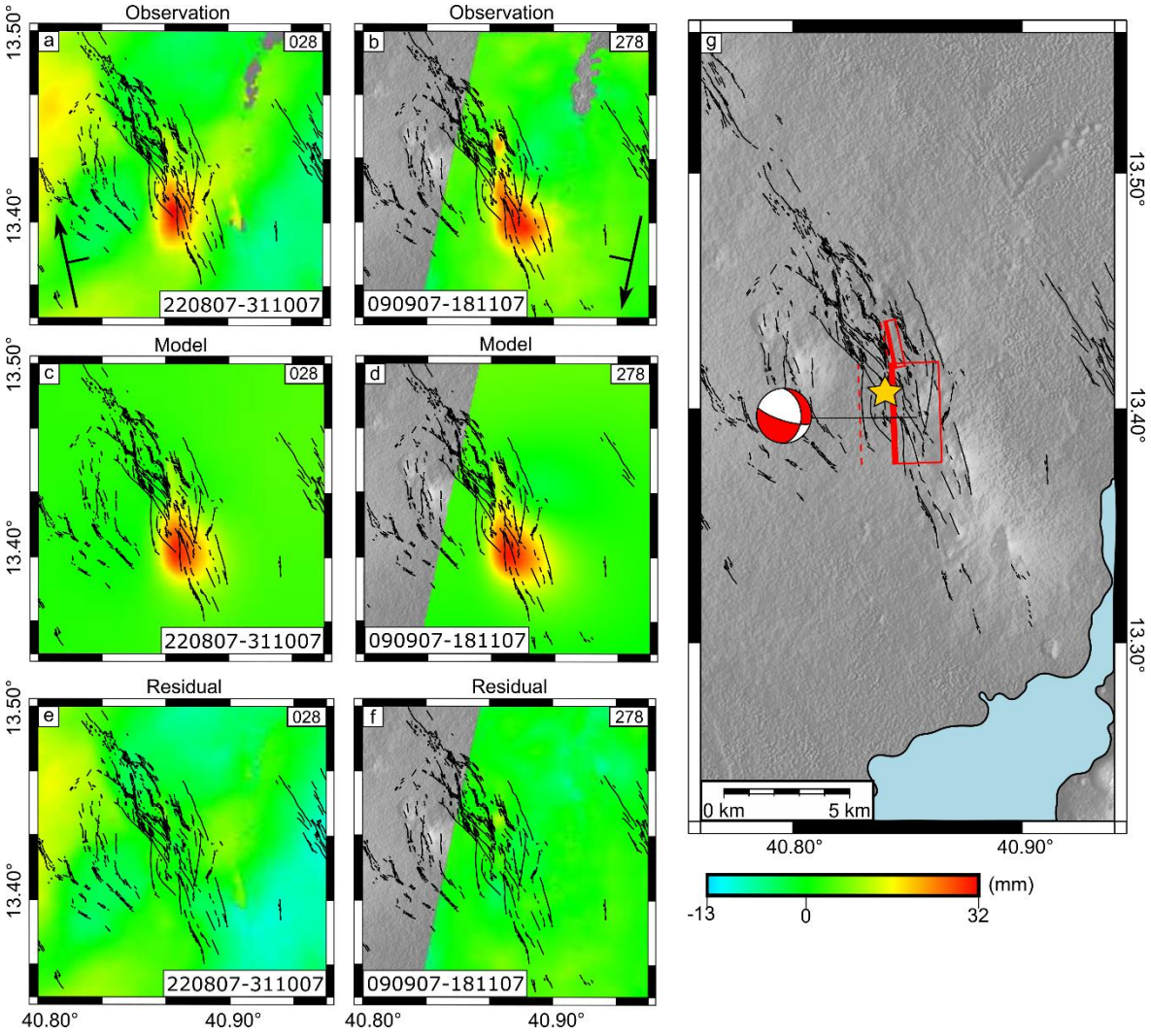

Figure 3.6 - InSAR best fit model assuming two faults. (a) Observed ascending unwrapped interferogram. (b) Observed descending unwrapped interferograms. (c) Modeled ascending interferogram. (d) Modeled descending interferogram. (e) Residual ascending interferogram. (f) Residual descending interferogram. Tracks numbers are in the top right corner, dates of first and second satellite acquisitions are given at the bottom, and all interferograms are overlapped with faults (black lines) as in Figure 3.1b. (g) Outlines of the modeled faults in map view (red boxes). The thick red line marks the upper edge of the fault and the red dashed lines are the fault projection at the surface. The red beach ball is the focal mechanism based on the best fit InSAR model. The location of the earthquake on 2 October 2007 from seismicity relocation is marked by a star.

N°	Lat. (°)	Lon. (°)	Depth (km)	Length (km)	Width (km)	Strike (°)	Dip (°)	Ss (mm)	Ds (mm)
1	13.4153	40.8692	0.93	3.87	2.36	N358E	37.5	103	46
2	13.4393	40.8684	0.32	1.84	1.00	N348E	64.3	13	47

Mo (Nm): $3.6x10^{16}$ **Mw:** 5.0

RMS: (mm)		
	T028	4.1
	T278	2.7
	T464	5.4

Table 3.2 - Best-fit faults parameters from InSAR modelling. Latitude and longitude are the coordinates of the centers of the faults upper edge. Ss is the left-lateral strike-slip component. Ds is the dip-slip normal component. RMS for each independent interferogram.

I also considered other fault geometries which could explain the observed surface deformation. In particular, I tested a model with a steeper main fault by forcing the dip angle to vary between 65° and 90°. Although a fault model with a 65° dip exists, the residuals are higher (Figure A4 and Table A3) compared to the previous 37° dipping fault. Furthermore, the distribution of the model solutions assuming a steep fault dip, 65°–90°, has all the solutions clustering at the lower bound, 65° (Figure A5), hence showing that dip angles ≥65° are too steep. Instead, the approximately normal distribution of the model solutions with dips between 29° and 45° (Figure A2 and Table A1) suggests that the best fit fault solution has a moderately shallow dip. Although this fault geometry is not fully Andersonian (Anderson, 1905), an explanation could be that the presence of preexisting weaknesses, such as other sets of faults as well as past eruptive fissures, influences the geometry and kinematics of the recent faults. These factors can explain why the Anderson theory may fail in predicting fault geometries in our study area (e.g., McKenzie, 1969; Byerlee, 1978; Celerier, 2008). I also tested a model of pure dip slip (Figure A7 and Table A4) as well as two faults corresponding to the nodal planes of the GCMT solution (Table A5). For the GCMT models, I fixed the strike, dip, and rake and let the other parameters vary. The three models showed a worse fit to the data (Figures A8, A9) compared to the preferred model. In particular, the right-lateral fault model assuming the near E-W striking plane from the GCMT solution has an unphysical geometry with a short and wide fault plane (Tables A6 and A7). I therefore prefer the first solution.

3.4 Seismic Analysis

I analyzed the seismicity accompanying the main shock of 2 October 2007 by inspecting the continuous recordings of the temporary network active in Ethiopia during that period. A description of the networks has been provided in section 2.2.6. For each event, I estimated the local magnitude (M_L) by measuring the zero-to-peak amplitude on simulated Wood Anderson seismometers, and then using the distance correction for the Danakil region by Illsley-Kemp et al. (2017). I also attempted to produce a focal mechanism of the main event, using P-wave first arrivals. However, due to the large azimuthal gap and 10–30 km distance between earthquakes and nearest station, I have not been able to obtain unambiguous solutions.

I identified 423 earthquakes from the AP during the time period from 14 July 2007 to 24 May 2008. For each earthquake, I manually picked a minimum of four P and S wave arrivals to at least three seismic stations. The detected events have been located using the non-linear probabilistic inversion approach implemented into the NLLoc software and the 2.5D seismic velocity model described in section 2.2.7. In general, high horizontal errors (ERH > 4.0 km) characterize events recorded by only three stations. To improve the spatial resolution of locations, I therefore isolated 203 earthquakes recorded by at least four stations (Figure 3.1 and 3.7), which have average horizontal errors of ±2.34 km. Most of the earthquakes are located in the top 1 km when I allow the inversion to solve for a best fit depth. I also tested the shallow locations by fixing the earthquake depths to a volume at 2–4-km depth, consistent with the fault depth achieved from InSAR modeling. These locations are very similar to those achieved by the original locations, strongly suggesting that the earthquakes are indeed in the shallow crust (Figure A12). The results show that earthquakes are mainly focused along the NNW-trending fault zone previously identified with InSAR and structural analyses and most of them occur in the area of highest co-seismic displacement. The cumulative seismic moment curve (Figure 3.1) shows that seismicity is characterized by periodic sequences of low magnitude earthquakes ($M_L \geq 4.0$) such as that accompanying the major event. The main seismic sequence lasted from 1 to 6 October, with 75 events with $M_L \geq 2.0$. The main event as also the majority of the related seismic sequence have been relocated to the area of highest co-seismic displacement (Figures 3.6 and 3.7), with a 68% confidence interval of ±2.78 km.

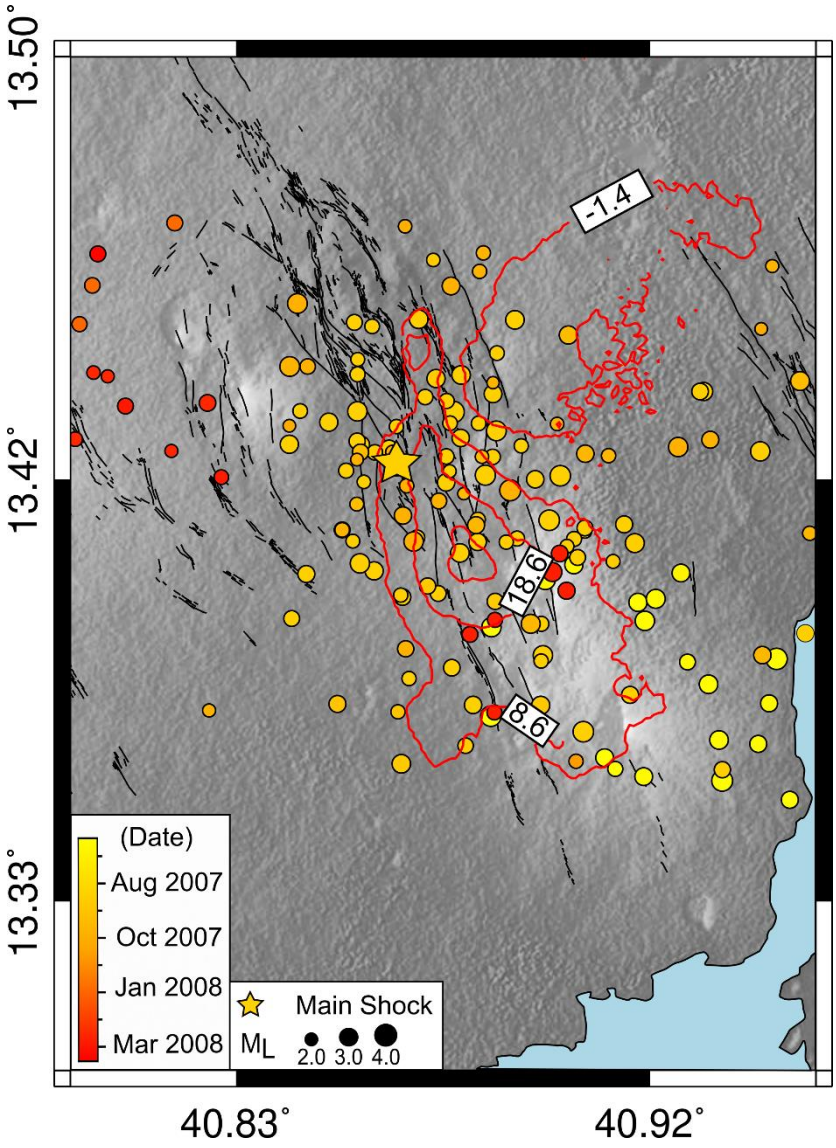

Figure 3.7 - Seismicity at AP and contours (red lines) of the co-seismic LOS displacement from the unwrapped interferogram of track 278, as in Figure 3.6. The contour line spacing is 10 mm. The figure shows that the seismicity clusters along the main fault-system and it corresponds to the area of highest co-seismic displacement.

3.5 Discussion

Using a multidisciplinary set of structural, seismic, and InSAR data I observed the tectonic processes occurring in the AP linkage zone between the EA and TA segments in Northern Afar. The faults and fissures in EA and TA strike N330°E and N328°E, respectively. GPS measurements show an ~N60°E regional extension direction (McClusky et al., 2010), strongly suggesting that rifting is orthogonal to the strike of the rift segments. Conversely, the AP shows a structural pattern consistent with a different strain field. Faults at AP have orientations varying between NNW-SSE and N-S with an average trend of ~N340°E. In the Northern part of AP, I found evidences for coexisting left-lateral and normal faulting such as

lozenge-shaped structures (Figure 3.2). These structures are predicted to form in oblique extensional settings by analogue models (e.g., McClay et al., 2002). To the South of AP, field measurements on horsetail fractures revealed local horizontal displacements with an average direction of N47°E, hence oblique with respect to the average strike of the fractures, N332°E. The relocated seismicity between 2007 and 2008 shows that earthquakes cluster along the main fault system (Figure 3.1 and 3.7). Illsley-Kemp et al., (2018b) observed swarms of seismicity in the same area during 2011–2013. The authors also interpreted focal mechanisms computed using low-magnitude earthquakes as evidence of oblique right-lateral faulting along NW-striking faults and concluded that these structures accommodate the deformation at AP while the NS-striking faults are inactive. However, my best fit InSAR model shows that the deformation caused by the M_L 5 earthquake of 2 October 2007 occurred on ~NS-striking faults with oblique left-lateral motions. Furthermore, the direction of maximum extension of my best fit InSAR model is N50°E, in agreement with the opening direction measured in the field of N47°E. The structural data and the best-fit model of the M_L 5 earthquake show that the strain at AP is primarily accommodated by left-lateral oblique slip along ~NS-striking faults. The right-lateral oblique slip along NW-SE trending faults (Illsley-Kemp et al., 2018b) could thus represent a conjugate fault population, as commonly observed in shear zones (e.g. Sibson, 1996; Davis et al., 2000; Dooley & Schreurs, 2012). The occurrence of two conjugate fault systems can be explained by a model of plate boundary kinematics where two rift segments, EA and TA, are linked by an oblique right-lateral transfer zone (Figure 3.8). Analogue and numerical models of rift linkage zones show that, at propagating rifts, rotations of the extension direction occurs which leads to oblique slip (e.g. Corti et al., 2003; Allken et al., 2011, 2013; Le Pourhiet et al., 2017). The observations at AP are consistent with counterclockwise rotation of the extension due to the formation of a transfer zones where strain is accommodated primarily by left-lateral oblique faults striking approximately parallel to the connecting EA and TA segments, while the conjugate NW-SE trending right-lateral faults are a secondary feature (Figure 3.8). I also considered other models that could explain my data. In particular the bookshelf faulting model has been used to explain shear between segments in both Southern and Northern Iceland (Einarsson, 2008; Green et al., 2014), as this model can generate transfer zones with faults subparallel to the rift segments, as observed at AP. However, the bookshelf model predicts pure strike slip, which is not consistent with the observations of oblique tectonics and range of fault strikes in Afrera. Conversely, Pagli et al., (2018) recently demonstrated

that linkage between the Red Sea and the Gulf of Aden rifts in Central Afar occurs through distributed extension in a series of rift-parallel and en-echelon basins, driving rift-perpendicular shearing at the rift tips. My results do not fit this model either, and instead provide a direct observational evidence that offset rift segments during continental break-up can be linked by a transfer zone composed of a conjugate set of oblique slip faults. Several factor can play a role in promoting the development of various types of linkage zones, encompassing the presence of pre-existing weaknesses, rift obliquity with respect to the extension direction, width of the linkage zone and the degree of overlap between magmatic segments (e.g. Corti, 2008, 2012; Brune et al., 2017; Allken et al., 2011, 2013; Le Pourhiet et al., 2017). Furthermore, it has been shown that linkage zones can evolve from transfer zones to a fully developed transform offset, where the two rift segments are linked by a narrow zone of extension-parallel strike-slip faulting (e.g. Taylor et al., 2009; Gerya 2013; Allken et al., 2011, 2013; Le Pourhiet et al., 2017). These topics are still matter of debate and, in the case of the AP, if and when the transfer zone evolve to a transform offset is not known.

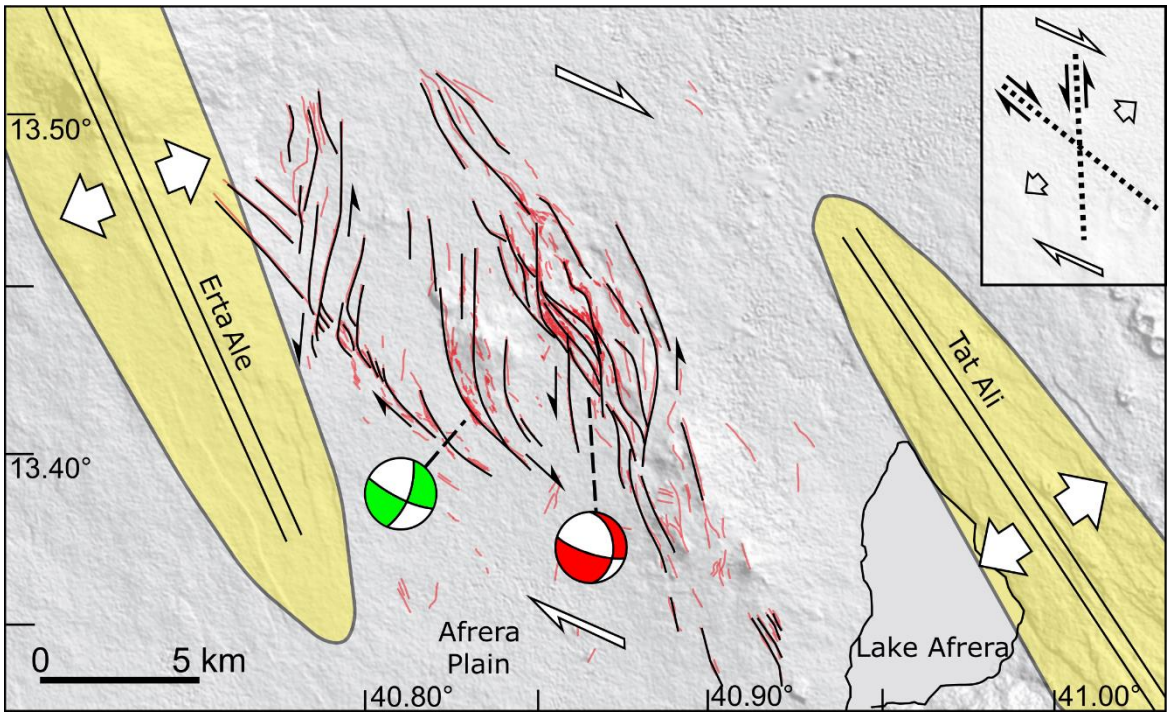

Figure 3.8 - Kinematics of the Afrera Plain transfer zone. The red beach ball is the focal mechanism computed in this study based on InSAR inversion. The green beach ball is the focal mechanism reported in the area by Illsley-Kemp, et al. (2018b).

3.6 Conclusion

In this chapter I investigated the tectonic activity of the AP, at the interaction between the EA and TA segments in Northern Afar, by integrating structural, InSAR and seismic data. I observed that the AP is characterized by a main central fault system made by major faults striking in a ~NS-direction. The area shows continuous low-magnitude seismicity along with a major M_L 5 earthquake occurred the 2 October 2007. Structural measurements of kinematics indicators, along with InSAR models of the October 2007 co-seismic deformation, indicate that the main central fault system is characterized by dominant oblique left-lateral faulting along a ~NS-striking, East-dipping fault-segments. Additionally, minor seismicity associated with oblique right-lateral faulting has been also observed by Illsley-Kemp et al. (2018b).

I combined all these observations to propose a kinematic model for the AP linkage zone. My results can be interpreted in a kinematic framework where the EA and TA magmatic segments are interacting through a right-lateral transfer zone, characterized by dominant left-lateral oblique slip along major ~NS-striking faults (Figure 3.8). Oblique right-lateral faulting could by associated to a minor conjugate fault population as observed in many shear zones. These results contribute to the now growing body of observations for a wide variety of strain types that can link rift segments.

4. Plate-boundary kinematics of the Afrera linkage zone

InSAR, seismicity and structural observations showed that the Afrera Plain (AP) is an active linkage zone where oblique fault slip occurred on a ~NS-oriented fault. In this chapter I use InSAR and seismicity to understand how the deformation is accommodated across the entire AP linkage zone, the kinematics of different faults, and whether deformation is episodic or time-progressive. Figure 4.1 summarizes the seismicity recorded in the area by local seismic networks during 2005-2013 (Belachew et al., 2011; Illsley-Kemp et al., 2018; seismicity in Chapter 3), showing that seismicity in Afrera is widespread. To understand the fault kinematics in this linkage zone, I processed the SAR data from ENVISAT (ENV) and Sentinel-1 (S1) catalogues spanning the time periods 2005-2010 and 2014-2019, and I analyzed the seismicity recorded by the two local seismic networks active in Ethiopia during 2017-2018 (Keir et al., 2020). The SAR data have been used to produce time-series of incremental deformation and the related uncertainties. Here, I identified both time-progressive and episodic deformation along different faults. Episodic deformation was associated with seismic a sequence in January 2018 in a similar manner as observed in 2007 (Chapter 3), but time-progressive deformation is also observed across the AP.

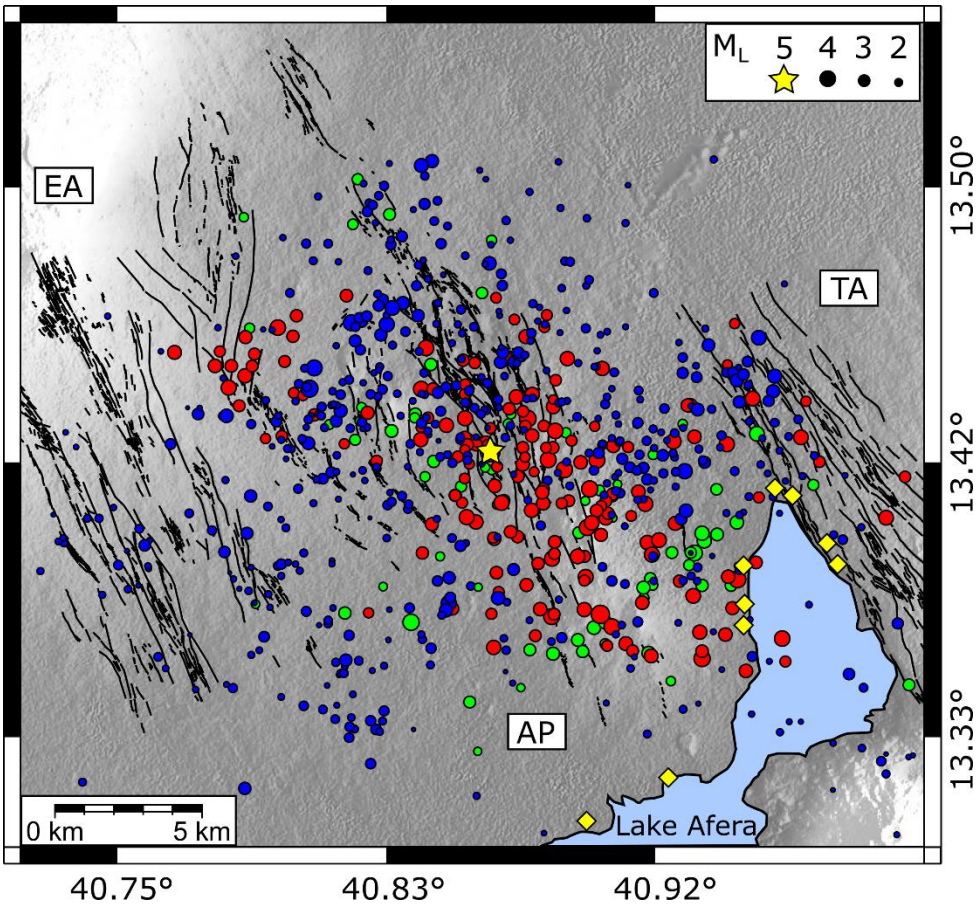

Figure 4.1 – Distribution of seismicity recorded by local networks during 2005-2013. The green dots are the seismicity between 2005 and October 2007 reported by Belachew et al. (2011). The red dots are the seismicity relocated in this thesis and shown in Chapter 2. The blue dots are the earthquakes occurred during 2011-2013 (Illsley-Kemp et al., 2018). The yellow diamonds are the hydrothermal springs reported in the area by Brinckmann et al. (1970). EA=Erta Ale, AP=Afrera Plain, TA=Tat'Ali.

4.1 InSAR and Seismic Data

I analyzed large SAR datasets acquired in the area by the European satellites ENV and S1, covering the AP linkage zone and spanning the time periods 2005-2010 and 2014-2019 to investigate how deformation is distributed across a linkage zone (Figure B1). I also looked into using X-band, Cosmo-SkyMed satellite data, but no acquisitions have been made over the AP. I finally analyzed the local seismicity recorded by the two temporary seismic networks active in Ethiopia during 2017-2018 (Keir et al., 2020).

4.2 InSAR Data processing

I formed 92 interferograms from SAR images of the ENV satellite in both ascending (track 028) and descending (track 049) geometries from 2005 to 2010. ENV interferograms were generated using the ROI_PAC software developed by JPL/Caltech and corrected for

topographic phase contribution using an external 3-arc sec (~90 m resolution) SRTM DEM (Farr et al., 2007). Interferograms were then filtered using a power spectrum filter (Goldstein & Werner, 1998) with strength of 0.6 and unwrapped using the ICU branch-cut algorithm (Goldstein et al., 1988). The unwrapped interferograms were then geocoded using the same SRTM DEM. I also produced 142 interferograms from S1 satellite images in both ascending and descending tracks (014 and 079) for the 2014-2019 period, using the JPL/Caltech/Stanford InSAR Scientific Computing Environment (ISCE) software package (Rosen et al., 2012). The SLCs co-registration and the topographic phase removal were performed using a 1-arc sec (~30 m resolution) SRTM DEM (Farr et al., 2007). Residual noise and decorrelation were then filtered with an adaptive power-spectral filter with strength of 0.5 (Goldstein & Werner, 1998). Interferograms were then unwrapped with the ICU branch-cut method (Goldstein et al., 1988) and geocoded to the 1-arc sec SRTM DEM.

4.2.1 InSAR co-seismic deformation

The first co-seismic deformation observed with InSAR in the AP was that associated to the M_L 5 of 2 October 2007. This has been already discussed in Chapter 3. A visual inspection of S1 interferograms allowed me to identify a new episodic event that occurred in the area in January 2018 (Figure 4.2). The InSAR signal is consistent with a fault slip and it consists of a deformation pattern elongated in ~NS direction and a main lobe with ~17 mm and ~19 mm of range increase in the satellite Line-Of-Sight (LOS), in ascending and descending orbits, respectively. The deformation is located East of the Afrera central fault system and it is consistent with faulting with a dominant normal component (Figure 4.2). The deformation signal also has a smaller maximum South of the main one in both independent ascending and descending interferograms, suggesting that fault slip also occurred on a minor fault segment (Figure 4.2).

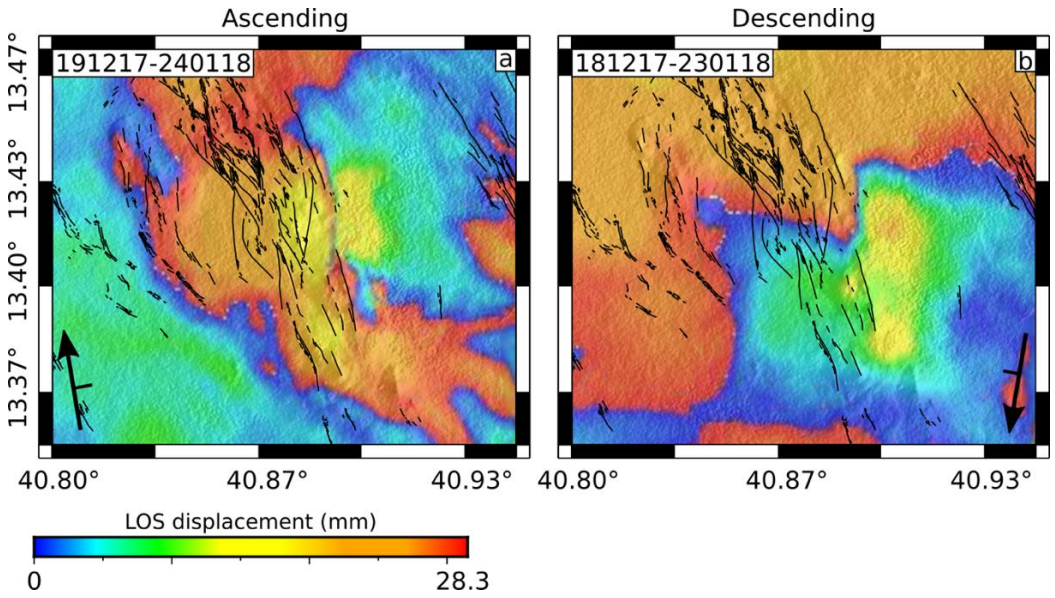

Figure 4.2 – S1 interferograms covering the event of January 2018. Both the interferograms span a time period of 36 days. The interferometric phase is wrapped and expressed in mm, with positive values (blue to red) indicating range increase.

4.2.2 InSAR Time-Series Analysis

I estimated time-series of incremental satellite LOS (Line-Of-Sight) displacements and their uncertainties for each InSAR track, using the Π-Rate software (Wang et al., 2012). I analyzed 51 interferograms for ENV ascending track 028, 41 for ENV descending track 049, 55 for S1 ascending track 014, and 87 for S1 descending 079 (Figure B1). For the time-series analysis, I used the entire available ENVISAT datasets, while I performed a selection on the large S1 datasets to favor interferometric pairs with both small spatial and temporal baselines. Further details on the interferogram pair selection to create the S1 networks are provided in Figure B1. To reduce the noise, I also multi-looked the S1 interferograms to a pixel size of 90m-by-90m, which is also the same resolution as for the ENV interferograms. Unwrapping errors were first identified in ENV data by adopting a phase closure method on Minimum Spanning Trees, while the excellent level of coherence in S1 data and lack of dense fringe patterns meant unwrapping mistakes were not a problem. Using a network approach, I applied orbital filtering to the geocoded interferograms by fitting them with a linear-function (Biggs et al., 2007). I also removed topographically correlated atmospheric noise and applied Atmospheric Phase Screen (APS) filter to minimize all other atmospheric disturbances (Elliott et al., 2008).

During the observation period, two main seismic episodes occurred in the study area in October 2007 (as discussed in Chapter 3) and January 2018. In order to analyze separately

the time-progressive and the episodic deformation, I extracted the sudden displacements in 2007 and January 2018 from the time-series using the cross-correlation technique (Pagli et al., 2014) before applying the APS filter. Figure B2 show the results of cross-correlation in S1 data.

The only other sudden displacement that occurred in Afar during the observation period is the 2005-2010 intrusion at Dabbahu (Ebinger et al., 2008) and the 2017 Erta Ale eruption (Xu et al., 2017; Moore et al., 2019), both of which occurred outside of our study area. Dabbahu is ~100 km away from the AP and our ENV dataset starts from October 2005, hence after the main intrusion occurred. The area affected by the Erta Ale volcano deformation is to the North of the AP but outside of the selected study area.

After sudden displacement was identified and extracted from the interferogram (Figure B2), I then applied APS using a combination of temporal high-pass and spatial low-pass filter with a temporal Gaussian filter with length of 0.5 years followed by a spatial Butterworth filter with low-pass cutoff estimated from the variance-covariance matrix of the spatially correlated noise. Finally, the sudden displacements of October 20007 and January 2018 have been added back to the time-series after the APS filtering.

4.2.3 Time-Series Results: 2005-2010

The cumulative time-series show three deforming areas of range increase (positive values) in both ascending and descending ENV tracks (Figures 4.3). The deformation patterns correspond to en-echelon ~NS-striking faults mapped in the area. The range increase in both tracks is consistent with a dominant down-dip motion of the hanging-walls along 2-5 km-long, East-dipping faults. The time-series of cumulative displacements also show that deformation is accommodated in different manners across the AP linkage zones (Figure 4.3 and 4.4). Both sudden episodes, such as in October 2007 (pixel 1), but also time-progressive continuous deformation (pixels 2 and 3) occur along different sub-parallel faults during the observation period (Figure 4.3 and 4.4). The total range increase along episodically deforming faults (~30-40 mm) is higher than those deforming continuously (~10-30 mm), suggesting that episodes of faulting accommodated more strain than progressive fault creep during 2005-2009.

The InSAR observations show that faulting along ~NS-striking East-dipping faults is the dominant mode of deformation in the AP during 2005-2010. This is also consistent with

InSAR and seismicity models of the M_L 5 earthquake in 2007 (Chapter 3). To further investigated the relationship between seismicity during 2005-2010 and tectonic deformation, I compared the distribution of seismicity recorded by Belachew et al. (2011), Illsley-Kemp et al. (2018), and the relocated seismicity in Chapter 3, to the InSAR time-series during the same time-period. To this aim, I analyzed the seismicity in the three different deforming areas as identified by InSAR (Figure 4.4). As can be seen in Figure 4.4, the highest seismic activity clearly occurs in the central fault system during the main shock of October 2007, yet minor seismicity also accompanies time-progressive deformation in the areas around pixel 2 and 3.

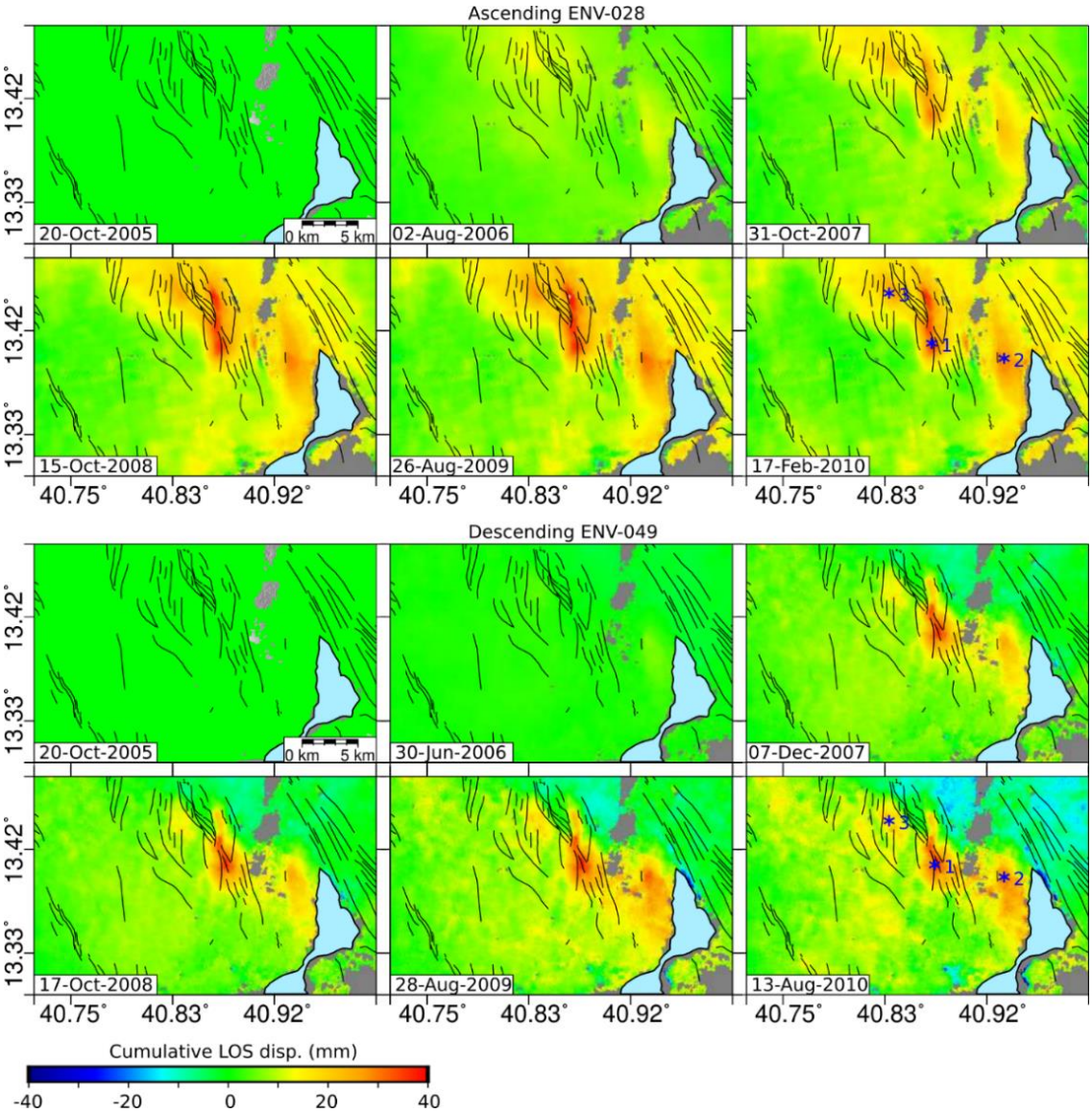

Figure 4.3 – Maps of cumulative deformation respect to the satellite LOS at different epochs (~1 year) from ENV data. The blue, numbered point in the maps show the location of the curves in Figure 4.4.

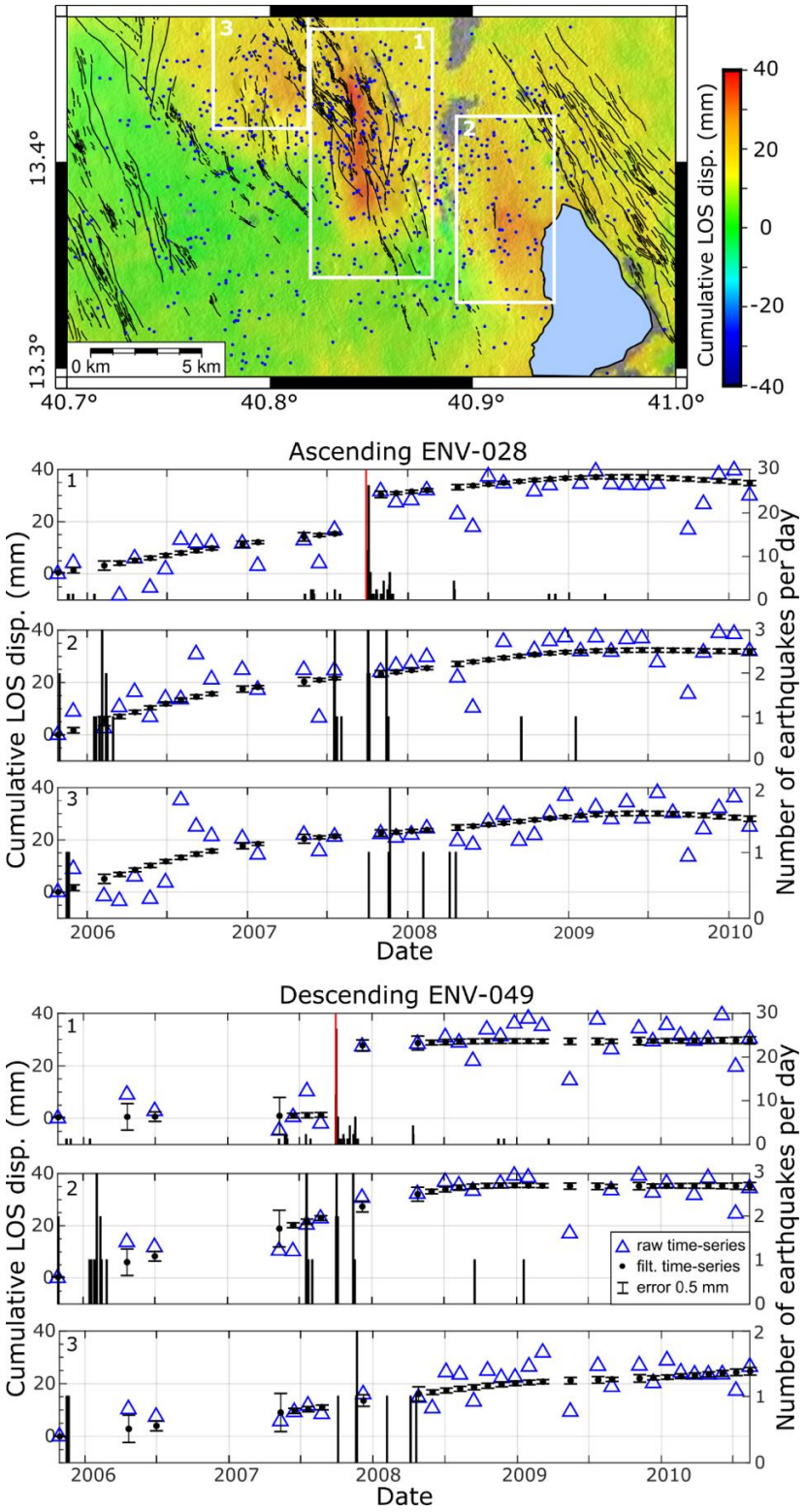

Figure 4.4 – Time-series of cumulative LOS displacements (including sudden episodes) extracted from pixels in Figure 4.3. The blue triangles show the raw time-series while the black dots are the final inverted displacements. The error bars are scaled and the scale is reported in the legend. The black histograms report the seismicity during the same time-period while the red line marks the main shock of 2 October 2007.

4.2.4 Time-Series Results: 2014-2019

The S1 cumulative time-series show three main deforming areas of range increase both in the ascending and descending tracks (Figure 4.5 and 4.6). The deformation patterns are consistent with motions along short, ~NS-striking fault planes. A fault that was active during the 2005-2010 period also continued deforming in 2014-2019 (pixels 2 in Figure 4.6 and 4.7), while episodic fault slip in January 2018 also occurred (pixel 4 and 5 and Figure 4.2).

The time-series at pixel 4 shows that the episodic deformation ruptured to the East of the 2 October 2007 episode, confirming that extension in the center of AP is accommodated by episodic slip along different fault segments. The episode at pixel 4 also corresponds to a seismic sequence including M_L ~5 events from 10 January 2018 to the 31 January 2018 (the seismicity will be analyzed in detail in sections 4.3 and 4.4). To the East of the episodic event, the time-series at pixel 2 shows that time-progressive deformation is still ongoing similar to what observed during 2014-2015 (Figure 4.5 and 4.6). In general, the time-series in descending track show higher deformation around pixel 2 (~40 mm) with respect to those measured in the same area in the ascending track (~20 mm). This is due to another episodic surface deformation occurred North of the Afrera lake in February 2018. As can be seen in Figure 4.7, the pattern has a lobe with ~19 mm of range increase that matches a short, ~NNW-striking, West-dipping fault bounding the Eastern shore of the lake (Bonatti et al. 2017). The pattern is small and is observed just in the descending track likely due to a favorable orientation of the fault with respect to the satellite LOS. However, the presence of the signal in two independent interferograms confirm that signal is associated to real deformation, rather than to noise in the area.

As performed for the other episodic events, I attempted to extract such episodic deformation before the APS filter using the cross-correlation. However, the cross-correlation didn't successfully extract the deformation, likely due to the fact that one of the correlated interferogram spans both the January and February 2018 events (e.g. Figure 4.7b). Therefore, some of the February 2018 deformation remains in the time-series analysis but it has been minimized by using the APS filter. With this in mind, it can still be observed that deformation at the eastern tip of the AP is higher (up to 40 mm) than those measured during 2005-2010, indicating that such faults are now accommodating more deformation (Figure 4.5). Furthermore, some far-field deformation during February 2018 also contribute to the range

increase measured in the descending track at pixel 2, which resulted in a higher cumulative deformation (Figure 4.5 and 4.6).

Finally, the time-series from ascending track 014 also show a pattern of range increase in the Western sector of AP (Figure 4.5), where time-progressive deformation have been observed during 2005-2010 (pixel 3 in Figure 4.3 and 4.4). Such pattern could be related to ongoing deformation along the same faults observed in ENV data. However, the pattern is not present in the descending time-series and cannot be confirmed.

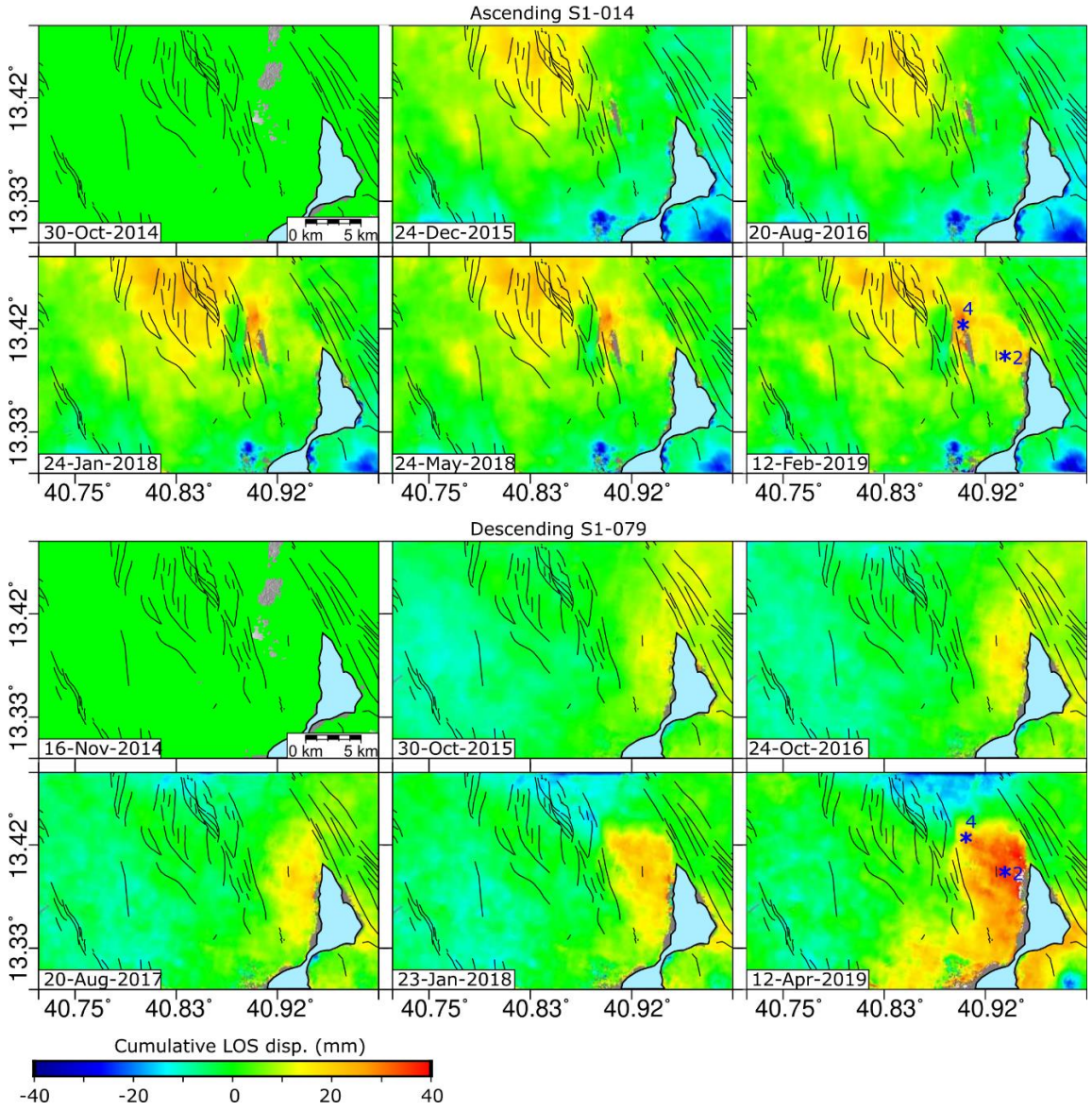

Figure 4.5 - Maps of cumulative deformation respect to the satellite LOS at different epochs from S1 data. A gap in 2017 is present in the ascending track due to lack of acquisitions in that period. The blue, numbered point in the maps show the location of the curves in Figure 4.6.

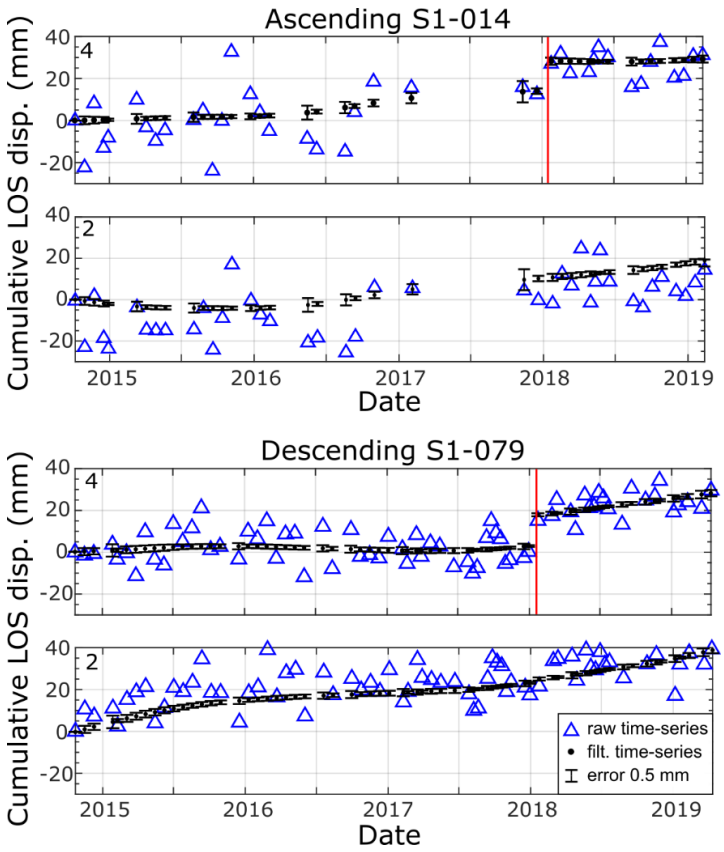

Figure 4.6 - Time-series of cumulative displacements in the satellite LOS extracted from pixels in Figure 4.5. The blue triangles show the raw time-series while the black dots show the filtered ones (including sudden episodes). The error bars are scaled and the scale is reported in the legend. The red lines mark the co-seismic deformation of January2018.

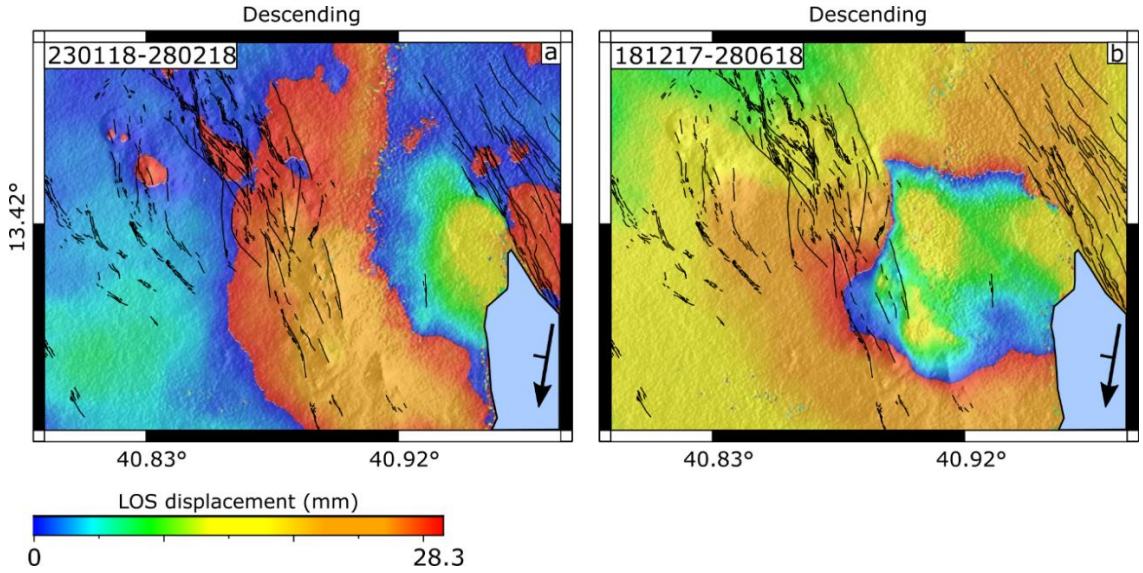

Figure 4.7 – S1 independent interferograms covering the event of February 2018. The interferograms span a time period of 36 days (a) and ~192 days (b). The interferometric phase is wrapped and expressed in mm, with positive values (blue to red) indicating range increase. Both the events of January and February 2018 are present in b).

4.3 InSAR Modeling

I modelled the deformation pattern observed in January 2018 by jointly inverting two S1 independent interferograms from both ascending (014) and descending (079) orbits assuming uniform fault slip across one fault plane in a conventional elastic half-space (Okada shear dislocation; Okada, 1985). For the modelling I tested several solutions by attempting to invert both the original interferograms and those extracted with cross-correlation. Initially, I inverted two 36-days long independent interferograms, (this is referred as Model 1). The interferograms were sub-sampled using the quadtree partitioning algorithm from Jonsson et al. (2002) and a maximum standard deviation (STD) threshold of 0.7 mm. For Model 1, I set narrow bounds on the location and strike of the fault (between N330°E and N30°E) according to the strike of mapped structures, while I let the other parameters free to vary. The best-fit Model 1 solution consists of a ~NS-striking fault (N357°E) dipping to the East with an angle of 67° (Figure B3). The fault is oblique with left-lateral (~33 mm) and normal (~45 mm) components (Figure B3). Model 1 has relatively low Root-Mean-Square (RMS) residuals of ~3 mm in both ascending and descending tracks (Table B1). However, the fault plane has an anomalous aspect ratio with a width of ~10 km and a length of 3.5 km (Figure B3 and table B1). Furthermore, the best-fit fault width corresponds to the upper bound of the search window.

I then constrained the bounds on the fault width to be between 1-3 km (this is referred as Model 2) (Figure B4). Model 2 shows that a solution with a 3 km fault width exists and the model is again an oblique left-lateral fault with geometry and kinematics comparable to Model 1. The fault strikes ~N358°E and dips ~76° to the East. The slip has 69 mm of left-lateral slip and ~55 mm of normal component slip, resulting in a geodetic M_w 5 (Figure B4 table B2). Model 1 and Model 2 show similar RMS residuals of ~3 mm in both ascending and descending tracks (Table B2), yet Model 2 has a geologically reasonable fault aspect ratio (Figure B4). Since the deformation pattern is relatively small, the results of the inversion could cause a model-misfit space characterized by more local minima (Cervelli et al., 2001)).

Finally, I also inverted the January 2018 deformation signals as extracted from the time-series processing using the cross-correlation method (this is referred as Model 3). This allowed me to run the inversion excluding most of the noise affecting the original interferograms. The cross-correlated interferograms have been again quadtree partitioned

(Jonsson et al., 2002) using a maximum STD threshold of 0.5 mm. A low STD threshold has been possible thanks to the low noise affecting the signal and allowed me to sample the deformation with higher spatial resolution. For the modelling, I again set relatively large bounds, except for the fault strike. Model 3 is again an oblique left-lateral fault striking N359°E and dipping to the East with an angle of ~68°. The fault length is 3.6 km-long and 4.8 km-wide (Figure 4.8 and Table 4.1). The fault has a dominant normal component of ~39 mm associated with a left-lateral slip of 13 mm. Model 3 has RMS residuals comparable to the previous solutions and equal to 2.7 mm and 3.2 mm in ascending and descending tracks, respectively (Table 4.1). The geodetic moment is $2.3x10^{16}$ corresponding to a M_w 4.9 (Table 4.1). I also calculated the uncertainties associated to each model parameter by adopting the Monte Carlo simulation of correlated noise (Wright et al., 2003; Wang et al., 2014). I used the variance-covariance matrices of the input data to create 100 simulations of spatially correlated random noise. Such simulations have than been added to the input data and inverted (Figure 4.9). The 90% Confidence Interval (CI) for each parameter has been calculated from the distribution of the 100 solutions (Table B3). The 90% C.I. for the fault length and width range between 3.5-3.7 km and 4.2-5.4 km, respectively. Normal slip is very well constrained with a 90% C.I. of 3.8-4.1 cm, as is also the strike-slip component with a 90% C.I. of 1.1-1.5.

To summarize, all the models show similar fault kinematics characterized by oblique left-lateral slip along ~NS-striking faults. The low variability in strike, kinematics and magnitude suggests that these parameters are rather well constrained. Using the cross-correlation (Model 3) has resulted in a great improvement in the quality of the input data, reducing the noise and the related local minima in the miss-fit space, and allowing the inversion greater freedom to search for the global minimum. This is also testified by the very low variability in the fault parameters shown by the 100 Monte Carlo simulations (Figure 4.9) and by the narrow 90% CI for the best-fit solution (Table B3). Models 2 and 3 have similar fault geometries and kinematics, however, since no constrains have been imposed on the search across the model-misfit space in Model 3, I favor that solution. The kinematics of Model 3 is also similar to the event of October 2007, suggesting that oblique slip along NS-striking is the dominant mode of deformation in the central faults of the AP.

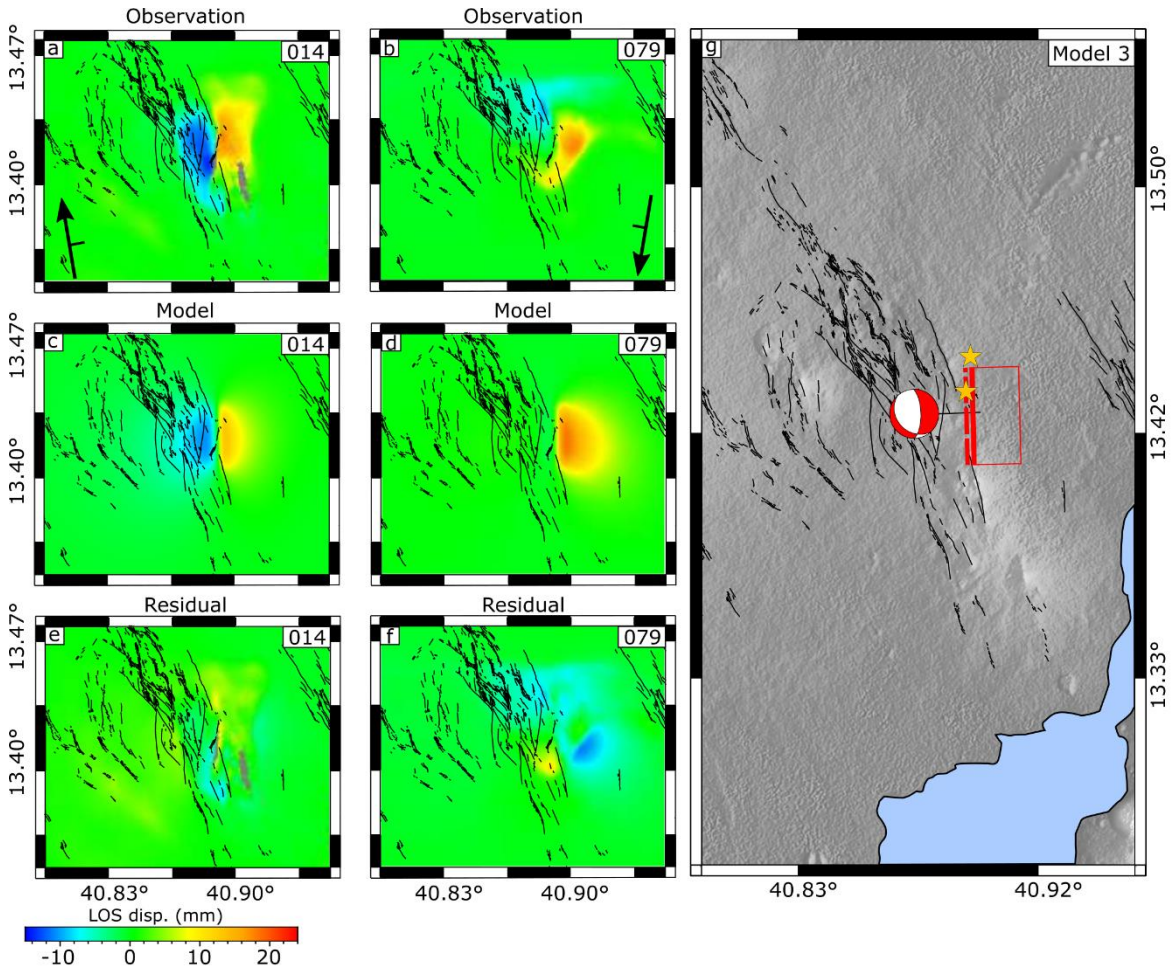

Figure 4.8 – Best-fit fault model (Model 3). a, b) cross-correlated deformation. c, d) model and e, f) residuals. The red beachball is the geodetic focal mechanism while the red square is the fault plane. The red dashed line is the projection of the fault top at surface. The two, orange stars are the major earthquakes occurred in January 2018.

Lat. (°)	**Lon. (°)**	**Depth (km)**	**Length (km)**	**Width (km)**	**Strike (°)**	**Dip (°)**	**Ss (mm)**	**Ds (mm)**
13.4226	40.8928	0.41	3.60	4.79	N359E	67.8	13.1	39.3
Mo (Nm): 2.3x1016			**Mw:** 4.9					
RMS: (mm)	**T014**	2.70						
	T079	3.24						

Table 4.1 - Model 3 parameters. Latitude and longitude are the coordinates of the center of the fault upper edge. Ss is the left-lateral strike-slip component. Ds is the dip-slip normal component. RMS for each independent interferogram.

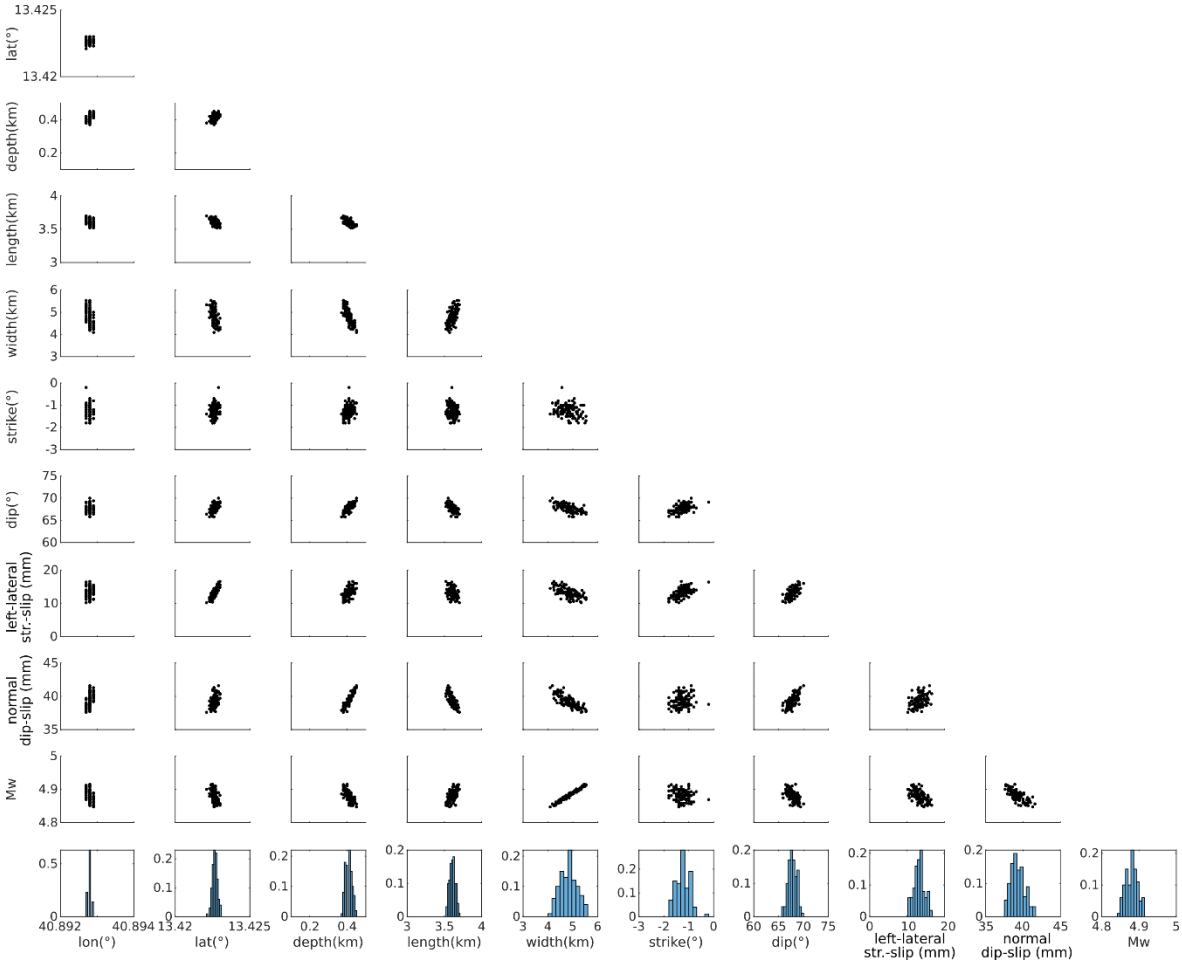

Figure 4.9 - Distribution of the Model 3 parameters computed using 100 Monte-Carlo simulations. The scatter plots show the parameters trad-off while histograms show the distribution of the individual model parameters.

4.4 Seismic Analysis

I investigated the seismicity accompanying the main fault slip in January 2018 by analyzing the data recorded by the recent seismic network deployed in Afar during 2017-2018 (Keir et al., 2020). I inspected one month of continuous seismic recordings, from 1 January to 31 January 2018 to identify all the earthquakes during that period. I found a total of 499 events with the first P-wave arrival at station N009 (located at Afrera) and manually picked both P and S waves for earthquakes recorded by four or more stations. I then located the events using the Oct-Tree search algorithm implemented into the NLLoc software (Lomax et al., 2000) and the 2.5D velocity model of Afar described in section 2.2.7. I finally estimated local magnitudes (M_L) by measuring the zero-to-peak amplitude on simulated Wood Anderson seismometers, and applying the distance correction for the Danakil region from Illsley-Kemp et al. (2017).

All the 499 located earthquakes cluster at the AP, along the main NNW-trending fault system and occur within the upper crust (1-10 km) (Figure 4.10) with average horizontal and vertical errors of ±2.8 km and ±2.2 km, respectively. The seismic sequence started on the 10 January 2018 with a main-shock of M_L ~5.2±0.3 at a depth of 9±4 km. The main-shock was followed by several events with $M_L > 4.5$ along with another shallower (~2 km) M_L 5.1±0.4 on the 11 January (Figure 4.10). The hypocentral locations are consistent with the InSAR time-series indicating that the two major earthquakes occurred East of the M_L 5 of October 2007. However, just a single fault was assumed in the modeling of the interferograms as the two events could not be separated temporally in both ascending and descending tracks. Since the depth of the M_L 5.1 on 11 January was shallower (2.6 km) than the M_L 5.2 main-shock on 10 January (~ 9 km), it is likely that the deformation imaged by InSAR is mainly due to the shallow earthquake, while the deeper M_L 5.2 does not contribute much to the surface deformation. This is also supported by the very good correspondence between the hypocentral depth estimated from both InSAR inversion (2.6 km) and seismic data (2.0 km) for the 11 January earthquake.

The rest of the seismic sequence seems instead to be shifted to the West (Figure 4.10) likely suggesting that some small slip along other fault segments was triggered by the two major earthquakes. Furthermore, the curve of the cumulative seismic moment release (Figure 4.10b) also shows a sequence of foreshocks preceding the main event during the two days before (8 and 9 January). I also attempted to process focal mechanisms for the events with $M_L > 4.5$. However, due to the large azimuthal gaps of the seismic network in the study area, I have not been able to obtain unambiguous solutions. I thus tried to reduce the azimuthal gap by also considering the P-wave arrivals at the permanent station ATD, located in Djibouti (https://www.fdsn.org/networks/detail/G/). However, including this station result in a worse earthquake location, with earthquakes drifting away from the area of highest co-seismic deformation identified with InSAR.

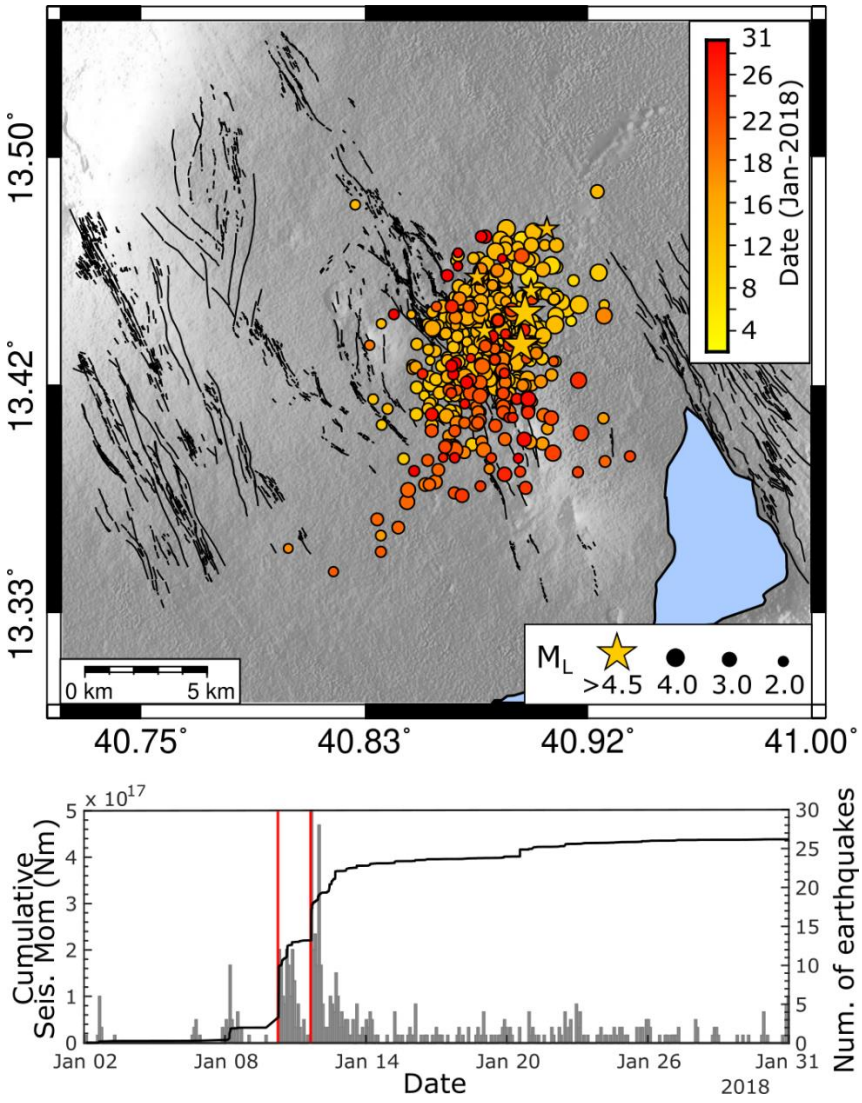

Figure 4.10 – a) Seismicity located in Afrera between 1 and 31 January 2018 with faults and fractures (black lines). b) Cumulative seismic moment release and number of earthquakes during the same time-period. The two red lines in b) mark the two major events of 10 and 11 January. The histogram plot has a binning of 12 hours.

4.5 Discussion

I used InSAR time-series and modeling, along with seismic data to document the present kinematics of the AP linkage zone in Afar. This dataset, combined with the previous study on the AP (Chapter 3), shows how the deformation is distributed across a linkage zone formed by the interaction of the Erta Ale and Tat'Ali magmatic segments. I show that en-echelon, ~NS-striking faults accommodate deformation at AP. In the analyzed time-period, different individual faults are observed to be active at different time periods suggesting that deformation is not localized to one fault at Afrera, but instead occurs on multiple faults in the fault network.

The major deformation patterns observed at the AP match the surface expression of East-dipping faults. This is also supported by the East-dipping faults modeled from InSAR data for the major earthquakes that occurred in October 2007 (Chapter 3) and January 2018 (this Chapter). In addition, slip also occurs along West-dipping faults near the shore of the Afrera lake during 2014-2019. This is also indicated by the field observations of dominant West-dipping faults along the Eastern shore of the Afrera lake (Bonatti et al., 2017). Overall, this indicates that extension at AP is mainly accommodated through dominant East-dipping faulting while active West-dipping faults characterize the Eastern-most sector, where the AP connect to the Tat'Ali segment.

The various faults in Afrera also exhibit varying types of behavior. Both the time-series and the individual interferograms show that episodic fault slip events characterize the central fault system of the AP, suggesting that these fault segments have a dominant stick-slip behavior. Here, various fault segments accommodated deformation at different times with similar type, size and timescales of seismic sequences that included the three largest earthquakes of $M_L > 5.0$. The most recent seismic sequence of January 2018 includes two $M_L > 5.0$ along with several $M_L > 4.5$ earthquakes. The best-fit InSAR model shows that fault slip occurs along a shallow oblique fault striking in a ~NS direction and dipping to the East (Figure 4.8). The two largest earthquakes perfectly correspond to the area with the highest deformation observed with InSAR. The second shallower (2.6 km) M_L ~5 of 11 January likely contributed to the observed surface deformation.

Faults close to the tips of the linkage zone instead display both time-progressive and episodic deformation. The time-progressive deformation shown by the time-series at pixel 2 and 3 suggest that these faults creep continuously. Similar patterns in the InSAR time-series have been in fact observed at the San Andreas fault where some segments are creeping (e.g. Shirzaei & Bürgmann, 2013; Jolivet et al., 2014; Khoshmanesh et al., 2015). Additionally, seismic records from Belachew et al. (2011) and Illsley-Kemp et al. (2018) along with relocated seismicity in Chapter 3 show low magnitude earthquakes occurring in these areas during 2005-2009 and 2011-2013 (Figure 4.1 and 4.4). It is thus possible that the fault creep is not aseismic, but instead associated with micro-seismicity. Conversely, a West-dipping fault at the Eastern tip of the AP showed both time-progressive and episodic deformation during 2014-2019 (Figure 4.5 and 4.7) indicating that some faults could alternate their behavior between creep and stick-slip.

It is well known that several fault behaviors can co-exist along different portion of the same fault system or alternate in time along the same fault segment (Harris, 2017). One of the best examples is the San Andreas fault where these phenomena have been well documented (e.g. De Michele et al., 2011; Sammis et al., 2016; Harris, 2017; Rousset et al., 2019). The fault behavior can be influenced by a wide range of factors encompassing, temperature, presence of fluids, fault lithology or a combination of these (e.g. Byerlee & Brace, 1968, 1970; Byerlee, 1993; Vidale & Shearer, 2006; Aochi et al., 2014; Harris, 2017). It has been shown that high temperatures in the deeper portions (> 15 km) of a fault zone may change its rheological properties favoring fault creep (e.g. Brace & Byerlee, 1970; Harris, 2017). Similarly, shallower hydrothermal circulations resulting from the interplay between fluids and positive thermal anomalies alter the fault rocks and generates phyllosilicates that weaken the fault zone in the upper crust and reduce its shear strength, favoring fault creep (e.g. Wintsch et al., 1995; Moore & Rymer, 2007). Conversely, an increase in the pressure of fluids circulating within the fault zone may induce significant fault slip on pre-stressed faults and therefore cause seismicity (Byerlee, 1993; Becken et al., 2011; Vidale & Shearer, 2006; Aochi et al., 2014; Harris, 2017; Ross et al., 2020). While I have few constraints on heat and fluid flows in the region, I primarily observe stick-slip fault behavior in the central portions of the AP, which is away from the magmatic segments and hot springs (Bonatti et al., 2017; Brinckmann et al., 1970). In contrast, I observe either creep or a combination of creep and stick-slip towards the Western and Eastern edges of the AP respectively, both in the vicinity of the magmatic segments, with hot springs common along the Eastern fault. The spatial variability of fault behavior strongly suggests that elevated heat and fluid flow facilitate fault creep. Overall, the AP transfer zone links two en-echelon magmatic segments by oblique slip on multiple en-echelon faults. These faults deform in a more stick-slip fashion in the center of the transfer zone, but with some continuous creep-like behavior closer to the magmatic segments.

4.6 Conclusion

In this chapter, I provided one of the few direct observations on how deformation is distributed across a linkage zone between two active magmatic segments in a natural case. I showed that deformation at the AP, between the Erta Ale and Tat'Ali segments, is accommodated by several en-echelon, ~NS-striking, oblique faults, which are arranged in two main structural architectures: dominant East-dipping faults characterize the center of the

AP while dominant West-dipping faults are observed close to the Eastern tip, where the AP meets the Tat'Ali segment. Various fault segments are active at different time-periods, showing great variability in their behavior. The faults segments at the center of the AP show a dominant stick-slip behavior characterized by episodic slip events associated with $M_L \geq 5$ earthquakes and related seismic sequences. Conversely, heterogeneous fault behavior encompassing creep, micro-seismicity and minor episodic events characterizes the Eastern tip. Here, a strong hydrothermal activity with hot springs and pools have been observed by Brinckmann et al. (1970) and Bonatti et al. (2017).

My observations expand on the results provided in Chapter 3 showing the time-evolving behavior of fault segments at the AP. These new results support the kinematic model of rift-linkage that I proposed for the AP where a right-lateral transfer zone is accommodating deformation between the Erta Ale and Tat'Ali segments. By comparing my results with previous geological studies (Brinckmann et al., 1970; Bonatti et al., 2017), I also hypothesize that heat flow and hydrothermal activity could influence the faults behavior at AP favoring fault creep, punctuated by minor episodic slip events, close to the magmatic segments.

5. Fault kinematics of the North-Western Afar Margin (NWAM) from seismic analyses and InSAR.

In this chapter I investigated the tectonics and kinematics of the Northern sector of the Western Afar Margin (here referred to as North-Western Afar Margin, NWAM), East of the city of Mekele (at latitudes of N13°-N14°), by analyzing the past and recent seismicity that occurred in this region. Both global and local seismic catalogs have been initially inspected to understand the spatial and temporal distribution of seismic activity in the area. Such recordings show persistent low magnitude seismicity accompanying several $M_w > 5$ sequences along systems of marginal grabens (Figure 5.1). Shallow seismicity (< 20 km) commonly occurs but mid-to-lower crustal earthquakes (15-35 km) have also been documented (Figure 5.1, Ayele et al., 2007; Illsley-Kemp et al., 2018a).

Recently, a M_w 5.6 (Ayele et al., 2007) and a M_w 5.2 earthquake struck the NWAM on the 10th August 2002 and the 24th March 2018 (Figure 5.1a). Here, I focused on the event of 2018 and analyzed the related seismic sequence by using continuous recordings from a local seismic survey in Afar during 2017-2018 (Keir et al., 2020), to highlight the active fault systems along the NWAM. I also formed co-seismic interferograms for both the main shocks of 2002 and 2018 using ERS and Sentinel-1 acquisitions but I found no evidence of surface deformation. For the 2002 event the NWAM remains incoherent, while for the episode of 2018 coherence was kept in the interferograms but no significant surface deformation was observed likely due to the large hypocentral depth of the earthquake. Earthquakes during the seismic sequence of 2018 have been in fact located at mid-to-lower crustal depths (15-30 km). Focal mechanisms have also been produced to understand the fault kinematics. These observations have been also interpreted in the light of previous geological and geophysical studies to find plausible explanations on the origins of mid-to-lower crustal seismicity at the NWAM.

5.1 The Wester Afar Margin (WAM)

The Afar depression is bounded to the West by systems of ~NS-trending normal faults extending for ~500 km from latitude N9.5° to N15° along the rift margin. Steep synthetic East-dipping fault scarps with ~1000 m-high trough mark the strongest decrease in elevation from the plateau to the rift floor (Beyene & Abdelsalam, 2005; Sembroni et al., 2017). However, antithetic West-dipping normal faults dominate the architecture of several sector of the WAM producing eastward tilted blocks and a series of en-echelon marginal grabens (Baker et al., 1972; Beyene & Abdelsalam, 2005; Stab et al., 2016; Zwaan et al., 2020a, 2020b). The tilted blocks are evident south of N12.5° showing a dip angle increasing rift-ward from 10° to 45° and are controlled by West-dipping faults with dip angles up to 70° (Zwaan et al., 2020a, 2020b). The marginal grabens extend for tens of kilometers in NNW-SSE direction, oblique with respect to the general NS trend of the WAM, and are connected by complex transfer zones which result in a right-stepping geometry (Zwaan et al., 2020a, 2020b). Dense drainage networks crosscut the WAM from West to East eroding the faulted blocks and depositing sediments within the adjacent basins.

In the NWAM, East of the Mekele city, between N12.5° and N14.0°, a 2000 m-elevated region hosting a Mesozoic marine sequence outcrops overlaying the Precambrian metamorphic basement made of a low-grade volcano-sedimentary rocks associated with mafic-ultramafic complexes. In the area, the interplay between tectonic and erosion caused the younger Mesozoic rocks to outcrop surrounded by the older basement (Sembroni et al., 2017). The entire sequence is intruded by doleritic dykes and sills which are 33-26 Ma in age (Sembroni et al., 2017; Zwaan et al., 2020a). To the South, the sequence is bounded by volcanic rocks pertaining to the trap series (Abdelsalam et al., 2002; Sembroni et al., 2017). Systems of East-dipping and West-dipping normal faults form a series of marginal grabens. Some of them are reported in the literature with the local names of the closest sites, such as Berahale, Abala (Zwaan et al., 2020a) and Dergaha grabens (Gouin, 1979) (Figure 5.1b). The marginal grabens have the same NNE-SSW trend observed elsewhere along the WAM. However, unlike other sectors of the WAM where marginal grabens are well developed, with sharp margins and clear fault surfaces, smaller and less developed basins have been observed between N13° and N14.0° (e.g. Dergaha) (Zwaan et al. 2020a, 2020b). The complex and strongly eroded fault systems in this sector also prevent a complete understanding of its structural setting (Zwaan et al., 2020b). Structural field measurements exist for the Abala

graben and report an extension direction of ~N80°E (Zwaan et al., 2020b) while for other adjacent grabens there are no measurements. Finally, some hydrothermal activity with hot springs is also reported 20 km South of Dergaha (Keir et al., 2009) (Figure 5.1b).

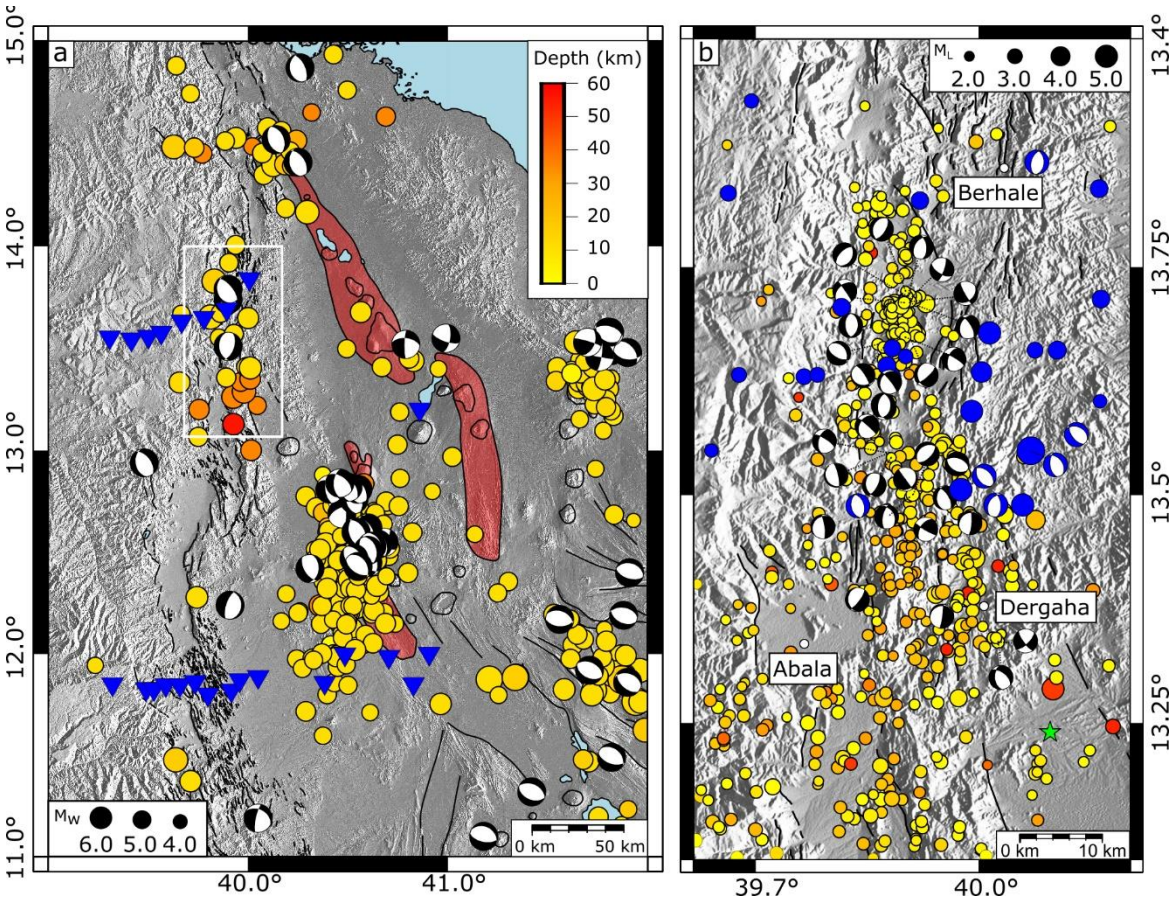

Figure 5.1 – a) Seismicity in Afar between 1973-2019 (circles color-coded by depth) from NEIC and focal mechanisms (beach balls) from the gCMT catalog. The blue triangles are the seismic stations of the temporary network 2017-2018 used in this study. Black solid lines are faults from Zwaan et al. (2020b). The white box marks the area shown in b) Seismicity (circles color-coded by depth - same scale as in panel a) recorded by local temporary networks between 2005-2013 (Ayele et al., 2007; Zwaan et al., 2020c). The solid blue circles are the seismicity in August 2002 from Ayele et al. (2002) (the depth information is not available). Black focal mechanisms are from 2011-2013 (Illsley-Kemp et al., 2018a; Zwaan et al., 2020c) while the blue ones are from 2002 (Ayele et al., 2007). The green star is a hot spring (Keir et al., 2009).

5.2 Seismicity at North-Western Afar Margin (NWAM)

Figure 5.1 shows the seismicity recorded by both global and local networks in the study area. Seismic activity in the NWAM is characterized by several $M_w > 5.0$ earthquakes that have occurred during the last few decades. The first seismic sequence instrumentally recorded in the area is that of April 1989 (USGS NEIC seismic catalogue). The episode included two earthquakes with $M_w > 5.0$ and several $M_w > 4.0$ at the Southern tip of the

Dergaha and Abala grabens, between N13.2° and N13.4° (Figure 5.1a). Relatively deep hypocenters, between 10 km to 33 km, are reported in global catalogs for these episodes (Figure 5.1a). Further to the North, between N13.5° and N13.8°, a sequence of 75 earthquakes accompanied a main shock with M_w 5.6 in August 2002 (Ayele et al. 2007). Moment tensor inversion of locally recorded waveforms provided focal solutions mechanisms for six of these events consistent with normal faulting along NNW-striking, NE-dipping planes (Figure 5.1b, Ayele et al., 2007). Depths estimated with the same technique give shallow depths between 5-7 km (Ayele et al., 2007).

More recently, the temporary seismic networks active between 2005-2009 (Belachew et al., 2011; Ebinger et al., 2008) and 2011-2013 (Illsley-Kemp et al., 2018; Zwaan et al., 2020b) recorded more than 1900 low-magnitude earthquakes North of the Dergaha graben (Figure 5.1b) suggesting that seismicity along the NWAM is common. Furthermore, high-frequencies of the earthquake waveforms indicate that such seismicity is tectonic (Illsley-Kemp et al., 2018a). The hypocentral distribution during 2011-2013 highlighted West-dipping faults with seismicity mainly clustered at depth < 5 km but with some also deeper than 20 km, close to Abala (Illsley-Kemp et al., 2018a; Zwaan et al., 2020b). The focal solutions show both normal and oblique-slip faulting (Figure 5.1b) accommodating extension directed at N82°E, suggesting that extension along the NWAM is currently accommodated by mainly West-dipping faults (Illsley-Kemp et al., 2018a; Zwaan et al., 2020b). A Similar structural architecture has been also observed in other sectors of the WAM, South of N12° (e.g. Stab et al., 2016). However, the causes of deep seismicity close Abala has not been investigated in detail. Furthermore, a peculiar bending in the distribution of the seismicity is observed South of Abala (Figure 5.1) where a complex right-stepping transfer zone connects the marginal grabens (Zwaan et al. 2020b). How Abala connects to the Southern grabens is not fully understood.

5.3 Earthquake location and magnitude estimation

Twenty-four stations from the two recent temporary seismic networks (Keir et al. 2020) were operational during the 24 March 2018 when the M_w 5.2 earthquake struck the NWAM, East of Mekele. I inspected 41 days of continuous seismic recordings, from the 20 March to the 30 April in order to identify all the earthquakes that occurred in Afar during that period and found that a total of 930 events have been measured by the continuous data. I manually picked both P and S waves for earthquakes recorded by four or more stations and located the

events using the Oct-Tree search algorithm implemented into the NLLoc software (Lomax, 2000). For the location, I used the same 2.5D velocity model, used in the previous chapter, based on the receiver function study of Hammond et al. (2011) and seismic refraction data from Makris & Ginzburg (1987) (Figure 2.12). The local magnitude (M_L) for each earthquake has been calculated by measuring the zero-to-peak amplitude on simulated Wood Anderson seismometers, and using the distance correction for the Danakil region from Illsley-Kemp et al. (2017).

I located 673 events on the NWAM (Figure 5.2a) with average vertical and horizontal errors of ±4.8 km and ±6.6 km, respectively. The seismic catalog has events with $M_L \geq 1.6$ and average uncertainty in magnitude estimation of ±0.3 (Figure 5.2b and c). The local magnitude of the main shock has been calculated to be M_L 5.3 ± 0.4, in agreement with the M_w 5.2 reported by the NEIC. Hypocentral depths and related uncertainties are shown in Figure 5.3, where I reported only earthquakes with both horizontal and vertical errors lower than 6 km. Earthquakes in Figure 5.3 are color-coded by date, as in Figure 5.2. I identified two areas of clustered seismicity characterized by different spatial and temporal distributions (Figure 5.2 and 5.3). The main seismic sequence of March-April 2018 occurred within the Dergaha graben with 514 earthquakes located along a system of ~NS-striking faults bounding the graben to the West (green box in Figure 5.2a). Hypocentral depths range between ~1 km and ~35 km indicating that seismicity in this sector of NWAM is deep and occurs throughout the entire crust (Figure 5.3). The main-shock occurred at a depth of ~19 ± 4 km, also where most of the seismicity is focused (Figure 5.3). The temporal distribution of earthquakes in Dergaha is characterized by continuous seismicity during the investigated time period, with an average of ~14 earthquakes per day but with two bursts of activity during the 24 March 2018 (day of the main event) with more than 50 earthquakes, and 16 April 2018 with 30 earthquakes (Figure 5.2d and e). Seismicity progressively decays to ~3 earthquakes per day by the 29 April 2018, comparable to the number of earthquakes occurred the days before the onset the seismic sequence (Figure 5.2d and e). Interestingly, a pattern in the statio-temporal distribution of earthquakes can be inferred from the profiles in Figure 5.3. The main sequence takes place close to the Southern tip of Dergaha at depth of 19-25 km, where the main-shock occurred. After that, earthquakes show a progression to shallower crustal levels and toward the Northern tip of Dergaha which could indicate a migration of seismicity.

Minor seismic activity has also been observed within a small graben, South-West of Berahale (blue box in Figure 5.2a and Figure 5.3b). Seismicity is shallower, between 5 km and 15 km with 75 earthquakes that were scattered in time rather than clustered in seismic sequences, as observed in the Dergaha graben. Furthermore, the occurrence of the earthquakes in this sector seems to be temporally independent from the main seismic sequence (Figure 5.2d-e).

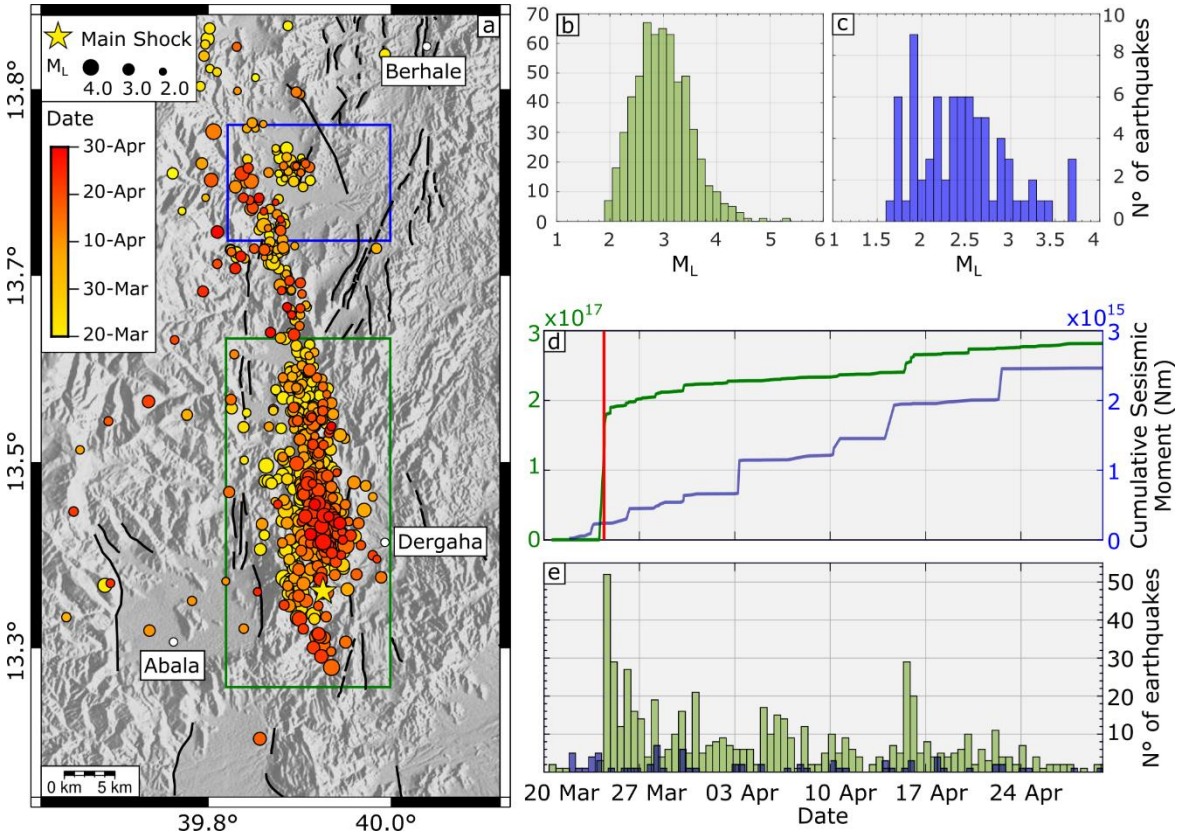

Figure 5.2 – a) Epicentral distribution of the 673 earthquakes located with NLLoc (Lomax, 2000) and occurred between 20 March 2018 and 29 April 2018. The earthquakes are colored-coded by time. The blue and green boxes highlight two different marginal grabens along the NWAM. b) and c) Histograms of magnitudes for the two areas highlighted in a). d) and e) cumulative seismic moment curves and histograms of number of earthquakes for the two areas in a).

To improve the resolution of hypocenter locations and highlight active fault planes, I relocated 262 earthquakes using the Double-Difference method implemented in the HypoDD software. The relocated seismicity seems to highlight both East and West-dipping active fault planes bounding the Western side of the Dergaha graben (Figure 5.4a and b). Sharp alignments of seismicity that I interpret as illuminating the fault planes are clear at a depth between 15-30 km (Figure 5.4b). In addition, the projection of these planes to the surface clearly matches the topographic expression of faults represented by a series of scarps

separating the Dergaha graben from the adjacent horst (Figure 5.4b). The distribution of seismicity also shows a main fault plane dipping to the West while a conjugate East-dipping fault is just observed at the Northern tip of the Dergaha graben.

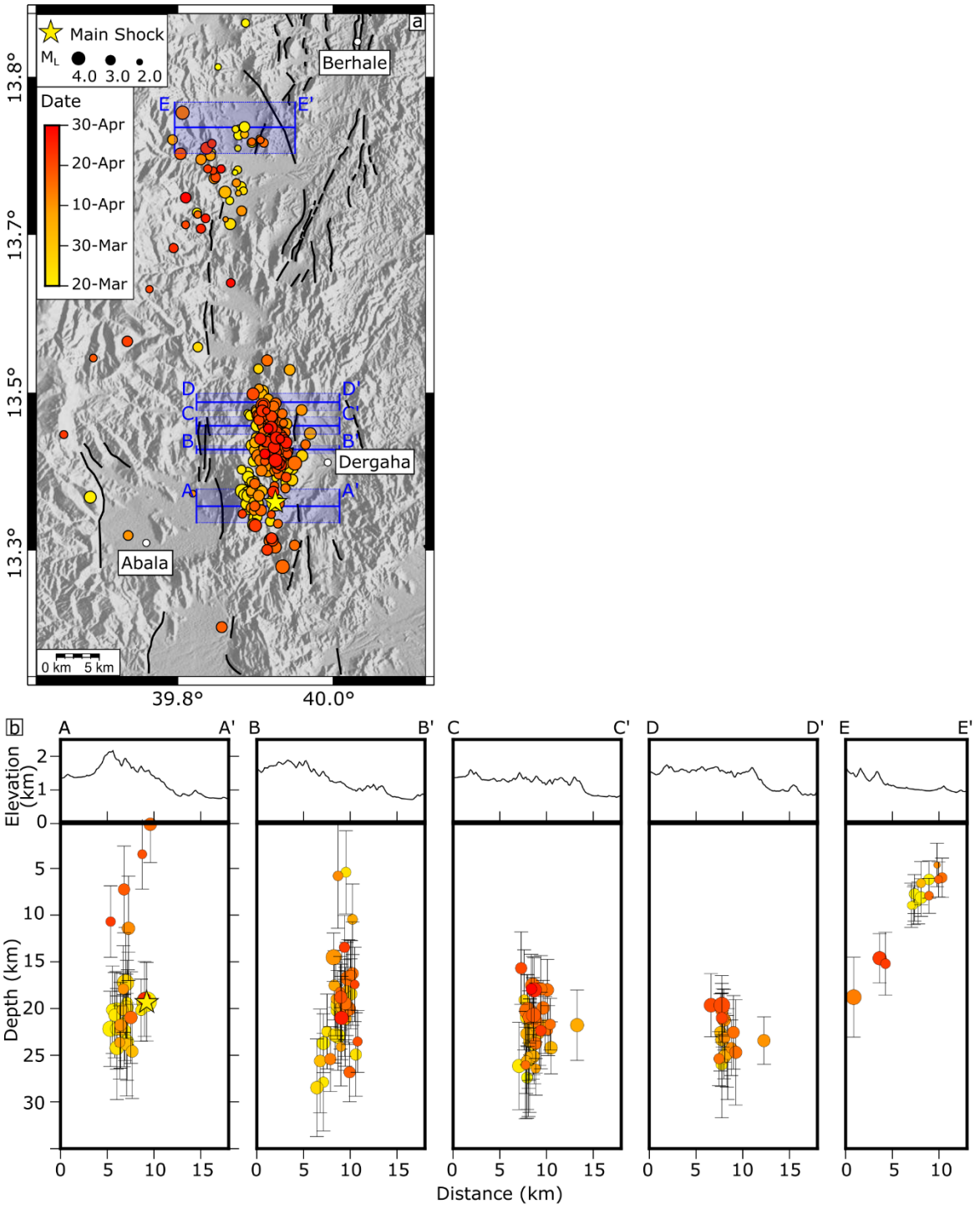

Figure 5.3 - Filtered seismic catalog including just earthquakes with both vertical and horizontal errors lower that 6 km. **a)** Earthquakes distribution in map view. **b)** Seismicity profiles projecting earthquakes within a line section onto the profiles. The projection width is represented by the blue shadowed areas in a).

5.4 Focal mechanisms

I computed focal mechanisms based on the polarities of the P-wave arrivals at both Northern and Southern stations. P-wave arrivals of events recorded by more than 15 stations have been processed using FOCMEC software (Snoke, 2003). Focal solutions have been attempted only for earthquakes with unambiguous first arrivals and no polarity errors have been allowed. This resulted in well solved focal mechanisms with maximum standard deviations (σ) in strike and dip angles equal to 7.5° and 11°, respectively (Table C1). I considered the nodal planes subparallel to the faults reported in literature (i.e. ~NS) as the main ones and classified their kinematics on the basis of the rake value. P and T axes of each solution have been used to retrieve the average extensional direction along the NWAM.

Twenty well-constrained focal mechanisms have been obtained for earthquakes within the Dergaha graben. All the solutions have main nodal planes oriented ~NS (Table C1 and Figure 5.4c). The focal solutions are characterized by dominant normal faulting along ~NS-striking faults, associated with a minor lateral component (Figure 5.4a and b). Ten focal mechanisms related to the major events can be observed along the central and Southern part of the Dergaha graben and show normal faulting with minor right-lateral slip on steep (57°-84°), West-dipping planes (Figure 5.4a and c, Table C1). Conversely, normal faulting earthquakes with minor left-lateral slip along East-dipping planes mainly focus along the Northern tip of the Dergaha graben (Figure 5.4a and c, Table C1). Three pure dip-slip focal mechanisms are also present in the central portion of the graben, with both East- and West-dipping planes (Figure 5.4a and c, Table C1). P and T axis computed from all the solutions indicate an average extension directed N92°E, nearly orthogonal to the average faults' strike in this sector of the NWAM. The main nodal planes match very well the structures observed in the field by Zwaan et al. (2020b) as also the fault planes highlighted by the relocated seismicity (Figure 5.4).

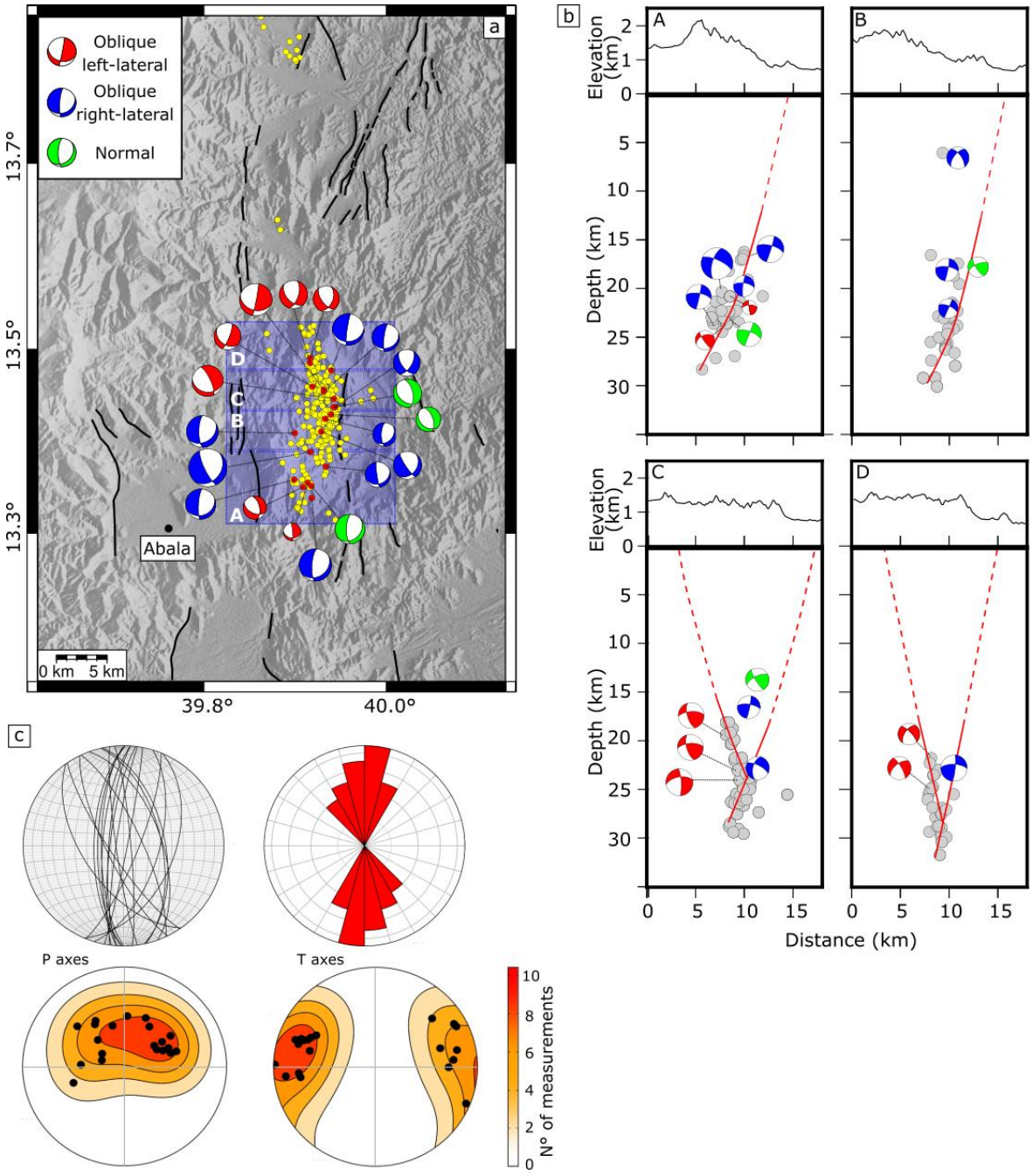

Figure 5.4 - Focal mechanism solutions in map view a) and cross sections b) for events located with more than 15 stations. Yellow dots in a) and gray dots in b) are the relocated seismicity. Red lines in b) represents possible faults highlighted by the relocated seismicity. c) Stereographic plots show the strike and dip (top left), the rose diagram of faults strikes (top right), and the P and T axes of the main nodal planes with density based on the number of measurements (bottom).

5.5 Interferometric Synthetic Aperture Radar (InSAR)

InSAR is widely used to identify co-seismic surface deformation and investigate the earthquake source parameters. However, the possibility to detect co-seismic surface deformation by InSAR strongly depends on the noise level affecting the interferometric phase (e.g. spatial and temporal decorrelations or atmospheric noise) along with the earthquake magnitude and the depth at which faulting occurs (e.g. Dawson & Tregoning, 2007; Funning & Garcia, 2019).

The M_w 5.6 of August 2002 was located in the upper crust by Ayele et al. (2007) and was covered by the ERS-2 ascending track 321. I successfully formed at least one co-seismic interferogram spanning about 5 years from track 321 (Figure 5.5) but the high perpendicular baselines of the ERS acquisitions prevented forming other shorter spanning interferograms. As can be seen in Figure 5.5, the co-seismic interferogram has overall low coherence along the border faults and the epicenter of the M_w 5.6 corresponds to an area of complete incoherence.

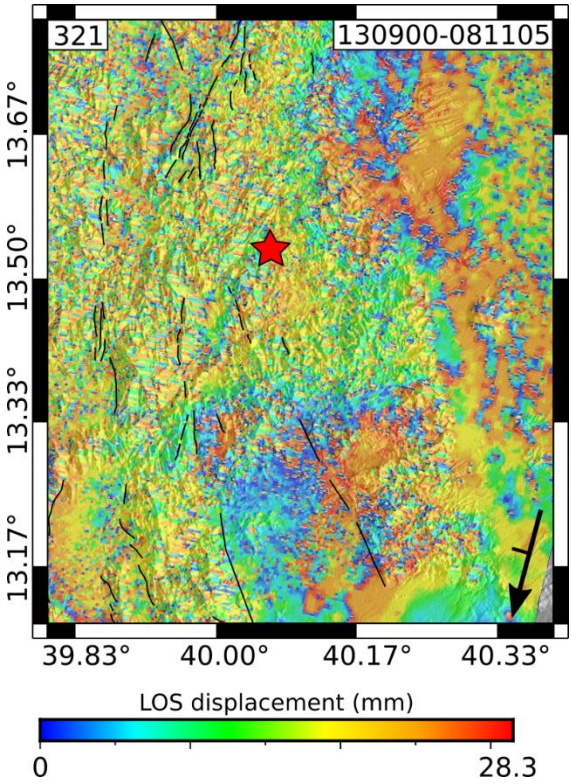

Figure 5.5– Descending ERS-2 interferogram covering the M_w 5.6 of August 2002. The epicentral location of the M_W 5.6 in August 2002 is marked by the red star and it occurred in an area of incoherence. The dates of ERS acquisitions used to form the interferogram are given in the top right corner as ddmmyy. Black solid lines are faults (Zwaan et al., 2020b).

In order to investigate the surface deformation related to the M_L 5.3 event of 24 March 2018, I also formed a series of Sentinel-1 interferograms from both ascending and descending tracks (Figure 5.6a, b and C1). Six independent interferograms with progressively increasing temporal baselines have been processed using the InSAR Scientific Computing Environment (ISCE) software developed by the Jet Propulsion Laboratory, Caltech and Stanford University (Rosen et al., 2012) and the same conventional processing parameters as in Chapter 4. The Sentinel-1 interferograms have relatively low level of noise and maintain good coherence up to temporal baseline of 6 months. However, no significant deformation has been identified in any of the co-seismic interferograms in the epicentral area (Figure 5.6a, b and C1) suggesting that co-seismic slip occurred at large depth and caused too small surface deformation to be measured by InSAR, as also indicated by the seismic data. To test this hypothesis, I produced a series of simulated interferograms assuming different depth of possible fault slip. I used an Okada shear dislocation within a homogeneous, elastic half-space with a Poisson's ratio of 0.25 and a shear modulus (μ) of 3.2×10^{10} Pa (Okada, 1985). On the basis of the seismic observations, I assumed a 10 km-long normal fault, striking North-South and dipping to the West with an angle of 70°. Normal slip has been fixed at 24.5 cm corresponding to a M_w 5.2, as reported by the USGS NEIC catalogue. I produced forward models of the InSAR deformation assuming progressively increasing depths of the upper fault edge, between 1 km and 15 km with a step size of 5 km (Figure 5.6c, d, e, f). The simulations show that LOS decreases rapidly at increasing depth of faulting with values of LOS down to 8 mm for an upper fault edge at a depth 15 km. Therefore, I conclude that at depth of ~19 km as estimated by seismicity the LOS deformation would be too small to be detected by InSAR.

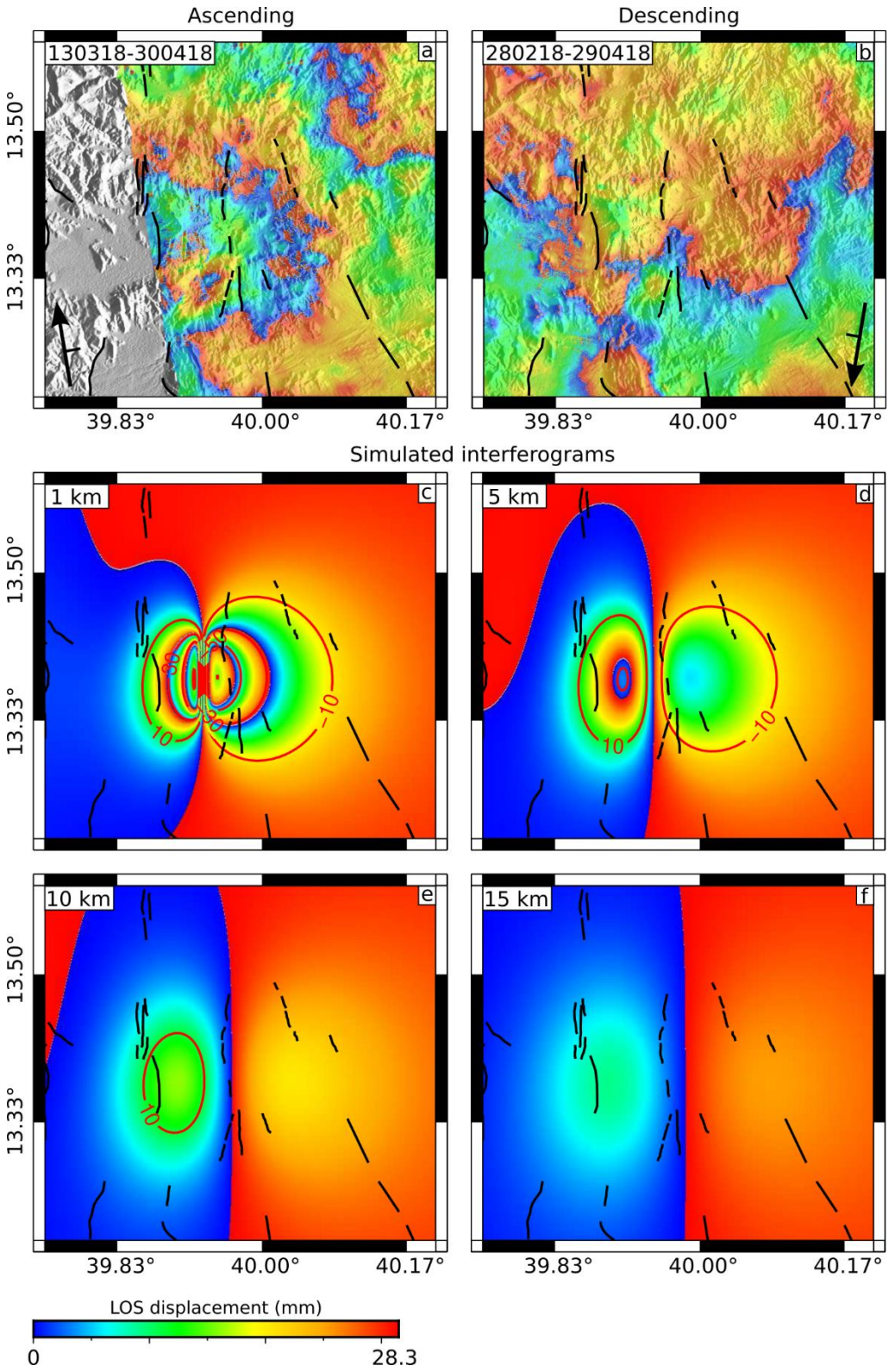

Figure 5.6 - a), b) Measured wrapped co-seismic interferograms from Sentinel-1 acquisitions. c), d), e), f) Simulated wrapped interferograms assuming Okada shear dislocation model located at increasing depth. The red contour lines display the deformation in mm. Black solid lines are faults reported by Zwaan et al. 2020b.

5.6 Discussion

I analyzed the seismicity in a time period of 41 days, covering the M_L 5.3 of March 2018, to investigate the fault activity across the NWAM, East of the Mekele city. Seismic location and well-constrained focal mechanisms provided a picture of the fault kinematics characterizing the marginal grabens during the analyzed time period.

I observed earthquakes focused in a sector of the NWAM (N13.3°-N13.8°) characterized by continuous seismicity and several $M_w > 5$ in the past few decades (NEIC, Ayele et al., 2007; Belachew et al., 2011; Illsley-Kemp et al., 2018a) (Figure 5.1 and 5.2). The largest part of the catalog consists of the seismicity that occurred at Dergaha and within the minor basins to the North between the 24 March 2018 and 29 April 2018. The results show the main seismic sequence was distributed through the entire crust, with the main M_L 5.3 occurring at ~19 km and the other major earthquakes also located in the lower crust between 15 and 30 km (Figure 5.3 and 5.4b). InSAR data also do not show any significant surface deformation related to the main shock suggesting that the hypocentral depth of the episode was greater than 15 km (Figure 5.6), in agreement with the seismic results. Mid-to-low crustal depths have been also reported in global catalogues for other $M_w > 5$ earthquakes in 1989-1990, as also in local catalogs (Zwaan et al. 2020c), suggesting that part of the seismic moment in this sector of the NWAM is released at an anomalous depth. Conversely, the M_w 5.6 sequence of August 2002 close to Dergaha was shallower (5-15 km), as also the low magnitude seismicity North of ~N°13.6 reported by Illsley-Kemp et al (2018a) and Zwaan et al. (2020c) during the time period 2011-2013.

The relocated seismicity in Dergaha highlights two steep crustal faults with a main West-dipping fault and a conjugate East-dipping fault (Figure 5.4b). The latter seems to rupture just at the Northern tip of the Dergaha graben. The imaged fault planes from the alignment of the seismic cluster have a good correspondence with the orientation of nodal planes in the focal solutions. Jointly, the earthquake locations and focal mechanisms indicate dominant normal faulting characterized by a minor right-lateral slip along West-dipping faults at the Southern and central portion of Dergaha. To the North, the dominant normal component is instead associated to minor left-lateral slip along East-dipping faults. Furthermore, the geometry of two fault planes at Dergaha suggest that West-dipping faulting is dominant. The T axes calculated from the focal solutions indicate that the average extension direction is oriented ~EW. Structural field measurements in Abala, along with

seismicity and focal mechanisms south of Berhale indicate similar extension directions and fault architecture (Zwaan et al., 2020b). Few shallow earthquakes along East and West-dipping faults are also reported in Dergaha by Zwaan et al. (2020b).

On the basis of the diffuse seismicity and the structural evidences of active faulting at surface, Zwaan et al. (2020b) suggested that tectonic extension is still occurring along the NWAM. The correspondence between my observations of oblique faulting and their structural and seismic dataset supports this hypothesis. However, I also show that deep seismicity occurs in the area and that dissimilarities between the temporal and spatial distribution of seismicity in Dergaha and in the other sectors of the NWAM exist. In particular, seismicity south of Berhale is spread over time and seems to occur independently from the main seismic sequence in Dergaha. Furthermore, the observation of deep earthquakes focused below Dergaha suggest that the mechanism driving seismicity here may be different to that causing seismicity along the rest of the NWAM, where only upper crustal earthquakes are observed (e.g. Ayele et al. 2007; Zwaan et al., 2020b).

Deep earthquakes have been widely observed elsewhere at both mature and young basins along the East African Rift System (e.g. Main Ethiopian Rift, Keir et al., 2009; Western Rift, Albaric et al., 2009, 2014; Tanganyika Rift, Shudofsky, 1985; Lavayssière et al., 2019) as well as other active rifts worldwide (e.g. Doser & Yarwood, 1994; Déverchère et al., 2001). Deep (15-30 km) moderate earthquakes ($M_W < 6.0$) occur across hundreds of kilometers-long segments of the Western and Eastern Rift Systems in Tanzania. Several authors (e.g. Shudofsky, 1985; Albaric et al., 2009, 2014) related such seismicity to the presence of a strong, intruded, mafic lower crust which can deform in a brittle manner at high depths. The same mechanism has been also invoked by Déverchère et al. (2001) to explain deep seismicity in the Baikal rift. Similarly, Lavayssière et al. (2019) analyzed seismicity in the Rukwa and Tanganyika rifts during 2014-2015 to suggest that deep earthquakes are related to the activity of steep border faults cross-cutting the entire crust, which is enabled by a cold lower crust and a very thick mantle lithosphere in the region. In contrast, Seno and Saito (1994) explained deep earthquakes across the East African Rift System as induced by the locally high strain rates induced by migration of fluids, such as from the upper mantle. Similarly, Lee et al. (2016) compared flux measurements and isotope compositions of CO_2 emissions with lower crustal earthquakes along large-offset fault scarps in the Magadi-Natron Basin (Kenya-Tanzania border) to suggest that deep seismicity (15-27

km) in the area is caused by tectonic degassing of mantle-derived CO_2. Deep seismicity has been also reported by Keir et al. (2009) near the flank of the Main Ethiopian Rift, where spatial associations between lower crustal earthquakes and high conductivities imaged in magneto-telluric data led them to the hypothesize that such seismicity is related to either melt migration, or fluids release resultant from magma emplacement.

The presence of NS-oriented mafic dikes along the NWAM such observed between Berahale and Abala (Zwaan et al., 2020b) indicates that mafic intrusions has been emplaced below the NWAM. The Miocene age of the majority dykes is similar to that observed along the margin of the Red Sea and likely associated with early magma-assisted rifting (e.g. Buck, 2006). A possible explanation for deep seismicity in the study area could thus be that the lower crust beneath the NWAM is mafic and therefore anomalously strong. However, such factor would likely cause deep seismicity on a large scale, as occur in Tanzania or along the Baikal rift where the spatial extent of deep earthquakes is observed for hundreds of kilometers along the rift (Déverchère et al., 2001; Albaric et al., 2009). By comparing my results with other local and global seismic catalogs (e.g. Figure 5.1), I observe that the area showing deep seismic in the NWAM is strongly focused around the Dergaha graben only. This brings me to hypothesize that a more local factor could play a role in triggering the deep earthquakes. Seismic imaging of the crust by Hammond et at (2011) have shown an anomalously high Vp/Vs ratio (~ 2.1) beneath Dergaha which has been interpreted as due to the current presence of partial melt in the crust. I thus hypothesize that the deep, focused seismicity in Dergaha could be induced by migration of either melt, or other fluids through the lower crust (Figure 5.7). My interpretation of fluid induced seismicity here is also supported by the migration pattern of earthquakes toward shallow crustal levels and toward the Northern tip of Dergaha (Figure 5.4), as also by the swarm like nature of the seismicity preceding the main sequence (Belachew et al., 2011; Zwaan et al., 2020b). In addition, hot springs are present near the Dergaha graben, but absent further North where the earthquakes are only in the upper crust (Figure 5.1). Patterns of earthquakes migration have been widely observed during either seismic sequences or swarms, and in some case, they have been interpreted as induced by fluids (e.g. Antonioli et al., 2005; Yamada et al., 2015; Yoshida & Hasegawa 2018). Fluid induced fault slip could assist tectonic extension by reducing the yield strength of the surrounding crust triggering slip and seismicity along crustal faults as observed in the Main Ethiopian Rift and in Magadi-Natron Basin (Keir et al., 2009; Lee et

al., 2016). Deep seismicity in the Magadi-Natron Basin generated by tectonic degassing of mantle-derived CO_2 highlights the deep portion of steep rift-parallel border faults (Lee et al., 2016). Similarly, the spatial and temporal distribution of earthquakes in Dergaha along with their focal mechanisms could indicate that the fluids induce failure of deep fault systems connected to the upper crustal faults, as also suggested by the presence of hydrothermal activity in the area

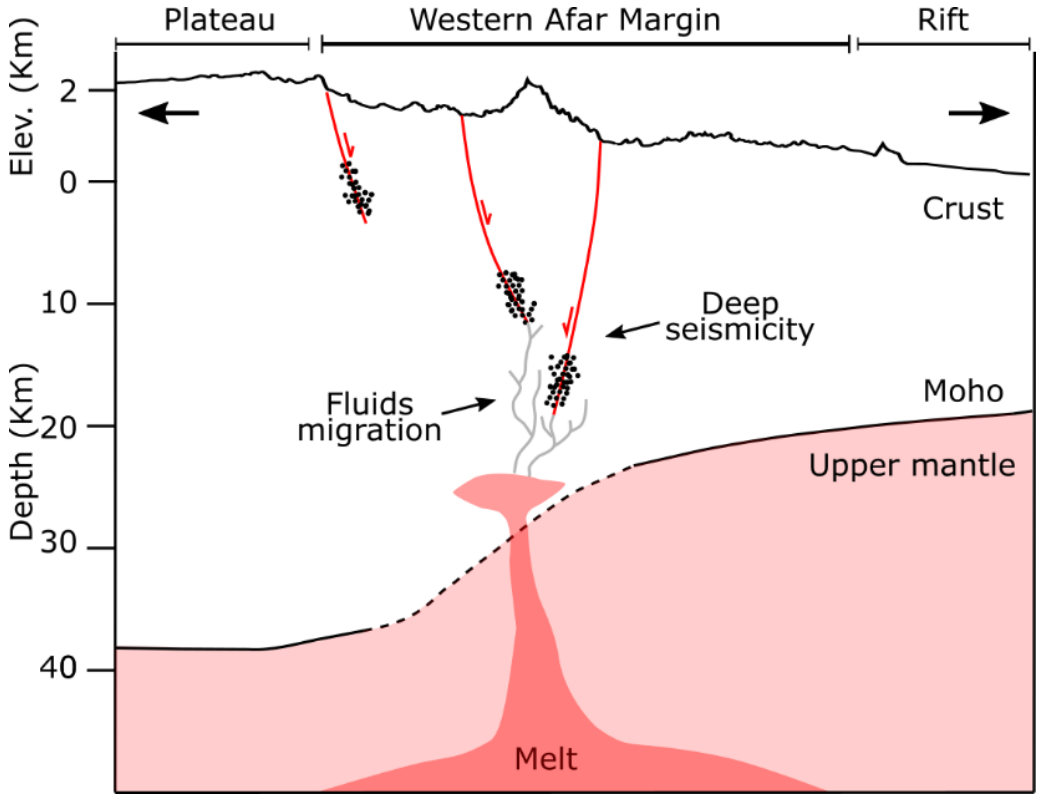

Figure 5.7 – Cartoon depiction showing the hypothesized mechanism controlling deep seismicity below the Dergaha graben.

5.7 Conclusion

In this chapter, I provided new observations of the fault activity across the NWAM. I showed that the seismic sequence of March 2018, East of Mekele, ruptured the deep portion of tens of kilometers-long crustal faults in the Dergaha graben, where other deep seismic sequences occurred in the past. The kinematics of rupture during the sequence showed an extension oriented ~EW, consistent with tectonic regime of the area inferred from other seismic and structural observation in previous studies (Illsley-Kemp et al., 2018a; Zwaan et al., 2020a). Deep seismicity focuses in a crust characterized by high Vp/Vs ratios which could indicate the presence of partial melt or other fluids (Hammond et al., 2011).

My results support the hypothesis that tectonic extension is still ongoing in the NWAM and provide new constrains on the kinematics of previously poorly investigated sectors. However, I also suggest that tectonic extension in the region near the Dergaha graben is accompanied by fluid induced faulting in the lower crust as indicated by the deep seismicity, presence of hot springs, and by independent evidence of partial melt beneath Dergaha (Figure 5.6) (Hammond et at. 2011). Such evidences could thus suggest that fluid migration resultant from magmatic processes plays an important role in influencing the fault activity at the rift margins during incipient break-up in Northern Afar.

6. Summary of results

In this thesis I investigated the tectonic deformation in Northern Afar to understand how strain is partitioned between border faults and axial magmatic segments in a mature stage of continental break-up.

In the Afrera Plain, between Erta Ale and Tat'Ali magmatic segments, rift-linkage processes are ongoing. In Chapter 3 I investigated such processes by combining InSAR, structural and seismic data, which have been jointly interpreted to suggest a new kinematic model of rift-linkage for the Afrera Plain. According to this model, the Erta Ale and Tat'Ali segments are interacting through a complex right-lateral transfer zone with dominant oblique left-lateral slip along ~NS-striking faults. The results shown in Chapter 3 opened new questions about the distribution of deformation across the Afrera Plain linkage-zone and whether faults slip episodically or creep. In Chapter 4 I addressed these questions by performing InSAR time-series analysis, combined with InSAR modelling and seismicity. I showed that multiple NS-striking, en-echelon oblique faults accommodate deformation but are active at different times and show different behaviors encompassing seismic creep and stick-slip. Furthermore, the time-series analysis and the modeling of episodic co-seismic deformation in 2018 shows that two structural architectures exist at the linkage zone: dominant East-dipping faults in central Afrera, and dominant West-dipping faults close to the Tat'Ali segment. In order to find a comprehensive explanation for the different fault behaviors, I combined my results of InSAR time-series with previous geological and geophysical studies. I hypothesize that the presence of magma below the Afrera Plain, and the related circulation of hydrothermal fluids in the crust, could play a role in influencing the fault behavior and seismicity at Afrera. In detail, a dominant stick-slip behavior seems to characterize the main central fault system which is far from the shallow evidences of hydrothermal activity. Conversely, the fault behavior at the Eastern tip of Afrera Plain is more heterogenous with creep, micro-seismicity and episodic slip events. Here hydrothermal activity could have a double effect either by altering the fault rocks and producing minerals which favor creep (e.g. phyllosilicates), or by inducing episodic slip events triggered by fluid overpressures.

Intense and almost continuous seismicity characterizes the Northern sector of the Western Afar Margin, East of the Mekele city. Several M_w> 5 earthquake sequences have been reported in the area, in both local and global catalogs (NEIC; Ayele et al. 2007; Belachew et al., 2011; Illsley-Kemp et al., 2018a). In Chapter 5, I analyzed seismicity covering the M_L 5.3 sequence of March 2018, in the North-Western Afar Margin to show that it was caused by faulting, as also suggested in recent studies by Illsley-Kemp et al. (2018a) and Zwaan et al (2020b). I also documented that the seismicity was deep, as observed in other mature and young sectors of the EARS (e.g. Keir et al., 2009; Lavayssière et al., 2019). The main seismic sequence of March 2018 occurred at depths of 15-30 km below Dergaha, where also other deep earthquakes occurred in the past. I showed that seismicity occurs along major West-dipping fault, yet conjugate East-dipping faults are also active. Finally, I interpreted the deep earthquakes in combination with previous geophysical evidences (Hammond et al. 2011) and suggested that seismicity could be triggered by fluids migration from partial melt in the lower crust.

The results achieved in this thesis provide new contributions towards improving the understanding of the tectonic deformation in extensional plate boundaries during incipient continental break-up. One of the main successes in this thesis is the application of InSAR in combination with seismicity to identify different modes of deformation of faults, showing that InSAR can be used to study even small-scale local deformation. Conversely, relatively small deformation, caused by M_W 5.1, but occurring at depths > 15 km prevented me from using InSAR on the border faults. This thesis also provides new insights on the tectonic activity at mature rift margins suggesting that the presence of magma can promote border fault activity also during the final stage of continental rifting, yet further investigations are required to corroborate the hypotheses. Future research studies could thus address the distribution of melt and fluids at the rift offsets and along the margin in Northern Afar and their role in focusing deformation and influencing fault activity.

Acknowledgements

The last three years have been full of great experiences and my whole PhD has been a period of continuous learning, impulses and professional enrichment which allowed me to grow as a person and as a future researcher. This has been possible thanks to lot of people to whom I'm grateful.

First, I would like to thank my advisor Prof. Carolina Pagli for her supervision. Her feedback and precious advices have been for me a beacon during my entire PhD, and they always will be. She supported me every day and taught me how to do research at best. She is a mentor to me and I will be always immensely grateful for her lessons and for believing in me.

Many thanks also to my co-advisors Prof. Derek Keir and Prof. Federico Sani for the time they dedicated to me and their valuable teachings in Earthquake Seismology and Structural Geology. They, and the interaction with them during these three years, make me understand how a positive and successful research team works, making me feel part of it.

I would like to acknowledge the two external reviewers, Prof. Eleonora Rivalta from the Department of Physics and Astronomy "Augusto Righi" (University of Bologna), and Prof. Freysteinn Sigmundsson from the School of Engineering and Natural Sciences (University of Iceland) for their precious feedback and comments that definitely improved the quality of this thesis.

A big thanks also goes to all the other scientists with whom I worked during my PhD, having inspirational conversations, and that kindly provided ideas and data. Many thanks to Giacomo Corti from the IGG-CNR (Instituto di Geoscienze e Georisorce - Consiglio Nazionale delle Ricerche) of Florence and Prof. Hua Wang from the Department of Surveying Engineering of Guangzhou for their precious ideas and advices. Many thanks to Cecile Doubre and the researchers of the EOST (École et Observatoire des Sciences de la Terre) of Strasbourg for kindly hosting me in their Department. Thanks also to the students and researchers at the Ocean and Earth Science Department of Southampton, where I have the pleasure to work at. I also would like to acknowledge Prof. Atalay Ayele, Birhanu Abera, Daniel Mamo Teshome from the Institute of Geophysics, Space Science and Astronomy of Addis Ababa, Prof. Sylvie Leroy from the ISTeP-Institut des Sciences de la Terre de Paris,

and all the people I met in Ethiopia, for providing data, advices and technical support in the field.

I certainly want to thank my colleagues of Earth Science Department of Pisa for their friendship and these three wonderful years together. Thanks to Simone, Stefano, Fabrizio, Edoardo, Giorgio, Alberto, Gianmaria and Martina.

My final thanks go to Giovanni, Fabio and to my Family that always loves and support me. Last but not least, I’m deeply grateful to Simona, for her unconditioned love and for being by my side every day.

Appendix A

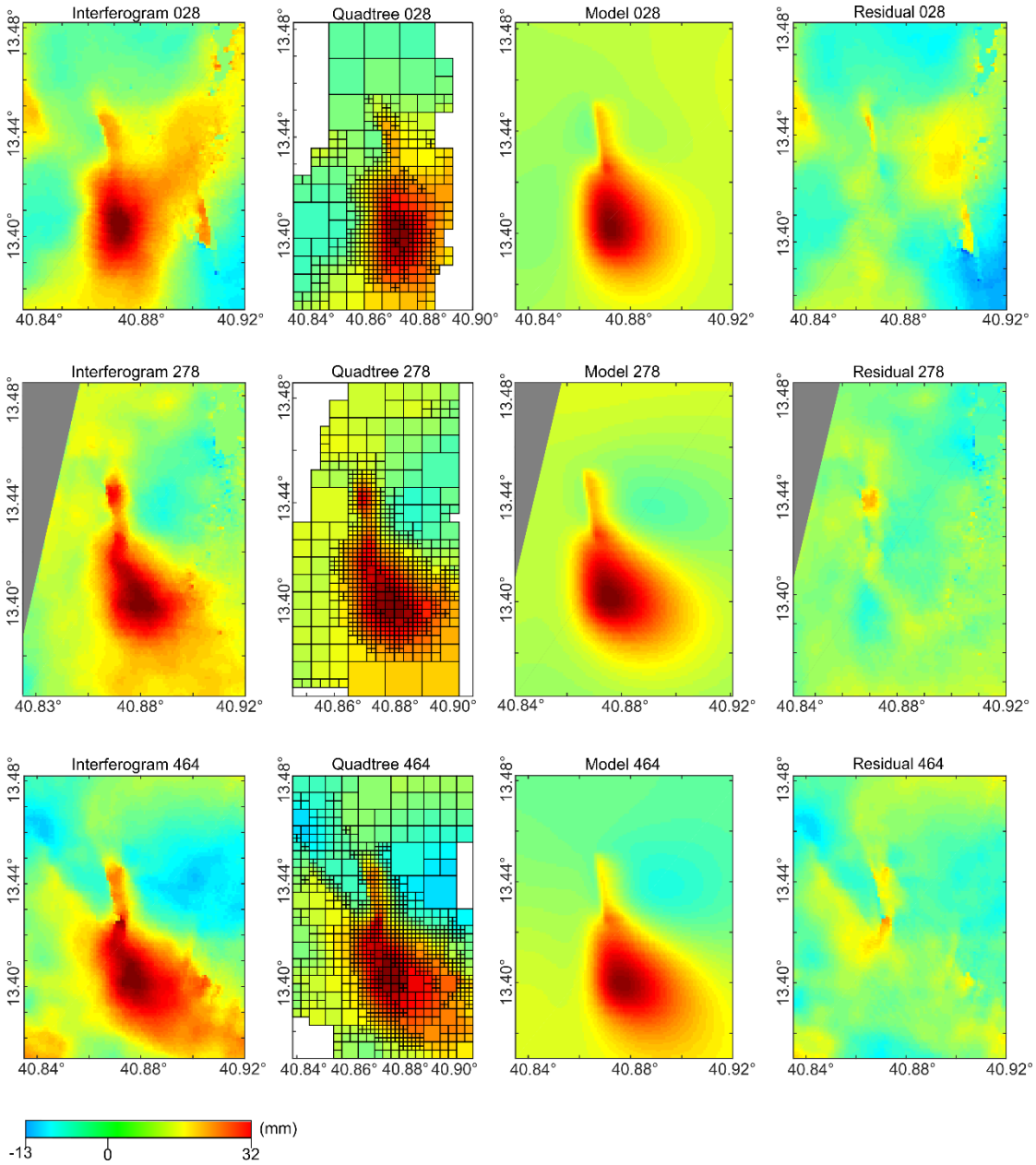

Figure A1 - InSAR data inversion procedure and results related to the best-fit model. Interferometric phase is unwrapped as shown in Figure 3.6. Quadtree partitioning has been carried out using an RMS threshold of 1.0 mm. A total of 2376 data points are left in the down-sampled dataset.

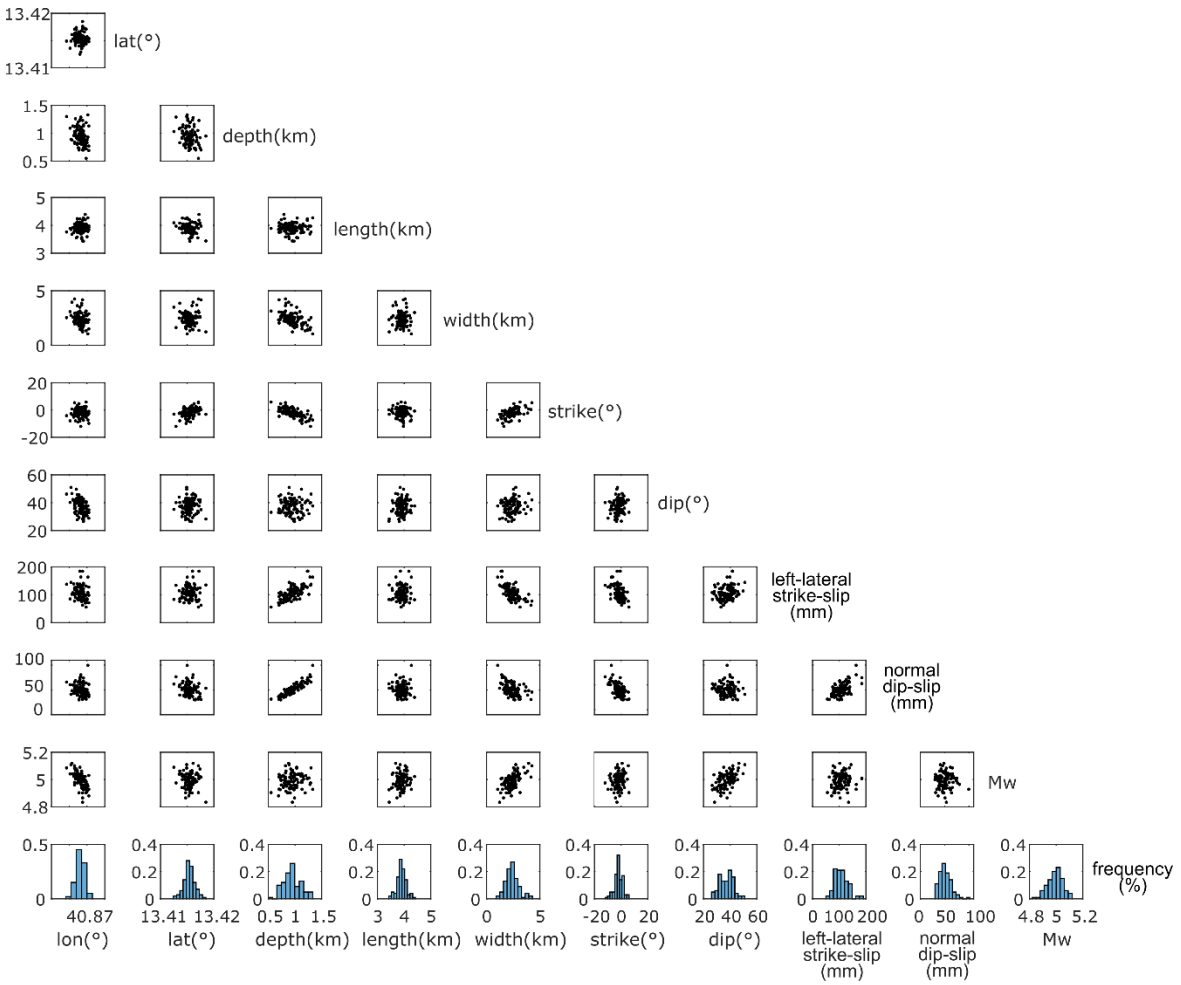

Figure A2 - Distribution of the model parameters for the main fault segment of the best-fit solution computed using 100 Monte-Carlo simulations. The scatter plots show the parameters trad-off while histograms show the distribution of the individual model parameters.

Parameter	90% Conf. Int.	
Lon. (°)	40.8685	40.8700
Lat. (°)	13.4140	13.4171
Depth (km)	0.72	1.23
Length (km)	3.58	4.18
Width (km)	1.46	3.49
Strike (°)	-7.9	2.4
Dip (°)	28.9	44.7
Strike-slip (mm)	75.4	139.4
Dip-slip (mm)	35	71.1
M_w	4.9	5.07

Table A1 - 90% confidence interval for each best-fit model parameters of the main fault segment.

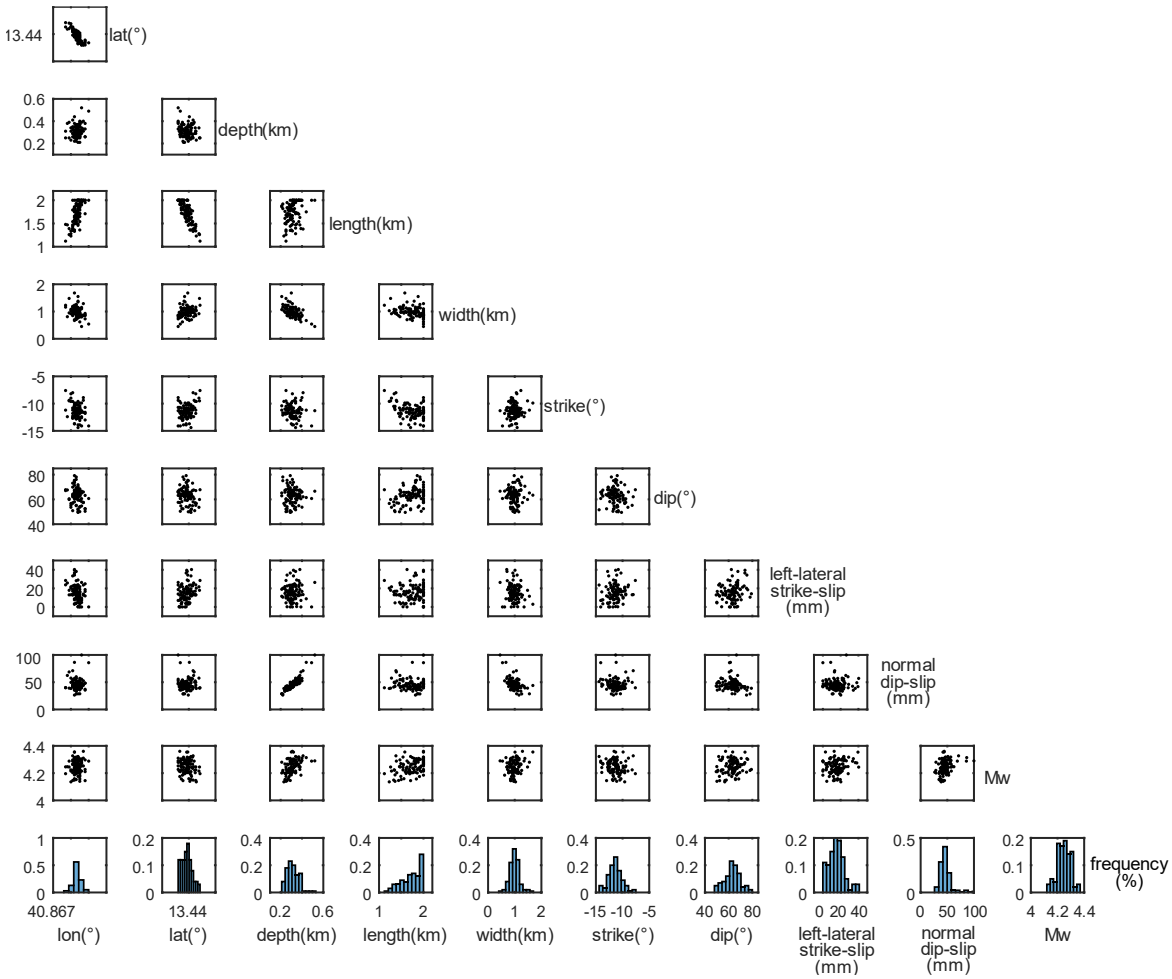

Figure A3 - Distribution of the model parameters for the second fault segment of the best-fit solution computed using 100 Monte-Carlo simulations. The scatter plots show the parameters trad-off while histograms show the distribution of the individual model parameters.

Parameter	90% Conf. Int.	
Lon (°)	40.8680	40.8687
Lat (°)	13.4382	13.4413
Depth(km)	0.24	0.39
Length(km)	1.34	2.00
Width(km)	0.71	1.26
Strike (°)	-13.7	-9.4
Dip (°)	51.6	73.7
Strike-slip (mm)	4	29
Dip-slip (mm)	34.4	62.4
M_w	4.15	4.32

Table A2 - 90% confidence interval for each best-fit model parameter of the second fault segment.

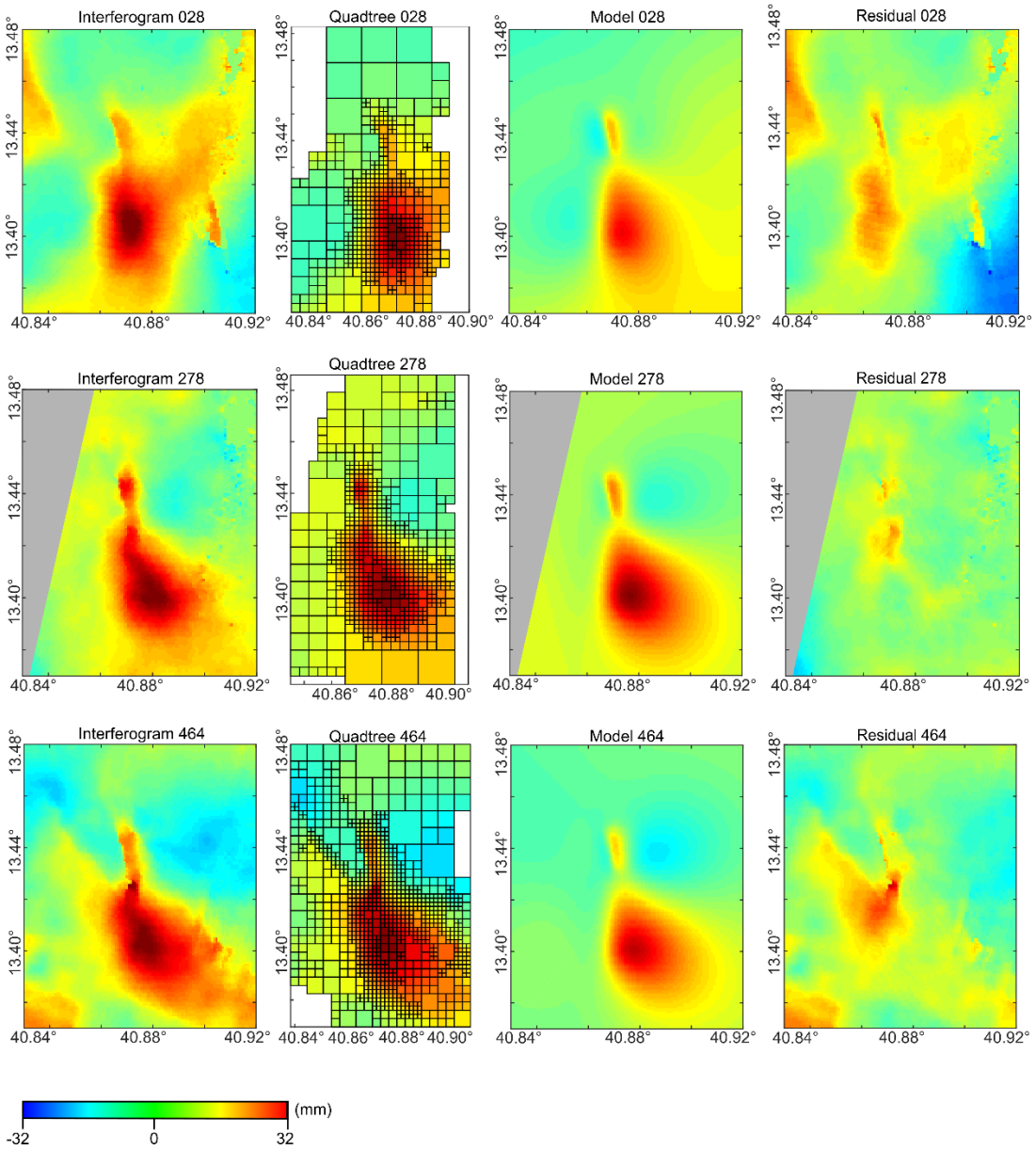

Figure A4 - InSAR data inversion procedure and results related to model with a main fault dip of 65°. Interferometric phase is unwrapped. Quadtree partitioning has been carried out using an RMS threshold of 1.0 mm. A total of 2376 data points are left in the down-sampled dataset.

N°	Lat. (°)	Lon. (°)	Depth (km)	Length (km)	Width (km)	Strike (°)	Dip (°)	Ss (mm)	Ds (mm)
1	13.4162	40.8682	0.94	3.87	2.59	N360E	65.0	148	40
2	13.4393	40.8683	0.33	1.78	0.92	N348E	66.4	7.5	49

Mo (Nm): 5.2×10^{16} **Mw:** 5.1

RMS (mm): **T028** 7.0; **T278** 3.4; **T464** 5.7

Table A3 - Faults parameters from InSAR modelling for the model in Figure A4. Latitude and longitude are the coordinates of the centres of the faults upper edge. Ss is the left-lateral strike-slip component. Ds is the dip-slip normal component. RMS for each independent interferogram.

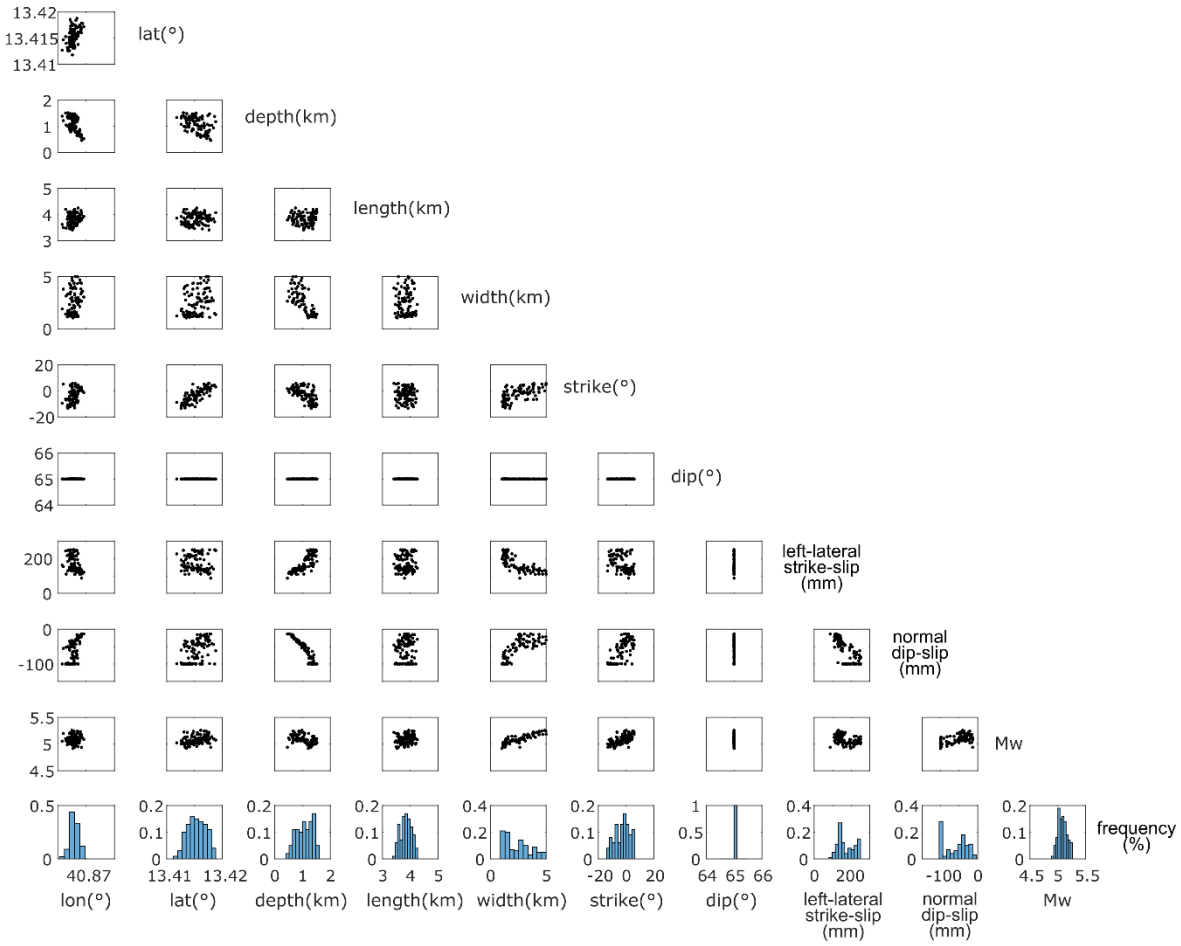

Figure A5 - Distribution of the model parameters for the main fault segment of the solution in Figure A4, computed using 100 Monte-Carlo simulations. The scatter plots show the parameters trad-off while histograms show the distribution of the individual model parameters. Note the inconsistent probability distribution of the dip.

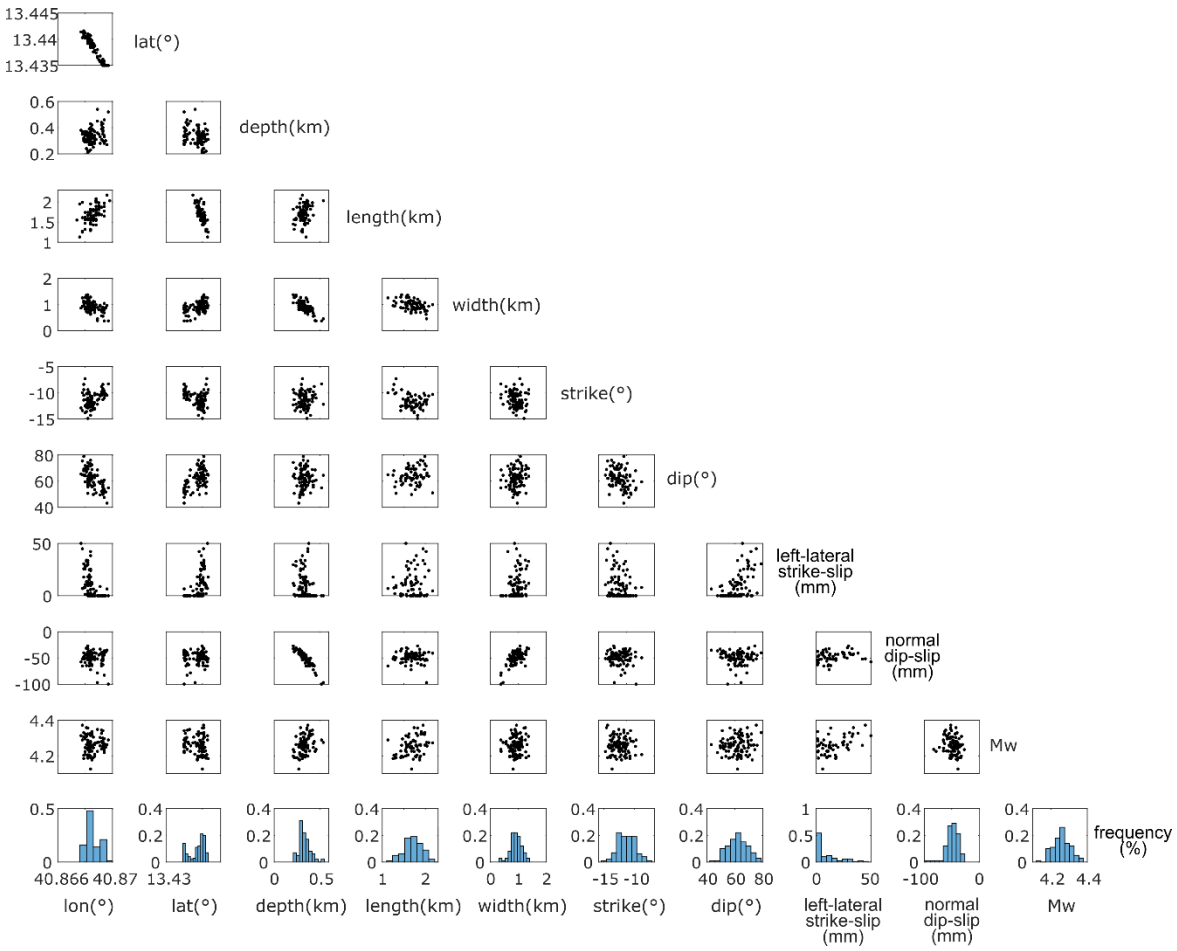

Figure A6 - Distribution of the model parameters for the second fault segment of the solution in Figure A4, computed using 100 Monte-Carlo simulations. The scatter plots show the parameters trad-off while histograms show the distribution of the individual model parameters.

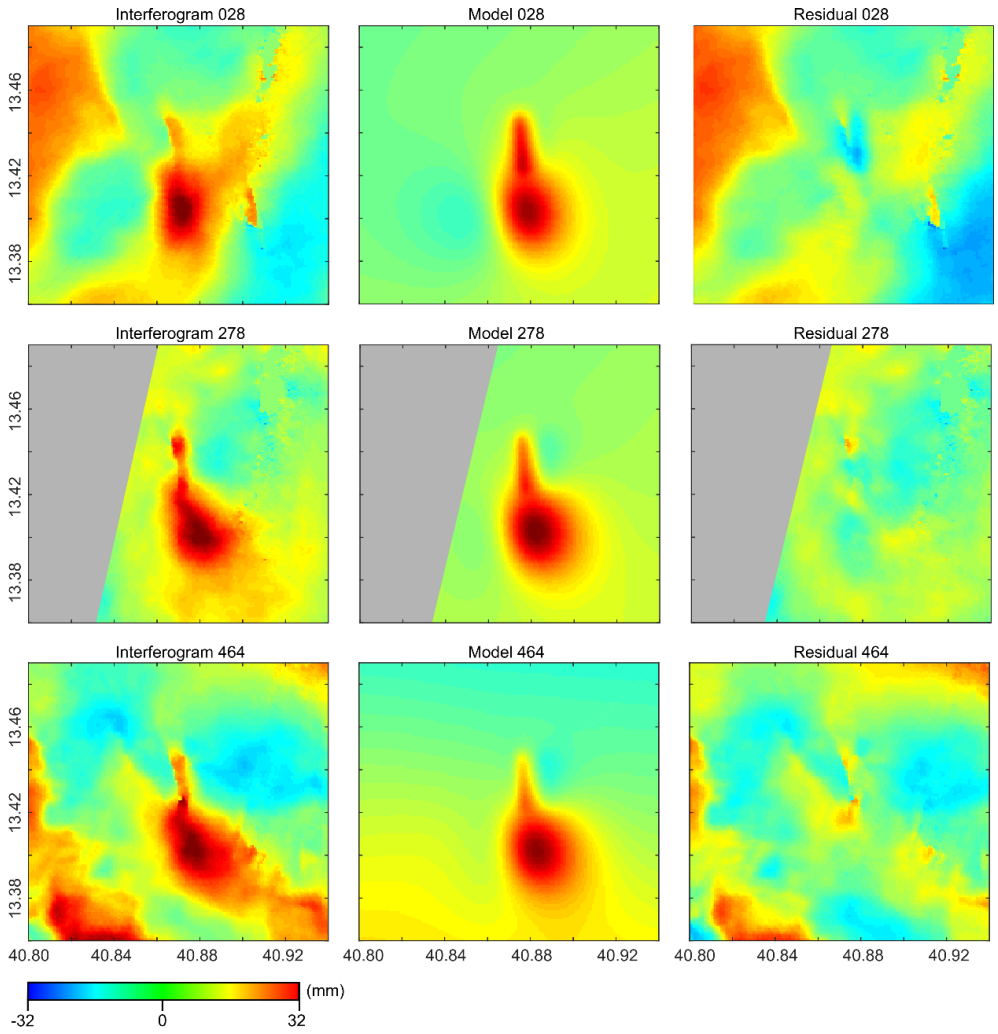

Figure A7. Results of the inversion using a normal fault to fit the deformation related to the main segment. The strike-slip component has been fixed to zero while the other parameters has been let free to vary. It is clear that this solution does not provide a good fit to the data. The parameters of the model are listed in Table A4.

N°	Lat. (°)	Lon. (°)	Depth (km)	Length (km)	Width (km)	Strike (°)	Dip (°)	Ss (mm)	Ds (mm)
1	13.4080	40.8693	1.33	4.02	2.03	N350E	50.0	0.0	94
2	13.4397	40.8684	0.29	1.64	1..00	N350E	58.4	0.0	42

Mo (Nm): 2.7×10^{16} **Mw:** 4.9

RMS:	**T028**	2.9
(mm)	**T278**	5.1
	T464	6.2

Table A4 - Faults parameters from InSAR modelling of the normal fault solution. Latitude and longitude are the coordinates of the centres of the faults upper edge. Ss is the strike-slip component. Ds is the dip-slip normal component. RMS for each independent interferogram.

Longitude	Latitude	Strike1	Dip1	Rake1	Strike2	Dip2	Rake2
40.99	13.55	10	65	-21	110	71	-153

Table A5 - Parameters of the nodal planes describing the CMT solution for the main seismic event of October 2007.

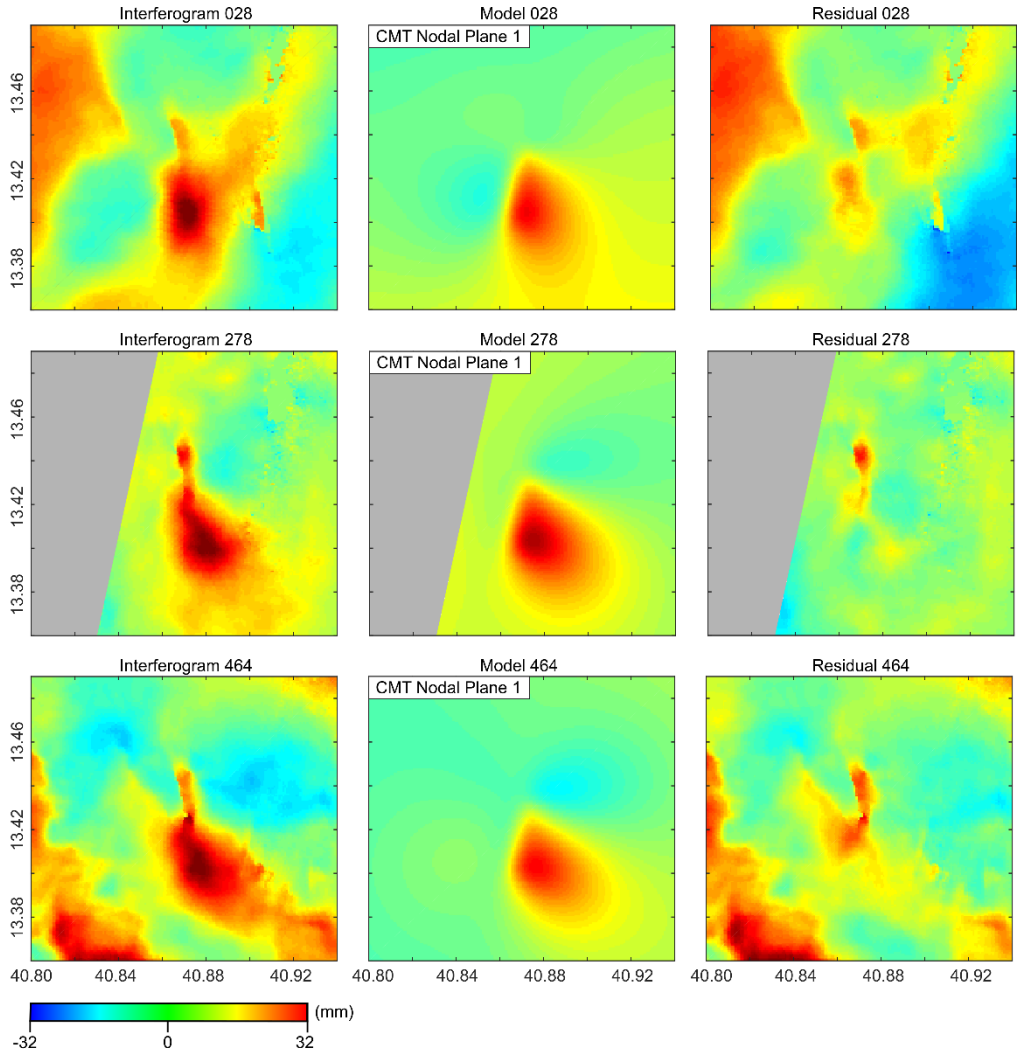

Figure A8. -Results of the inversion test using the parameters of first nodal plane of the CMT solution. The parameters describing the nodal planes are listed in Table A5. The smaller segment has not been modelled. It is clear that this solution does not provide a good fit to the data. The parameters of the model are listed in Table A6.

N°	Lat. (°)	Lon. (°)	Depth (km)	Length (km)	Width (km)	Strike (°)	Dip (°)	Ss (mm)	Ds (mm)
1	13.4186	40.8685	0.92	3.78	4.46	N10E	65.0	108	42

Mo (Nm): 6.32×10^{16} **Mw:** 5.2

RMS: (mm)	**T028**	6.0
	T278	4.6
	T464	6.1

Table A6 - Faults parameters from InSAR modelling of the first nodal plane of the CMT solution. Latitude and longitude are the coordinates of the centres of the faults upper edge. Ss is the left-lateral strike-slip component. Ds is the dip-slip normal component. RMS for each independent interferogram.

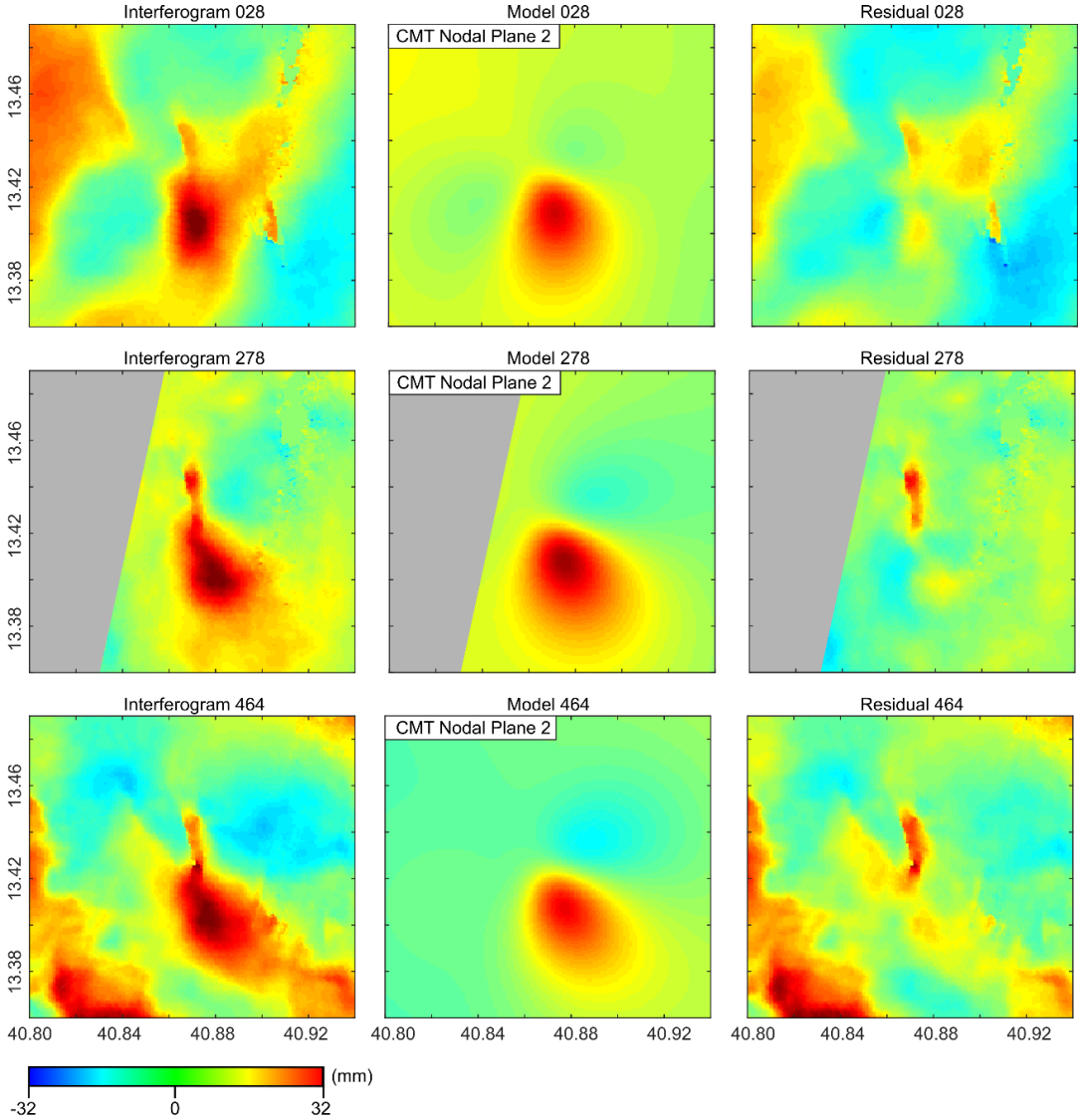

Figure A9 - Results of the inversion test using the parameters of second nodal plane of the CMT solution. The parameters describing the nodal planes are listed in Table A5. The smaller segment has not been modelled. It is clear that this solution does not provide a good fit to the data. The parameters of the model are listed in Table A7.

N°	Lat. (°)	Lon. (°)	Depth (km)	Length (km)	Width (km)	Strike (°)	Dip (°)	Ss (mm)	Ds (mm)
1	13.4211	40.8700	2.06	0.67	3.20	N110E	71.0	-88.7	45.2

Mo (Nm): 6.92×10^{16} **Mw:** 5.2

RMS: (mm)		
	T028	5.0
	T278	5.1
	T464	5.7

Table A7 - Faults parameters from InSAR modelling of the second nodal plane of the CMT solution. Latitude and longitude are the coordinates of the centres of the faults upper edge. Ss is the left-lateral strike-slip component. Ds is the dip-slip normal component. RMS for each independent interferogram.

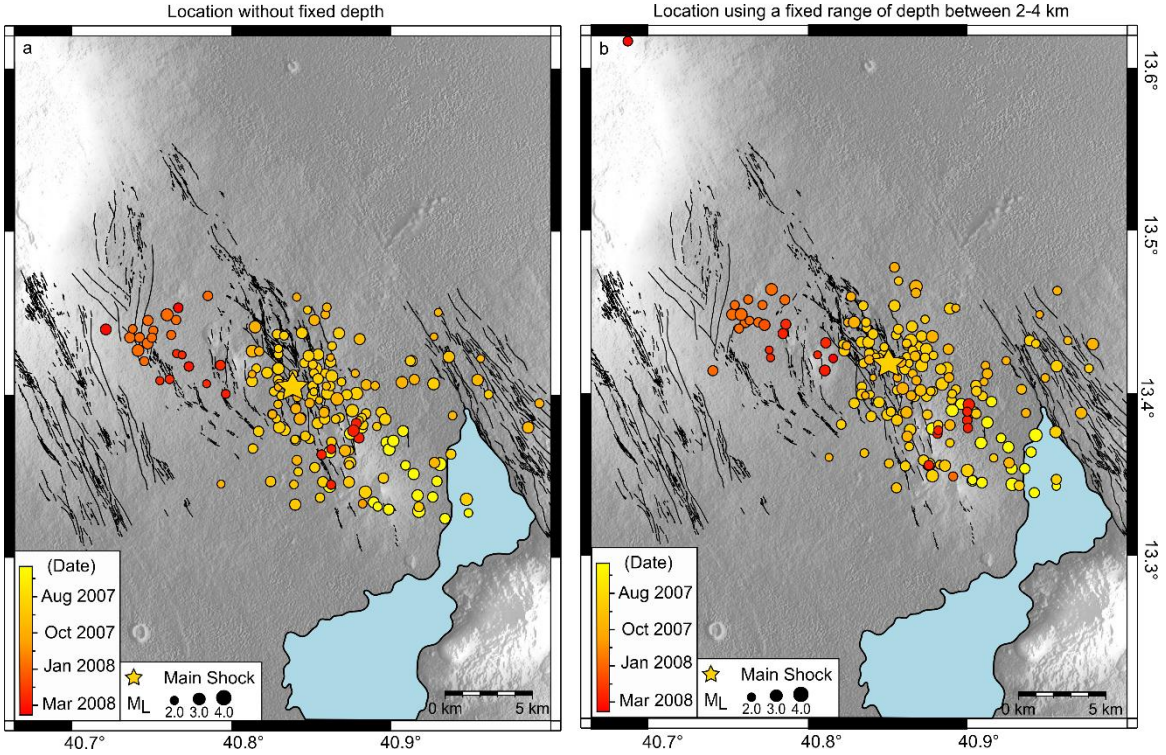

Figure A12 - Seismic locations without fixed depth (a) and seismic locations fixing the depths to range between 2 and 4 km (b) as suggested by InSAR inversion. Seismic locations in (a) and in (b) are similar with the location in (b) characterized by a slight shift to the East. Nevertheless, the earthquakes in (b) are mainly located within the fault zone displaying the same clustering along the main fault system as observed in (a).

Appendix B

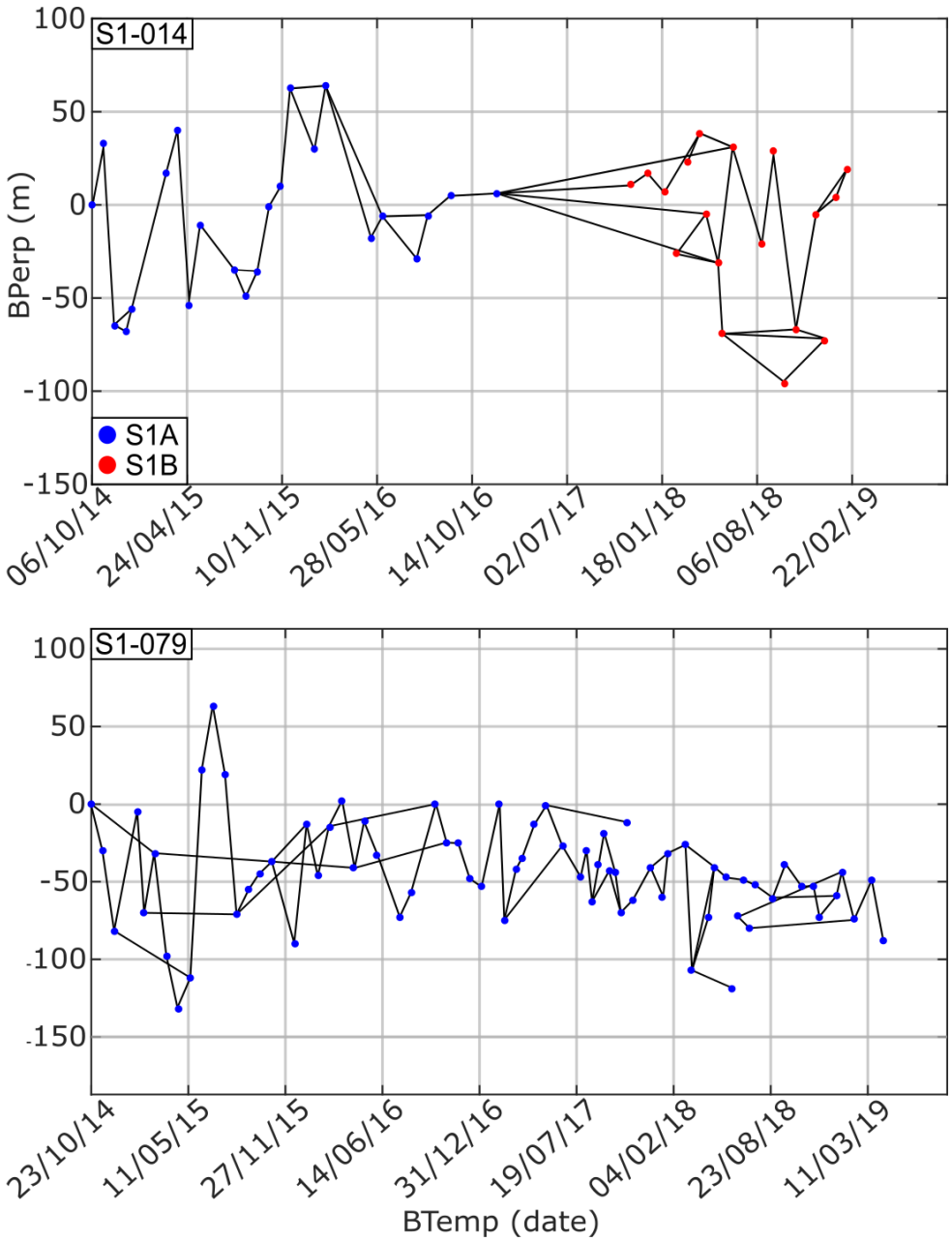

Figure B1 – Networks of interferograms created for S1 ascending 014 and descending 079. The two networks have been created by favoring interferometric pairs with temporal baseline between 12 and 36 day. However, a further manual selection has been performed by visual inspection of the interferograms. On this basis, short interferograms characterized by high levels of noise have been excluded from the networks, while longer interferograms (up to 6 months) with low noise have been kept.

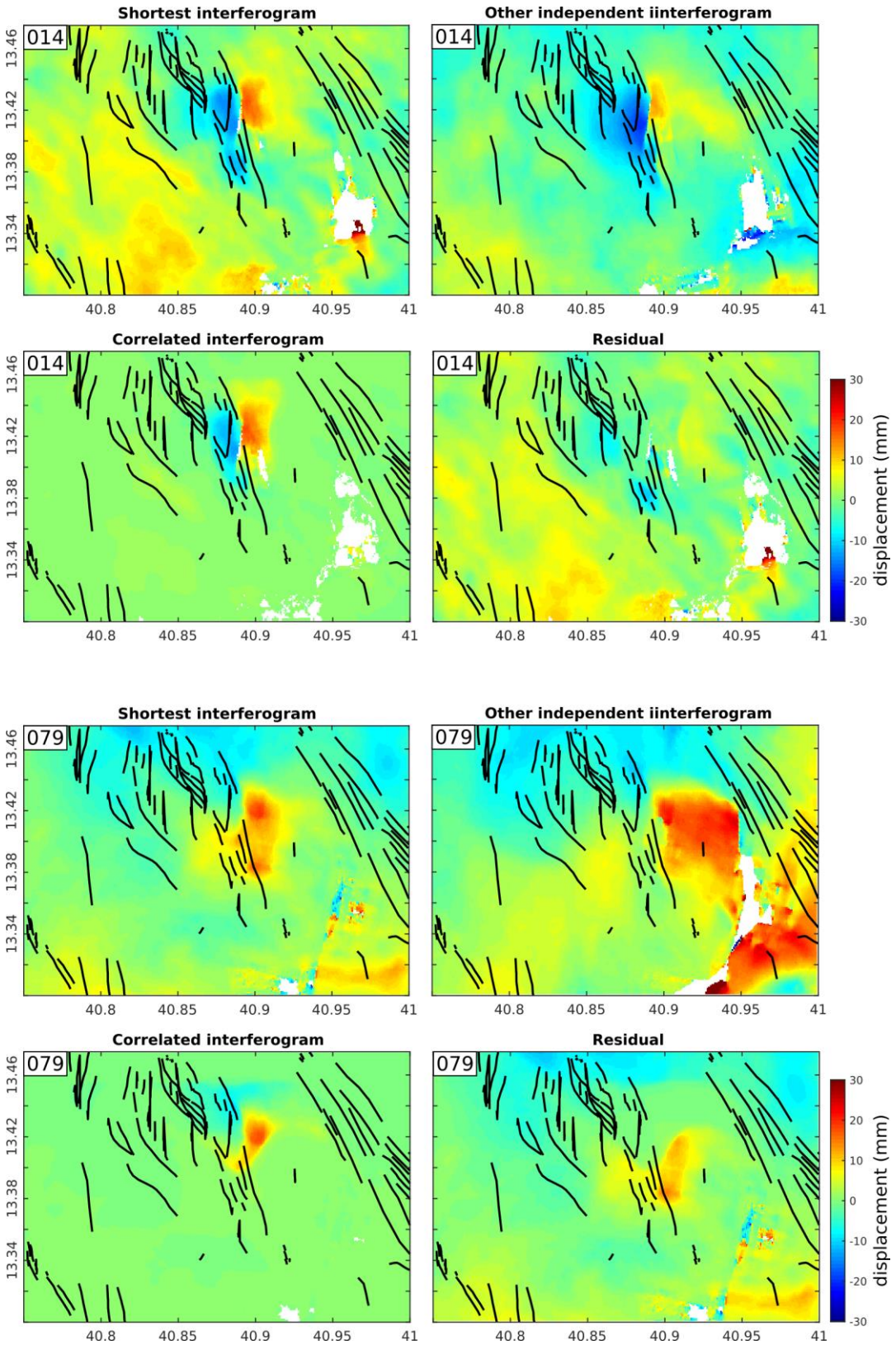

Figure B2 – Removal of the episodic deformation caused by fault slip in January 2018, using the cross-correlation technique. Two independent interferograms are show for each S1 track, along with the correlated deformation and its residual respect to the shortest interferogram.

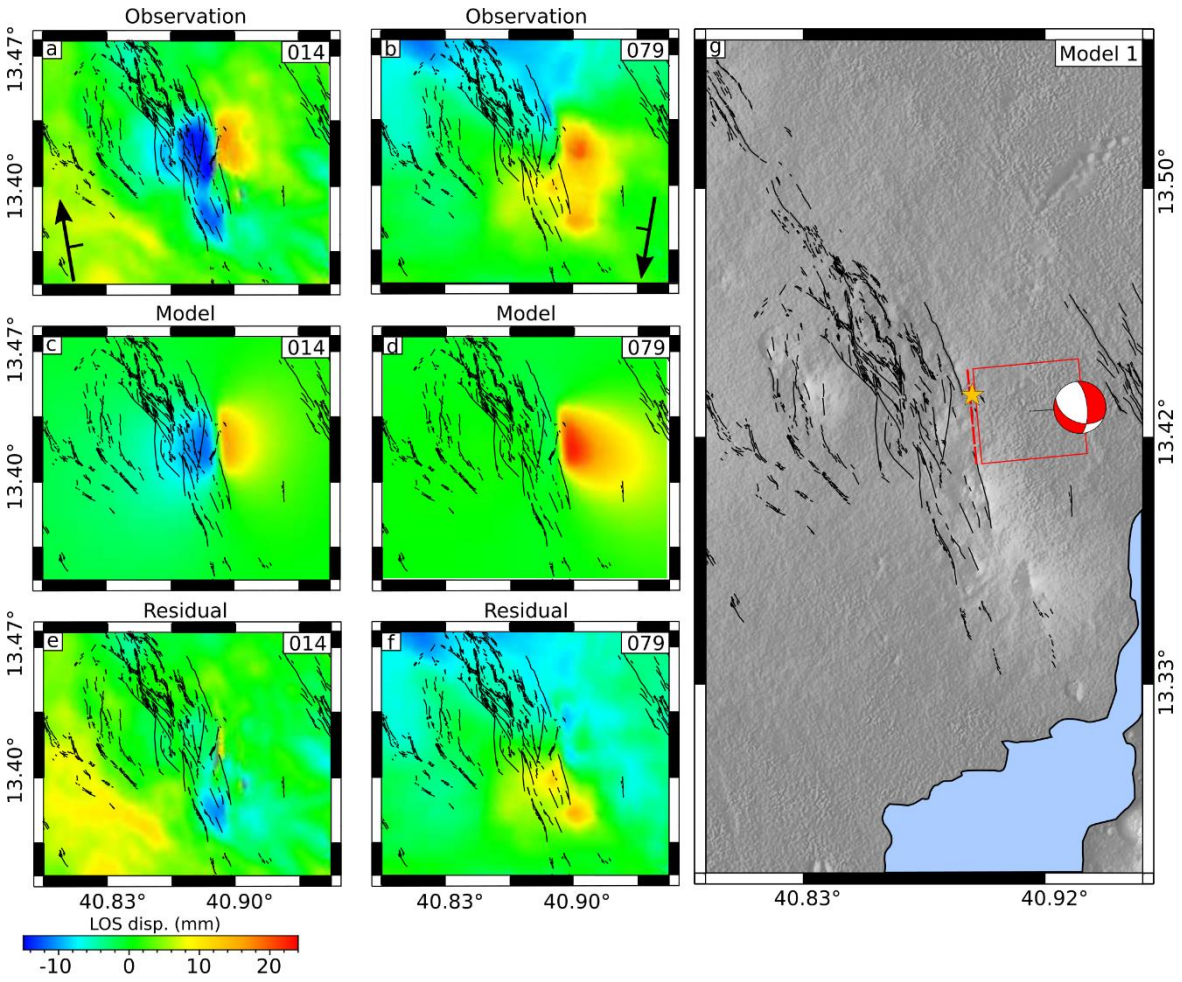

Figure B3 – Best-fit model and associated residuals obtained by inverting the original S1 interferograms. The model is referred as Model 1.

Lat. (°)	Lon. (°)	Depth (km)	Length (km)	Width (km)	Strike (°)	Dip (°)	Ss (mm)	Ds (mm)
13.4238	40.8932	0.46	3.50	10	N354E	67	32.6	44.7

Mo (Nm): 6.3×10^{16} **Mw:** 5.2

RMS: (mm)		
	T014	2.9
	T079	3.1

Table B1. Model 1 parameters. Latitude and longitude are the coordinates of the centres of the faults upper edge. Ss is the left-lateral strike-slip component. Ds is the dip-slip normal component. RMS for each independent interferogram.

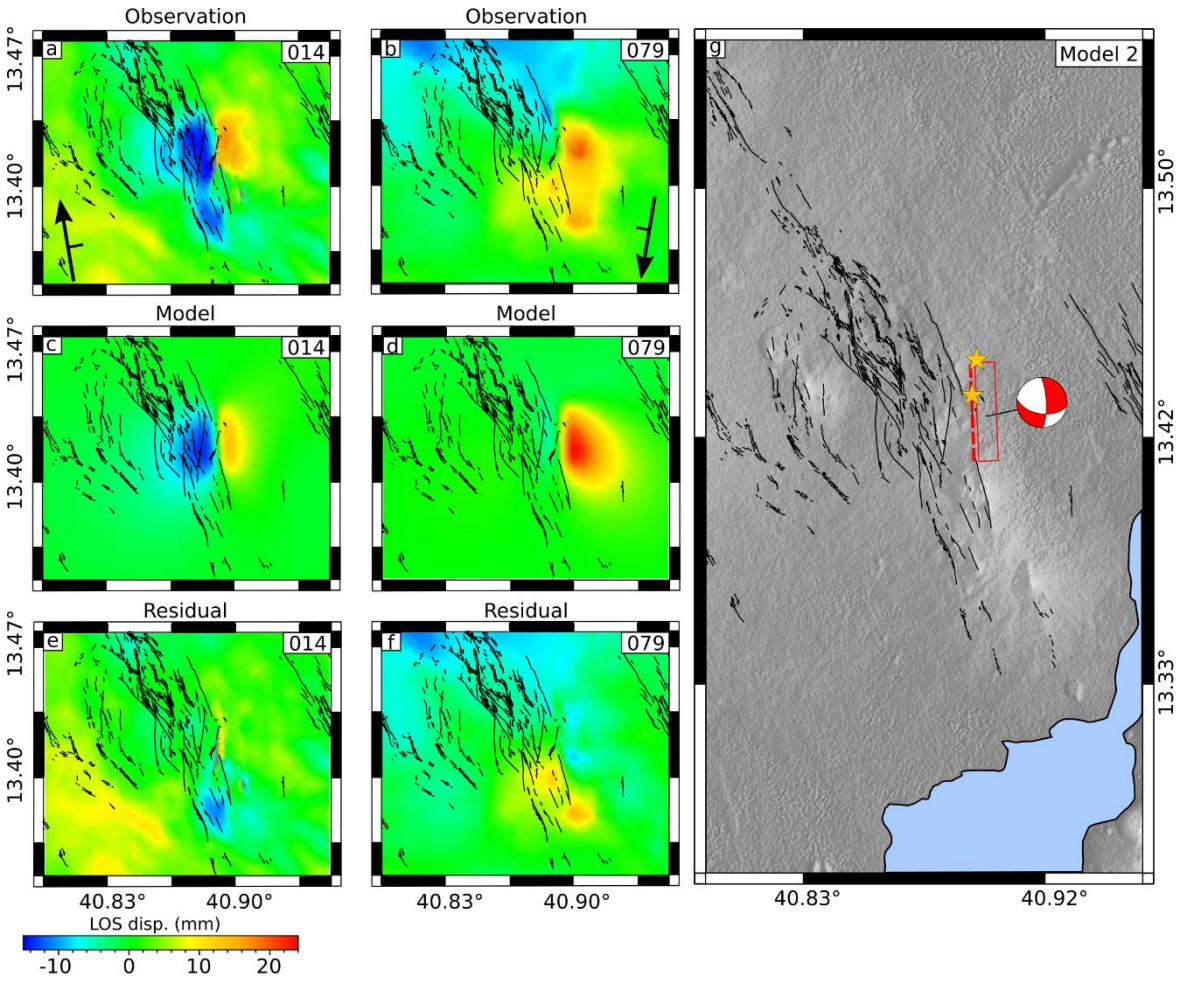

Figure B4 – Best-fit model and associated residuals obtained by inverting the original S1 interferograms and narrowing the research bound for the fault width between 0-3 km. The model is referred as Model 2.

Lat. (°)	Lon. (°)	Depth (km)	Length (km)	Width (km)	Strike (°)	Dip (°)	Ss (mm)	Ds (mm)
13.4251	40.8931	0.68	3.60	3.0	N358E	76	69	55

Mo (Nm): 3.1×10^{16} **Mw:** 5.0

RMS: (mm)		
	T014	3.1
	T079	2.9

Table B2. Model 2 parameters. Latitude and longitude are the coordinates of the centers of the faults upper edge. Ss is the left-lateral strike-slip component. Ds is the dip-slip normal component. RMS for each independent interferogram.

Parameter	90% Conf. Int.	
Lon. (°)	40.8927	40.8929
Lat. (°)	13.4224	13.4229
Depth (km)	0.38	0.44
Length (km)	3.54	3.67
Width (km)	4.25	5.37
Strike (°)	-1.7	-0.9
Dip (°)	66.4	69.1
Strike-slip (mm)	10.1	15.6
Dip-slip (mm)	38	41
Mw	4.853	4.907

Table B3. 90% confidence interval for each parameter of Model 3.

Appendix C

Date and Time	M_L	Strike (°)	σ Strike (°)	Dip (°)	σ Dip (°)	Rake (°)	σ Rake (°)
2018/03/24 10:27	5.3	N154E	3.9	76	6.9	-117	0.9
2018/03/24 10:56	4.3	N184E	0.8	78	0.0	-113	0.0
2018/03/24 11:23	4.0	N146E	0.0	79	0.0	-122	0.0
2018/03/24 21:02	4.5	N180E	3.2	72	1.0	-117	3.1
2018/03/25 01:48	3.3	N348E	3.6	56	4.0	-53	2.0
2018/03/26 00:25	2.5	N355E	1.5	84	0.8	-61	0.5
2018/03/26 00:29	4.2	N181E	4.6	69	7.6	-109	2.2
2018/03/29 18:37	3.8	N145E	4.9	57	4.4	-141	6.2
2018/03/30 06:31	4.6	N184E	1.3	73	3.3	-111	0.4
2018/03/31 00:56	3.5	N340E	2.8	59	3.9	-74.5	0.9
2018/04/02 11:02	3.8	N022E	1.7	78	4.0	-55	0.6
2018/04/02 11:50	4.0	N017E	7.0	61	11.0	-50	9.0
2018/04/07 19:49	3.9	N187E	2.3	79	3.4	-111	2.4
2018/04/11 20:59	3.6	N172E	1.7	84	1.7	-116	0.4
2018/04/15 12:11	4.6	N011E	0.8	87	1.7	-56	1.4
2018/04/15 12:34	4.4	N335E	1.4	75	1.4	-68	0.7
2018/04/15 13:23	4.0	N347E	4.7	59	6.4	-71	2.0
2018/04/15 22:37	4.5	N188E	0.7	84	0.0	-114	0.0
2018/04/20 03:34	3.7	N023E	7.5	48.5	7.8	-41	5.8
2018/04/23 01:25	3.4	N181E	1.8	66.5	3.1	-114	0.7

Table C1 – Parameters of the focal solutions computed for 20 major earthquakes at Dergaha.

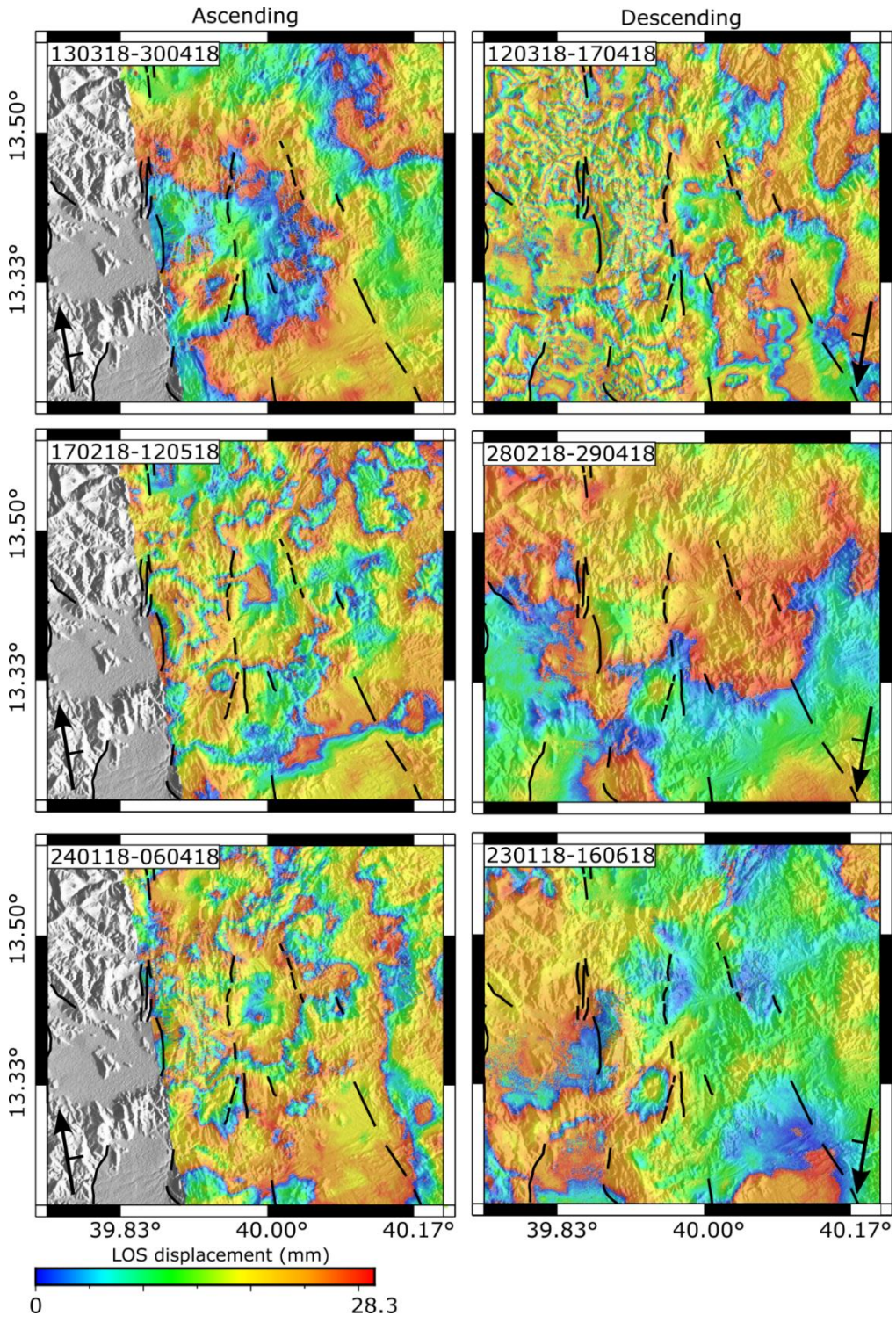

Figure C1 – Sentinel-1 independent interferograms covering the M_L 5.3 earthquake of 24 March 2018, from both ascending (track 014) and descending (track 079) geometry. Black solid lines are fault from Zwaan et al. (2020b).

References

Abdelsalam, M. G., Liégeois, J. P., & Stern, R. J. (2002). The Saharan Metacraton. *Journal of African Earth Sciences*, *34*(3–4), 119–136. https://doi.org/10.1016/S0899-5362(02)00013-1

Acocella, V., & Korme, T. (2002). Holocene extension direction along the Main Ethiopian Rift, East Africa. *Terra Nova*, *14*(3), 191–197. https://doi.org/10.1046/j.1365-3121.2002.00403.x

Acocella, V., Abebe, B., Korme, T., & Barberi, F. (2008). Structure of Tendaho Graben and Manda Hararo Rift: Implications for the evolution of the southern Red Sea propagator in Central Afar. *Tectonics*, *27*(4), 1–17. https://doi.org/10.1029/2007TC002236

Aki, K., & Richards, P. G. (1980). *Quantitative seismology* (Vol. II).

Albaric, J., Déverchère, J., Petit, C., Perrot, J., & Le Gall, B. (2009). Crustal rheology and depth distribution of earthquakes: Insights from the central and southern East African Rift System. *Tectonophysics*, *468*(1–4), 28–41. https://doi.org/10.1016/j.tecto.2008.05.021

Albaric, J., Déverchère, J., Perrot, J., Jakovlev, A., & Deschamps, A. (2014). Deep crustal earthquakes in North Tanzania, East Africa: Interplay between tectonic and magmatic processes in an incipient rift. *Geochemistry, Geophysics, Geosystems*, *15*(2), 374–394. https://doi.org/10.1002/2013GC005027

Allken, V., Huismans, R. S., & Thieulot, C. (2011). Three-dimensional numerical modeling of upper crustal extensional systems. *Journal of Geophysical Research: Solid Earth*, *116*(10), 1–15. https://doi.org/10.1029/2011JB008319

Allken, V., Huismans, R. S., & Thieulot, C. (2012). Factors controlling the mode of rift interaction in brittle-ductile coupled systems: A 3D numerical study. *Geochemistry, Geophysics, Geosystems*, *13*(5), 1–18. https://doi.org/10.1029/2012GC004077

Allken, V., Huismans, R. S., Fossen, H., & Thieulot, C. (2013). 3D numerical modelling of graben interaction and linkage: A case study of the Canyonlands grabens, Utah. *Basin Research*, *25*(4), 436–449. https://doi.org/10.1111/bre.12010

Aochi, H., Poisson, B., Toussaint, R., Rachez, X., & Schmittbuhl, J. (2014). Self-induced seismicity due to fluid circulation along faults. *Geophysical Journal International*, *196*(3), 1544–1563. https://doi.org/10.1093/gji/ggt356

Antonioli, A., Piccinini, D., Chiaraluce, L., Cocco, M. (2005). Fluid flow and seismicity

pattern: Evidence from the 1997 Umbria-Marche (central Italy) seismic sequence. *Geophysical Research Letters, 32*, L10311, https://doi.org/10.1029/2004GL022256

Arnadottir, T., Segall, P., & Matthews, M. (1992). Resolving the discrepancy between geodetic and seismic fault models for the 1989 Loma Prieta, California, earthquake. *Bulletin - Seismological Society of America*, *82*(5), 2248–2255.

Ayele, A., Stuart, G., Bastow, I., & Keir, D. (2007). The August 2002 earthquake sequence in north Afar: Insights into the neotectonics of the Danakil microplate. *Journal of African Earth Sciences*, *48*(2–3), 70–79. https://doi.org/10.1016/j.jafrearsci.2006.06.011

Baker, B. H., Mohr, P. A., & Williams, L. A. J. (1972). Geology of the Eastern Rift System of Africa. *Geological Society of America*, *136*. https://doi.org/10.1130/SPE136

Barberi, F., Ferrara, G., Santacroce, R., Varet, J. (1975). Structural evolution of the Afare triple junction.

Barberi, F., & Varet, J. (1970). The Erta Ale volcanic range (Danakil depression, northern afar, ethiopia). *Bulletin Volcanologique*, *34*(4), 848–917. https://doi.org/10.1007/BF02596805

Barberi, F., Tazieff, H., & Varet, J. (1972). Volcanism in the Afar Depression: Its Tectonic and Magmatic Significance. *Tectonophysics*, *7*(C), 19–29. https://doi.org/10.1016/0040-1951(72)90046-7

Beauducel, F., Briole, P., & Froger, J. L. (2000). Volcano-wide fringes in ERS synthetic aperture radar interferograms of Etna (1992-1998): Deformation or tropospheric effect? *Journal of Geophysical Research: Solid Earth*, *105*(B7), 16391–16402. https://doi.org/10.1029/2000jb900095

Becken, M., Ritter, O., Bedrosian, P. A., & Weckmann, U. (2011). Correlation between deep fluids, tremor and creep along the central San Andreas fault. *Nature*, *480*(7375), 87–90. https://doi.org/10.1038/nature10609

Belachew, M., Ebinger, C., Coté, D., Keir, D., Rowland, J. V., Hammond, J. O. S., & Ayele, A. (2011). Comparison of dike intrusions in an incipient seafloor-spreading segment in Afar, Ethiopia: Seismicity perspectives. *Journal of Geophysical Research: Solid Earth*, *116*(6), 1–23. https://doi.org/10.1029/2010JB007908

Berardino, P., Fornaro, G., Lanari, R., & Sansosti, E. (2002). A new algorithm for monitoring localized deformation phenomena based on small baseline differential SAR interferograms. *IEEE Transactions on Geoscience and Remote Sensing*, *40*(11), 2375–

2383. https://doi.org/10.1109/TGRS.2002.803792

Beyene, A., & Abdelsalam, M. G. (2005). Tectonics of the Afar Depression: A review and synthesis. *Journal of African Earth Sciences*, *41*(1–2), 41–59. https://doi.org/10.1016/j.jafrearsci.2005.03.003

Biggs, J., Wright, T., Lu, Z., & Parsons, B. (2007). Multi-interferogram method for measuring interseismic deformation: Denali Fault, Alaska. *Geophysical Journal International*, *170*(3), 1165–1179. https://doi.org/10.1111/j.1365-246X.2007.03415.x

Birhanu, Y., Bendick, R., Fisseha, S., Lewi, E., Floyd, M., King, R., & Reilinger, R. (2016). GPS constraints on broad scale extension in the Ethiopian Highlands and Main Ethiopian Rift. *Geophysical Research Letters*, *43*(13), 6844–6851. https://doi.org/10.1002/2016GL069890

Boccaletti, M., Bonini, M., Mazzuoli, R., Abebe, B., Piccardi, L., & Tortorici, L. (1998). Quatemary oblique extensional tectonics in the Ethiopian Rift (Horn of Africa). *Tectonophysics*, *287*, 97–116. https://doi.org/10.1016/S0040-1951(98)80063-2

Bonatti, E., Gasperini, E., Vigliotti, L., Lupi, L., Vaselli, O., Polonia, A., & Gasperini, L. (2017). Lake Afrera, a structural depression in the Northern Afar Rift (Red Sea). *Heliyon*, *3*(5), e00301. https://doi.org/10.1016/j.heliyon.2017.e00301

Brace, W. F., & Byerlee, J. D. (1970). California earthquakes: Why only shallow focus? *Science*, *168*(3939), 1573–1575. https://doi.org/10.1126/science.168.3939.1573

Brinckmann, J., Kading C., Knetsch, G., Kurten, M. Mayrhofer, H., Richter-Bernburg G. (1970) Geological Sketchmap of the Danakil Depression.

Brune, S., Corti, G., & Ranalli, G. (2017). Controls of inherited lithospheric heterogeneity on rift linkage: Numerical and analog models of interaction between the Kenyan and Ethiopian rifts across the Turkana depression. *Tectonics*, *36*(9), 1767–1786. https://doi.org/10.1002/2017TC004739

Byerlee, J. D.(1978). Friction of Rocks. *Pageoph*, *116*.

Byerlee, J. D.(1993). Model for episodic flow of high-pressure water in fault zones before earthquakes. *Geology*, *21*(4), 303–306. https://doi.org/10.1130/0091-7613(1993)021<0303:MFEFOH>2.3.CO;2

Byerlee, J. D., & Brace, W. F. (1968). Stick Slip, Stable Sliding, and Earthquakes. Effect of Rock Type, Pressure, Strain Rate, and Stiffness. *Journal of Geophysical Research*, *73*(18), 6031–6037.

Cavalié, O., Doin, M. P., Lasserre, C., & Briole, P. (2007). Ground motion measurement in

the Lake Mead area, Nevada, by differential synthetic aperture radar interferometry time series analysis: Probing the lithosphere rheological structure. *Journal of Geophysical Research: Solid Earth*, *112*(3), 1–18. https://doi.org/10.1029/2006JB004344

Celerier, B. (2008). Seeking Anderson's Faulting in Seismicity: a Centennial Celebration. *Reviews of Geophysics*, (2007), 1–34. https://doi.org/10.1029/2007RG000240.1.INTRODUCTION

Cervelli, P., Murray, M. H., Segall, P., Aoki, Y., & Kato, T. (2001). Estimating source parameters from deformation data, with an application to the March 1997 earthquake swarm off the Izu Peninsula, Japan. *Journal of Geophysical Research: Solid Earth*, *106*(B6), 11217–11237. https://doi.org/10.1029/2000JB900399

Cheloni, D., D'Agostino, N., Scognamiglio, L., Tinti, E., Bignami, C., Avallone, A., et al. (2019). Heterogeneous behavior of the Campotosto normal fault (Central Italy) imaged by InSAR GPS and strong-motion data: Insights from the 18 January 2017 events. *Remote Sensing*, *11*(12). https://doi.org/10.3390/rs11121482

Chen, C. W., & Zebker, H. A. (2002). Phase unwrapping for large SAR interferograms: Statistical segmentation and generalized network models. *IEEE Transactions on Geoscience and Remote Sensing*, *40*(8), 1709–1719. https://doi.org/10.1109/TGRS.2002.802453

Corti, G. (2008). Control of rift obliquity on the evolution and segmentation of the main Ethiopian rift. *Nature Geoscience*, *1*(4), 258–262. https://doi.org/10.1038/ngeo160

Corti, G. (2012). Evolution and characteristics of continental rifting: Analog modeling-inspired view and comparison with examples from the East African Rift System. *Tectonophysics*, *522–523*(1), 1–33. https://doi.org/10.1016/j.tecto.2011.06.010

Corti, G., & Dooley, T. P. (2015). Lithospheric-scale centrifuge models of pull-apart basins. *Tectonophysics*, *664*, 154–163. https://doi.org/10.1016/j.tecto.2015.09.004

Corti, G., Bonini, M., Conticelli, S., Innocenti, F., Manetti, P., & Sokoutis, D. (2003). Analogue modelling of continental extension: A review focused on the relations between the patterns of deformation and the presence of magma. *Earth-Science Reviews*, *63*(3–4), 169–247. https://doi.org/10.1016/S0012-8252(03)00035-7

Craig, T. J., Jackson, J. A., Priestley, K., & Mckenzie, D. (2011). Earthquake distribution patterns in Africa: Their relationship to variations in lithospheric and geological structure, and their rheological implications. *Geophysical Journal International*,

185(1), 403–434. https://doi.org/10.1111/j.1365-246X.2011.04950.x

Cunningham, W. D., & Mann, P. (2007). Tectonics of strike-slip restraining and releasing bends. *Geological Society Special Publication*, *290*, 1–12. https://doi.org/10.1144/SP290.1

Davis, G. H., Bump, A. P., García, P. E., & Ahlgren, S. G. (2000). Conjugate Riedel deformation band shear zones. *Journal of Structural Geology*, *22*(2), 169–190. https://doi.org/10.1016/S0191-8141(99)00140-6

Dawson, J., & Tregoning, P. (2007). Uncertainty analysis of earthquake source parameters determined from InSAR: A simulation study. *Journal of Geophysical Research: Solid Earth*, *112*(9), 1–13. https://doi.org/10.1029/2007JB005209

De Michele, M., Raucoules, D., Rolandone, F., Briole, P., Salichon, J., Lemoine, A., & Aochi, H. (2011). Spatiotemporal evolution of surface creep in the Parkfield region of the San Andreas Fault (1993-2004) from synthetic aperture radar. *Earth and Planetary Science Letters*, *308*(1–2), 141–150. https://doi.org/10.1016/j.epsl.2011.05.049

De Zan, F., & Guarnieri, A. M. (2006). TOPSAR: Terrain observation by progressive scans. *IEEE Transactions on Geoscience and Remote Sensing*, *44*(9), 2352–2360. https://doi.org/10.1109/TGRS.2006.873853

De Zan, F., Guarnieri, A. M., Rocca, F., & Tebaldini, S. (2008). Sentinel-1 radar interferometry applications. *Proceedings of the European Conference on Synthetic Aperture Radar, EUSAR*, *1–4*(May 2014), 2–6.

Déverchère, J., Petit, C., Gileva, N., Radziminovitch, N., Melnikova, V., & San'Kov, V. (2001). Depth distribution of earthquakes in the Baikal rift system and its implications for the rheology of the lithosphere. *Geophysical Journal International*, *146*(3), 714–730. https://doi.org/10.1046/j.0956-540X.2001.1484.484.x

Dooley, T. P., & Schreurs, G. (2012). Analogue modelling of intraplate strike-slip tectonics: A review and new experimental results. *Tectonophysics*, *574–575*, 1–71. https://doi.org/10.1016/j.tecto.2012.05.030

Doser, D. I., & Yarwood, D. R. (1994). Deep crustal earthquakes associated with continental rifts. *Tectonophysics*, *229*(1–2), 123–131. https://doi.org/10.1016/0040-1951(94)90008-6

Doubre, C., Déprez, A., Masson, F., Socquet, A., Lewi, E., Grandin, R., et al. (2017). Current deformation in Central Afar and triple junction kinematics deduced from GPS and InSAR measurements. *Geophysical Journal International*, *208*(2), 936–953.

https://doi.org/10.1093/gji/ggw434

Drouin, V. & Sigmundsson, F., (2018). Country-wide deformation fields over Iceland using Sentinel-1 SAR images. *EGU2018-14247, 2018, EGU General Assembly*.

Drouin, V., Sigmundsson, F., Ófeigsson, B.G., Hreinsdóttir, S., Sturkell, E., Einarsson, P., (2017). Deformation in the Northern Volcanic Zone of Iceland 2008–2014: an interplay of tectonic, magmatic, and glacial isostatic deformation. *J. Geophys. Res. Solid Earth* 122, 3158–3178. https://doi.org/10.1002/2016JB013206.

Dunn, M., Horton, S., DeShon, H., & Powell, C. (2010). High-resolution earthquake relocation in the New Madrid seismic zone. *Seismological Research Letters*, *81*(2), 406–413. https://doi.org/10.1785/gssrl.81.2.406

Dzurisin, D., & Lu, Z. (2007). Interferometric synthetic-aperture radar (InSAR). In *Volcano Deformation. Geodetic Monitoring Techniques* (pp. 153–194). Springer-Verlag Berlin Heidelberg New York.

Eagles, G., Gloaguen, R., & Ebinger, C. (2002). Kinematics of the Danakil microplate. *Earth and Planetary Science Letters*, *203*(2), 607–620. https://doi.org/10.1016/S0012-821X(02)00916-0

Ebinger, C. J. (2005). Continental break-up: The East African perspective. *Astronomy and Geophysics*, *46*(2), 2.16-2.21. https://doi.org/10.1111/j.1468-4004.2005.46216.x

Ebinger, C. J., & Sleep, N. H. (1998). Cenozoic magmatism throughout east Africa resulting from impact of a single plume. *Nature*, *395*(October), 788–791. https://doi.org/10.1038/27417

Ebinger, C. J., Ayele, A., Keir, D., Rowland, J., Yirgu, G., Wright, T., et al. (2010). Length and timescales of rift faulting and magma intrusion: The afar rifting cycle from 2005 to present. *Annual Review of Earth and Planetary Sciences*, *38*(February), 439–466. https://doi.org/10.1146/annurev-earth-040809-152333

Ebinger, C. J., & Casey, M. (2001). Continental breakup in magmatic provinces: An Ethiopian example. *Geology*, *29*(6), 527–530. https://doi.org/10.1130/0091-7613(2001)029<0527:CBIMPA>2.0.CO;2

Ebinger, C. J., Yemane, T., Woldegabriel, G., Aronson, J. L., & Walter, R. C. (1993). Late Ecocene-Recent volcanism and faulting in the southern main Ethiopian rift. *Journal - Geological Society (London)*, *150*(1), 99–108. https://doi.org/10.1144/gsjgs.150.1.0099

Ebinger, C. J., Keir, D., Ayele, A., Calais, E., Wright, T. J., Belachew, M., et al. (2008). Capturing magma intrusion and faulting processes during continental rupture:

Seismicity of the Dabbahu (Afar) rift. *Geophysical Journal International*, *174*(3), 1138–1152. https://doi.org/10.1111/j.1365-246X.2008.03877.x

Ebinger, C. J., Karner, G. D., & Weissel, J. K. (1991). Mechanical strength of extended continental lithosphere: Constraints from the Western Rift System, East Africa. *Tectonics*, *10*(6), 1239–1256. https://doi.org/10.1029/91TC00579

Einarsson, P. (2008). Plate boundaries, rift and transforms in Iceland. *Jökull*, *58*(August).

Einarsson, P. (2010). Mapping of Holocene surface ruptures in the South Iceland Seismic Zone. *Jökull* 60, 121–138.

Einarsson, P., Björnsson, S., Foulger, G., Stefánsson, R., Skaftadóttir, Þ., 1981. Seismicity pattern in the South Iceland seismic zone. *In: Simpson, D., Richards, P. (Eds.), Earthquake Prediction - an International Review. American Geophys. Union, Maurice Ewing Series* 4, 141–151. https://doi.org/10.1029/ME004p0141

Elliott, J. R., Biggs, J., Parsons, B., & Wright, T. J. (2008). InSAR slip rate determination on the Altyn Tagh Fault, northern Tibet, in the presence of topographically correlated atmospheric delays. *Geophysical Research Letters*, *35*(12), 1–5. https://doi.org/10.1029/2008GL033659

Ekström, G., Nettles, M., & Dziewoński, A. M. (2012). The global CMT project 2004–2010: Centroid-moment tensors for 13,017 earthquakes. Physics of the Earth and Planetary Interiors, 200, 1-9. https://doi.org/10.1016/j.pepi.2012.04.002

European Space Agency (ESA) (2000-2020). https://earth.esa.int/eogateway/

Farr, T. G., Rosen, P., Caro, E., Crippen, R., Duren, R., Hensley, S., et al. (2007). The Shuttle Radar Topoghraphy Mission. *Reviews of Geophysics*, *45*. https://doi.org/10.1029/2005RG000183

Ferretti, A., Monti-Guarnieri, A., Prati, C., Rocca, M., Massonnet, D. (2007) *InSAR Principle: Guidelines for SAR Interferometry Processing and Interpretation*. Eds: Fletcher, K. ESA Pubblications.

Ferretti, A., Prati, C., & Rocca, F. (2001). Permanent scatterers in SAR interferometry. *IEEE Transactions on Geoscience and Remote Sensing*, *39*(1), 8–20. https://doi.org/10.1109/36.898661

Finnegan, N. J., Pritchard, M. E., Lohman, R. B., & Lundgren, P. R. (2008). Constraints on surface deformation in the Seattle, WA, urban corridor from satellite radar interferometry time-series analysis. *Geophysical Journal International*, *174*(1), 29–41. https://doi.org/10.1111/j.1365-246X.2008.03822.x

Fornaro, G., & Franceschetti, G. (1995). Image registration in interferometric SAR processing. *IEE Proceedings: Radar, Sonar and Navigation*, *142*(6), 313–320. https://doi.org/10.1049/ip-rsn:19952174

Foulger, G., R. Bilham, W. J. Morgan, and P. Einarsson (1987). The iceland GPS geodetic field campain 1986, Eos Trans. AGU, 68(52), 1809–1818. https://doi.org/10.1029/EO068i052p01809-02.Funning, G. J., & Garcia, A. (2019). A systematic study of earthquake detectability using Sentinel-1 InterferometricWide-Swath data. *Geophysical Journal International*, *216*(1), 332–349. https://doi.org/10.1093/gji/ggy426

George, R., Rogers, N., & Kelley, S. (1998). Earliest magmatism in Ethiopia: Evidence for two mantle plumes in one flood basalt province. *Geology*, *26*(10), 923–926. https://doi.org/10.1130/0091-7613(1998)026<0923:EMIEEF>2.3.CO;2

Gerya, T. V. (2013). Initiation of transform faults at rifted continental margins: 3D petrological-thermomechanical modeling and comparison to the Woodlark Basin. *Petrology*, *21*(6), 550–560. https://doi.org/10.1134/S0869591113060039

Geudtner, D., & Torres, R. (2012). Sentinel-1 system overview and performance. *International Geoscience and Remote Sensing Symposium (IGARSS)*, *2013*(September), 1719–1721. https://doi.org/10.1109/IGARSS.2012.6351191

Goitom, B., Oppenheimer, C., Hammond, J. O. S., Grandin, R., Barnie, T., Donovan, A., et al. (2015). First recorded eruption of Nabro volcano, Eritrea, 2011. *Bulletin of Volcanology*, *77*(10). https://doi.org/10.1007/s00445-015-0966-3

Goldstein, R. M., & Werner, C. L. (1998). Radar interferogram filtering for geophysical applications. *Geophysical Research Letters*, *25*(21), 4035–4038. https://doi.org/10.1029/1998GL900033

Goldstein, R. M., Zebker, H. A., & Werner, C. L. (1988). Satellite radar interferometry: Two-dimensional phase unwrapping. *Radio Science*, *23*(4), 713–720. https://doi.org/10.1029/RS023i004p00713

Gouin, P. (1979). Earthquake History of Ethiopia and the Horn of Africa.

Green, R. G., White, R. S., & Greenfield, T. (2014). Motion in the north Iceland volcanic rift zone accommodated by bookshelf faulting. *Nature Geoscience*, *7*(1), 29–33. https://doi.org/10.1038/ngeo2012

Grindlay, N. R., Fox, P. J., & MacDonald, K. C. (1991). Second-order ridge axis discontinuities in the south Atlantic: Morphology, structure, and evolution. *Marine*

Geophysical Researches, *13*(1), 21–49. https://doi.org/10.1007/BF02428194

Hamling, I. J., Ayele, A., Bennati Laura, L., Calais, E., Ebinger, C. J., Keir, D., et al. (2009). Geodetic observations of the ongoing Dabbahu rifting episode: New dyke intrusions in 2006 and 2007. *Geophysical Journal International*, *178*(2), 989–1003. https://doi.org/10.1111/j.1365-246X.2009.04163.x

Hamlyn, J. E., Keir, D., Wright, T. J., Neuberg, J. W., Goitom, B., Hammond, J. O. S., et al. (2014). Seismicity and subsidence following the 2011 Nabro eruption , Eritrea : Insights into the plumbing system of an off-rift volcano. *Journal of Geophysical Research : Solid Earth*. https://doi.org/10.1002/2014JB011395.Nabro

Hammond, J. O. S., Kendall, J. M., Stuart, G. W., Keir, D., Ebinger, C., Ayele, A., & Belachew, M. (2011). The nature of the crust beneath the Afar triple junction: Evidence from receiver functions. *Geochemistry, Geophysics, Geosystems*, *12*(12). https://doi.org/10.1029/2011GC003738

Harris, R. A. (2017). Large earthquakes and creeping faults. *Reviews of Geophysics*, *55*(1), 169–198. https://doi.org/10.1002/2016RG000539

Havskov, J., & Ottemoller, L. (2010). *Routine Data Processing In Earthquake Seismology.* Springer Dordrecht Heidelberg London New York

Hein, A. (2004). *Processing of SAR Data*. Springer-Verlag Berlin Heidelberg.

Hutton, L. K., & Boore, D. M. (1987). The ML Scale in Southern California. *Bulletin of the Geological Society of America*, *77*(6), 2074–2094.

Illsley-Kemp, F., Bull, J. M., Keir, D., Gerya, T., Pagli, C., Gernon, T., et al. (2018b). Initiation of a Proto-transform Fault Prior to Seafloor Spreading. *Geochemistry, Geophysics, Geosystems*, *19*(12), 4744–4756. https://doi.org/10.1029/2018GC007947

Illsley-Kemp, F., Keir, D., Bull, J. M., Ayele, A., Hammond, J. O. S., Kendall, J. M., et al. (2017). Local earthquake magnitude scale and b-value for the Danakil region of northern afar. *Bulletin of the Seismological Society of America*, *107*(2), 521–531. https://doi.org/10.1785/0120150253

Illsley-Kemp, F., Keir, D., Bull, J. M., Gernon, T. M., Ebinger, C., Ayele, A., et al. (2018a). Seismicity During Continental Breakup in the Red Sea Rift of Northern Afar. *Journal of Geophysical Research: Solid Earth*, *123*(3), 2345–2362. https://doi.org/10.1002/2017JB014902

Jolivet, R., Grandin, R., Lasserre, C., Doin, M. P., & Peltzer, G. (2011). Systematic InSAR tropospheric phase delay corrections from global meteorological reanalysis data.

Geophysical Research Letters, *38*(17), 1–6. https://doi.org/10.1029/2011GL048757

Jolivet, R., Simons, M., Agram, P. S., Duputel, Z., & Shen, Z. K. (2014). Aseismic slip and seismogenic coupling along the central San Andreas Fault. *Geophysical Research Letters*, *42*(2), 297–306. https://doi.org/10.1002/2014GL062222

Jonsson, S., Zebker, H., Segall, P., & Amelung, F. (2002). Mw7.1 Hector Mine, California, Earthquake, Estimated from Satellite Radar and GPS Measurements. *Bulletin of the Seismological Society of America*, *92*(4), 1377–1389. https://doi.org/10.1785/0120000922

Kanamori, H. (1977). The Energy Release in Greate Earthquakes. *Journal of Geophysical Research*, *82*(20), 2981–2987. https://doi.org/https://doi.org/10.1029/JB082i020p02981

Keir, D., Ebinger, C. J., Stuart, G. W., Daly, E., & Ayele, A. (2006). Strain accommodation by magmatism and faulting as rifting proceeds to breakup: Seismicity of the northern Ethiopian rift. *Journal of Geophysical Research: Solid Earth*, *111*(5), 1–17. https://doi.org/10.1029/2005JB003748

Keir, D., Hamling, I. J., Ayele, A., Calais, E., Ebinger, C., Wright, T. J., et al. (2009). Evidence for focused magmatic accretion at segment centers from lateral dike injections captured beneath the Red Sea rift in Afar. *Geology*, *37*(1), 59–62. https://doi.org/10.1130/G25147A.1

Keir, D., Bastow, I. D., Whaler, K. A., Daly, E., Cornwell, D. G., & Hautot, S. (2009). Lower crustal earthquakes near the Ethiopian rift induced by magmatic processes. *Geochemistry, Geophysics, Geosystems*, *10*(6), 1–10. https://doi.org/10.1029/2009GC002382

Keir, D., Pagli, C., Bastow, I. D., & Ayele, A. (2011). The magma-assisted removal of Arabia in Afar: Evidence from dike injection in the Ethiopian rift captured using InSAR and seismicity. *Tectonics*, *30*(2), 1–13. https://doi.org/10.1029/2010TC002785

Keir, D., Bastow, I. D., Pagli, C., & Chambers, E. L. (2013). The development of extension and magmatism in the Red Sea rift of Afar. *Tectonophysics*, *607*, 98–114. https://doi.org/10.1016/j.tecto.2012.10.015

Keir, D., Doubre, C., Ahmed, H., La Rosa, A., Pagli, C., & Leroy, S. (2020). *Lower crustal intrusion and role of detachment faulting during continental breakup*. Scientific Report.

Khoshmanesh, M., Shirzaei, M., & Nadeau, R. M. (2015). Time-dependent model of aseismic slip on the central San Andreas Fault from InSAR time series and repeating

earthquakes. *Journal of Geophysical Research: Solid Earth*, *120*(9), 3782–3803. https://doi.org/10.1002/2015JB012039

Kidane, T., Courtillot, V., Manighetti, I., Audin, L., Lahitte, P., Quidelleur, X., et al. (2003). New paleomagnetic and geochronologic results from Ethiopian Afar: Block rotations linked to rift overlap and propagation and determination of a ∼2 Ma reference pole for stable Africa. *Journal of Geophysical Research: Solid Earth*, *108*(B2). https://doi.org/10.1029/2001jb000645

Kieffer, B., Arndt, N., Lapierre, H., Bastien, F., Bosch, D., Pecher, A., et al. (2004). Flood and shield basalts from Ethiopia: Magmas from the African superswell. *Journal of Petrology*, *45*(4), 793–834. https://doi.org/10.1093/petrology/egg112

Kim, Y. S., & Sanderson, D. J. (2006). Structural similarity and variety at the tips in a wide range of strike-slip faults: A review. *Terra Nova*, *18*(5), 330–344. https://doi.org/10.1111/j.1365-3121.2006.00697.x

Kim, Y. S., Peacock, D. C. P., & Sanderson, D. J. (2004). Fault damage zones. *Journal of Structural Geology*, *26*(3), 503–517. https://doi.org/10.1016/j.jsg.2003.08.002

Koptev, A., Gerya, T., Calais, E., Leroy, S., & Burov, E. (2018). Afar triple junction triggered by plume-assisted bi-directional continental break-up. *Scientific Reports*, *8*(1), 1–7. https://doi.org/10.1038/s41598-018-33117-3

Kruskal, J. (1956). On the shortest spanning subtree of a graf and the traveling salesman problem. *Proceedings of the American Mathematical Society*, *7*(1), 48–50. https://doi.org/10.2307/2033241

Lahitte, P., Gillot, P.-Y., Kidane, T., Courtillot, V., & Bekele, A. (2003). New age constraints on the timing of volcanism in central Afar, in the presence of propagating rifts. *Journal of Geophysical Research: Solid Earth*, *108*(B2). https://doi.org/10.1029/2001jb001689

Lanari, R., Casu, F., Manzo, M., Zeni, G., Berardino, P., M., M., & Pepe, A. (2007). An Overview of the Small BAseline Subset Algorithm: A DInSAR Technique for Surface Deformation Analysis. *Pure Applied Geophysics*, *164*, 637–661. https://doi.org/https://doi.org/10.1007/978-3-7643-8417-3_2

Lavayssière, A., Drooff, C., Ebinger, C., Gallacher, R., Illsley-Kemp, F., Oliva, S. J., & Keir, D. (2019). Depth Extent and Kinematics of Faulting in the Southern Tanganyika Rift, Africa. *Tectonics*, *38*(3), 842–862. https://doi.org/10.1029/2018TC005379

Le Gall, B., Nonnotte, P., Rolet, J., Benoit, M., Guillou, H., Mousseau-Nonnotte, M., et al. (2008). Rift propagation at craton margin. Distribution of faulting and volcanism in the

North Tanzanian Divergence (East Africa) during Neogene times. *Tectonophysics*, *448*(1–4), 1–19. https://doi.org/10.1016/j.tecto.2007.11.005

Le Pourhiet, L., May, D. A., Huille, L., Watremez, L., & Leroy, S. (2017). A genetic link between transform and hyper-extended margins. *Earth and Planetary Science Letters*, *465*, 184–192. https://doi.org/10.1016/j.epsl.2017.02.043

Lee, H., Muirhead, J. D., Fischer, T. P., Ebinger, C. J., Kattenhorn, S. A., Sharp, Z. D., & Kianji, G. (2016). Massive and prolonged deep carbon emissions associated with continental rifting. *Nature Geoscience*, *9*(2), 145–149. https://doi.org/10.1038/ngeo2622

Leroy, S., d'Acremont, E., Tiberi, C., Basuyau, C., Autin, J., Lucazeau, F., & Sloan, H. (2010). Recent off-axis volcanism in the eastern Gulf of Aden: Implications for plume-ridge interaction. *Earth and Planetary Science Letters*, *293*(1–2), 140–153. https://doi.org/10.1016/j.epsl.2010.02.036

Lomax, A, Michelini, A., & Curtis, A. (2009). Earthquake Location, Direct, Global-Search Methods. In R. Meyers (Ed.), *Encyclopedia of Complexity and Systems Science* (pp. 2449–2473). Springer, Berlin, Heidelberg. https://doi.org/https://doi.org/10.1007/978-3-642-27737-5_150-2

Lomax, Anthony, Virieux, J., Volant, P., & Berge-Thierry, C. (2000). Probabilistic Earthquake Location in 3D and Layered Models. In C. H. Thurber & N. Rabinowitz (Eds.), *Advances in Seismic Event Location* (pp. 101–134). Berlin: Springer. https://doi.org/10.1007/978-94-015-9536-0_5

Macdonald, K. C., Fox, P. J., Perram, L. J., Eisen, M. F., Haymon, R. M., Miller, S. P., et al. (1988). A new view of the mid-ocean ridge from the behaviour of ridge-axis discontinuities. *Nature*, *335*(6187), 217–225. https://doi.org/10.1038/335217a0

Mackenzie, G. D., Thybo, H., & Maguire, P. K. H. (2005). Crustal velocity structure across the Main Ethiopian Rift: Results from two-dimensional wide-angle seismic modelling. *Geophysical Journal International*, *162*(3), 994–1006. https://doi.org/10.1111/j.1365-246X.2005.02710.x

Maguire, P. K. H., Ebinger, C. J., Stuart, G. W., Mackenzie, G. D., Whaler, K. A., Kendall, J. M., et al. (2003). Geophysical project in ethiopia studies continental breakup. *Eos*, *84*(35), 3–8. https://doi.org/10.1029/2003EO350002

Maguire, P. K. H., Keller, G. R., Klemperer, S. L., Mackenzie, G. D., Keranen, K., Harder, S., et al. (2006). Crustal structure of the northern Main Ethiopian Rift from the EAGLE

controlled-source survey; a snapshot of incipient lithospheric break-up. *Geological Society Special Publication*, *259*, 269–292. https://doi.org/10.1144/GSL.SP.2006.259.01.21

Makris, J., & Ginzburg, A. (1987). The Afar Depression: transition between continental rifting and sea-floor spreading. *Tectonophysics*, *141*(1–3), 199–214. https://doi.org/10.1016/0040-1951(87)90186-7

Mandl, G. (1987). Tectonic deformation by rotating parallel faults—The "bookshelf" mechanism. *Tectonophysics*, *141*, 277–316. https://doi.org/https://doi.org/10.1016/0040-1951(87)90205-8

Massonnet, D., & Feigl, K. L. (1998). Radar interferometry and its application to changes in the earth's surface. *Reviews of Geophysics*, *36*(4), 441–500. https://doi.org/10.1029/97RG03139

Massonnet, D., Rossi, M., Carmona, C., Adragna, F., Peltzer, G., Felgl, K., & Rabautet, T. (1993). The displacement field of Lander earthquake mapped by radar interferometry. *Nature*, *364*(July), 138–142. https://doi.org/https://doi.org/10.1038/364138a0

Metzger, S., and S. Jónsson (2014). Plate boundary deformation in North Iceland during 1992–2009 revealed by InSAR time-series analysis and GPS, *Tectonophysics*, 634, 127–138. http://doi.org/10.1016/j.tecto.2014.07.027

Metzger, S., Jónsson, S., Danielsen, G., Hreinsdóttir, S., Jouanne, F., Giardini, D., Villemin, T. (2013). Present kinematics of the Tjörnes Fracture Zone, North Iceland, from campaign and continuous GPS measurements. *Geophysical Journal*, 192 (2), 441-455. http://doi.org/ 10.1093/gji/ggs032

McClay, K. R., Dooley, T. P., Whitehouse, P., & Mills, M. (2002). 4-D evolution of rift systems: Insights from scaled physical models. *AAPG Bulletin*, *86*(6), 935–959. https://doi.org/10.1306/61EEDBF2-173E-11D7-8645000102C1865D

McClusky, S., Reilinger, R., Ogubazghi, G., Amleson, A., Healeb, B., Vernant, P., et al. (2010). Kinematics of the southern Red Sea-Afar Triple Junction and implications for plate dynamics. *Geophysical Research Letters*, *37*(5), 1–5. https://doi.org/10.1029/2009GL041127

McKenzie, D. (1969). The ralation between fault plane solutions for earthquakes and the direction of the principal stresses. *Bulletin of the Seismological Society of America*, *59*(2), 591–601.

McKenzie, D., Davies, D., & Molnar, P. (1970). Plate Tectonics of the Red Sea and East

Africa. *Nature*, *228*, 726–734. https://doi.org/10.1038/226243a0

McKenzie, D. (1978). Some remarks on the development of sedimentary basins. *Earth and Planetary Science Letters*, *40*(1), 25–32. https://doi.org/10.1016/0012-821X(78)90071-7

Merryman Boncori, J. P. (2019). Measuring coseismic deformation with spaceborne synthetic aperture radar: A review. *Frontiers in Earth Science*, *7*(February), 1–20. https://doi.org/10.3389/feart.2019.00016

Meyer, F. J. (2011). Performance requirements for ionospheric correction of low-frequency SAR data. *IEEE Transactions on Geoscience and Remote Sensing*, *49*(10 PART 1), 3694–3702. https://doi.org/10.1109/TGRS.2011.2146786

Modisi, M. P., Atekwana, E. A., Kampunzu, A. B., & Ngwisanyi, T. H. (2000). Rift kinematics during the incipient stages of continental extension: Evidence the nascent Okavango rift basin, Northwest Botswana. *Geology*, *28*(10), 939–942. https://doi.org/10.1130/0091-7613(2000)28<939:RKDTIS>2.0.CO;2

Monti Guarnieri, A., Pasquali, P., Cafforio, C., Guccione, P., & Desnos, Y. L. (2003). ENVISAT ASAR ScanSAR Interferometry. *International Geoscience and Remote Sensing Symposium (IGARSS)*, *2*(C), 1124–1126. https://doi.org/10.1109/igarss.2003.1294032

Moore, C., Wright, T., Hooper, A., & Biggs, J. (2019). The 2017 Eruption of Erta 'Ale Volcano, Ethiopia: Insights Into the Shallow Axial Plumbing System of an Incipient Mid-Ocean Ridge. *Geochemistry, Geophysics, Geosystems*, *20*(12), 5727–5743. https://doi.org/10.1029/2019GC008692

Moore, D. E., & Rymer, M. J. (2007). Talc-bearing serpentinite and the creeping section of the San Andreas fault. *Nature*, *448*(7155), 795–797. https://doi.org/10.1038/nature06064

Mosegaard, K., & Tarantola, A. (1995). Monte Carlo sampling of solutions to inverse problems. *Journal of Geophysical Research*, *100*(B7). https://doi.org/10.1029/94jb03097

Moser, T. J., Van Eck, T., & Nolet, G. (1992). Hypocenter determination in strongly heterogeneous Earth models using the shortest path method. *Journal of Geophysical Research*, *97*(B5), 6563–6572. https://doi.org/10.1029/91JB03176

Nobile, A., Pagli, C., Keir, D., Wright, T. J., Ayele, A., Ruch, J., & Acocella, V. (2012). Dike-fault interaction during the 2004 Dallol intrusion at the northern edge of the Erta Ale

Ridge (Afar, Ethiopia). *Geophysical Research Letters*, *39*(19), 2–7. https://doi.org/10.1029/2012GL053152

Okada, Y. (1985). Surface deformation due to shear and tensile faults in a half-space. *Bulletin - Seismological Society of America*, *75*(4), 1135–1153.

Opheim, J. A., & Gudmundsson, A. (1989). Formation and geometry of fractures, and related volcanism, of the Krafla fissure swarm, northeast Iceland. *Geological Society of America Bulletin*, *101*(12), 1608–1622. https://doi.org/10.1130/0016-7606(1989)101<1608:FAGOFA>2.3.CO;2

Pagli, C., Wright, T. J., Ebinger, C. J., Yun, S.-H., Cann, J. R., Ayele, A., & Barnie, T. (2012). Shallow axial magma chamber at the slow-spreading Erta Ale Ridge. *Nature Geoscience*, *5*(4), 284–288. https://doi.org/DOI: 10.1038/NGEO1414

Pagli, C., Wang, H., Wright, T. J., Calais, E., & Lewi, E. (2014). Current plate boundary deformation of the Afar rift from a 3-D velocity field inversion of InSAR and GPS. *Journal of Geophysical Research: Solid Earth*, *119*, 8562–8575. https://doi.org/10.1002/2014JB011391

Pagli, C., Mazzarini, F., Keir, D., Rivalta, E., & Rooney, T. O. (2015). Introduction: Anatomy of rifting: Tectonics and magmatism in continental rifts, oceanic spreading centers, and transforms. *Geosphere*, *11*(5), 1256–1261. https://doi.org/10.1130/GES01082.1

Pagli, C., Yun, S.-H., Ebinger, C., Keir, D., & Wang, H. (2018). Strike-slip tectonics during rift linkage. *Geology*, *47*(1), 31–34. https://doi.org/10.1130/g45345.1

Parsons, B., Wright, T., Rowe, P., Andrews, J., Jackson, J., Walker, R., et al. (2006). The 1994 Sefidabeh (eastern Iran) earthquakes revisited: New evidence from satellite radar interferometry and carbonate dating about the growth of an active fold above a blind thrust fault. *Geophysical Journal International*, *164*(1), 202–217. https://doi.org/10.1111/j.1365-246X.2005.02655.x

Peltzer, G., Crampé, F., Hensley, S., & Rosen, P. (2001). Transient strain accumulation and fault interaction in the Eastern California shear zone. *Geology*, *29*(11), 975–978. https://doi.org/10.1130/0091-7613(2001)029<0975:TSAAFI>2.0.CO;2

Philippon, M., & Corti, G. (2016). Obliquity along plate boundaries. *Tectonophysics*, *693*, 171–182. https://doi.org/10.1016/j.tecto.2016.05.033

Philippon, M., Willingshofer, E., Sokoutis, D., Corti, G., Sani, F., Bonini, M., & Cloetingh, S. (2015). Slip re-orientation in oblique rifts. *Geology*, *43*(2), 147–150. https://doi.org/10.1130/G36208.1

Prats-Iraola, P., Scheiber, R., Marotti, L., Wollstadt, S., & Reigber, A. (2012). TOPS interferometry with terraSAR-X. *IEEE Transactions on Geoscience and Remote Sensing*, *50*(8), 3179–3188. https://doi.org/10.1109/TGRS.2011.2178247

Reijs, J., & McClay, K. (2003). The Salina del Fraile pull-apart basin , northwest Argentina, 197–209. https://doi.org/10.1144/GSL.SP.2003.210.01.12

Richter, C. F. (1935). An instrumental earthquake magnitude scale. *Bulletin of the Seismological Society of America*, *25*(1), 1–32.

Rooney, T. O., Herzberg, C., & Bastow, I. D. (2012). Elevated mantle temperature beneath East Africa. *Geology*, *40*(1), 27–30. https://doi.org/10.1130/G32382.1

Rosen, P. A., Hensley, S., Joughin, I. R., Li, F. K., Madsen, S. N., Rodriguez, E., & Goldstein, R. M. (2000). Synthetic aperture radar interferometry. *Proceedings of the IEEE*, *88*(3), 333–380. https://doi.org/10.1109/5.838084

Rosen, P. A., Hensley, S., Peltzer, G., & Simons, M. (2004). Updated repeat orbit interferometry package released. *Eos*, *85*(5), 47. https://doi.org/10.1029/2004EO050004

Rosen, P. A., Gurrola, E. M., Sacco, G. F., & Zebker, H. (2012). The InSAR scientific computing environment. In *EUSAR 2012; 9th European Conference on Synthetic Aperture Radar* (pp. 730–733).

Ross, Z. E., Cochran, E. S., Trugman, D. T., & Smith, J. D. (2020). 3D fault architecture controls the dynamism of earthquake swarms. *Science*, *368*(June), 1357–1361.

Ruegg, J. . C., & Kasser, M. (1987). Deformation across the Asal-ghoubbet rift, Djibouti, uplif and crustal extension 1979-1986. Geophysical Research Letters, 14(7), 745–748. https://doi.org/https://doi.org/10.1029/GL014i007p00745

Ruegg, J. C., Tarantola, A., & Physique, D. (1979). Geodetic measurements of rifting associated with a seismo-volcanic crisis in Afar, 6(11).

Rousset, B., Bürgmann, R., & Campillo, M. (2019). Slow slip events in the roots of the San Andreas fault. *Science Advances*, *5*(2), 1–8. https://doi.org/10.1126/sciadv.aav3274

Ruch, J., Anderssohn, J., Walter, T. R., & Motagh, M. (2008). Caldera-scale inflation of the Lazufre volcanic area, South America: Evidence from InSAR. *Journal of Volcanology and Geothermal Research*, *174*(4), 337–344. https://doi.org/10.1016/j.jvolgeores.2008.03.009

Sambridge, M., & Drijkoningen, G. (1992). Genetic algorithms in seismic waveform inversion. *Geophysical Journal International*, *109*(2), 323–342.

https://doi.org/10.1111/j.1365-246X.1992.tb00100.x

Sammis, C. G., Smith, S. W., Nadeau, R. M., & Lippoldt, R. (2016). Relating transient seismicity to episodes of deep creep at Parkfield, California. *Bulletin of the Seismological Society of America*, *106*(4), 1887–1899. https://doi.org/10.1785/0120150224

Sansosti, E., Berardino, P., Manunta, M., Serafino, F., & Fornaro, G. (2006). Geometrical SAR image registration RID F-7297-2011. *Ieee Transactions On Geoscience and Remote Sensing*, *44*(10), 2861–2870. https://doi.org/10.1109/TGRS.2006.875787

Schmidt, D. A., & Bürgmann, R. (2003). Time-dependent land uplift and subsidence in the Santa Clara valley, California, from a large interferometric synthetic aperture radar data set. *Journal of Geophysical Research: Solid Earth*, *108*(B9), 1–13. https://doi.org/10.1029/2002jb002267

Scott, W.B. (1897). An introduction to geology. *Macmillan Ed.,* Second Edition.

Sembroni, A., Molin, P., Dramis, F., Faccenna, C., & Abebe, B. (2017). Erosion-tectonics feedbacks in shaping the landscape: An example from the Mekele Outlier (Tigray, Ethiopia). *Journal of African Earth Sciences*, *129*, 870–886. https://doi.org/10.1016/j.jafrearsci.2017.02.028

Shearer, P. M. (2009). *Introduction to Seismology*. Cambridge University Press.

Shirzaei, M., & Bürgmann, R. (2013). Time-dependent model of creep on the Hayward fault from joint inversion of 18 years of InSAR and surface creep data. *Journal of Geophysical Research: Solid Earth*, *118*(4), 1733–1746. https://doi.org/10.1002/jgrb.50149

Shudofsky, G. N. (1985). Source mechanisms and focal depths of East African earthquakes using Rayleigh-wave inversion and body-wave modelling. *Geophysical Journal of the Royal Astronomical Society*, *83*(3), 563–614. https://doi.org/10.1111/j.1365-246X.1985.tb04328.x

Sibson, R. H. (1996). Structural permeability of fluid-driven fault-fracture meshes. *Journal of Structural Geology*, *18*(8), 1031–1042. https://doi.org/10.1016/0191-8141(96)00032-6

Sigmundsson, F. (1992). Tectonic implications of the 1989 Afar earthquake sequence. *Geophysical Research Letters*, 19 (9), 877-880. https://doi.org/10.1029/92GL00686

Sigmundsson, F. (2006). Iceland Geodynamics: Crustal Deformation and Divergent Plate Tectonics. *Springer Praxis Books Geophysical Sciences*. https://doi.org/10.1007/3-540-

37666-6

Sigmundsson, F., Einarssona, P., Hjartardóttir, A. R., Drouin, V., Jónsdóttir K., Árnadóttir, T., Geirsson, H., Hreinsdóttir, S., Li, S., Ófeigsson B.G. (2020a). Geodynamics of Iceland and the signatures of plate spreading. *Journal of Volcanology and Geothermal Research,* 391, 106436. https://doi.org/10.1016/j.jvolgeores.2018.08.014Sigmundsson, F., Pinel, V., Grapenthin, R. Hooper, A., Halldórsson, S. A., Einarsson, P., Ófeigsson, B.G., Heimisson, E.R., Jónsdóttir, K., Gudmundsson, M. T., Vogfjörd, K., Parks, M., Li, S., Drouin, V., Geirsson, H., Dumont, S., Fridriksdottir, H. M., Gudmundsson, G. B., Wright, T. J., & Yamasaki, T. (2020b) Unexpected large eruptions from buoyant magma bodies within viscoelastic crust. *Nature Communications*, 11, 2403. https://doi.org/10.1038/s41467-020-16054-6

Sigmundsson, F., Hooper, A., Hreinsdóttir, S., Vogfjörd, K. S., Ófeigsson, B. G., Heimisson, E. R., et al. (2015). Segmented lateral dyke growth in a rifting event at Bárðarbunga volcanic system, Iceland. *Nature*, *517*(7533). https://doi.org/10.1038/nature14111

Simons, M., & Rosen, P. A. (2007). Interferometric Synthetic Aperture Radar Geodesy. *Treatise on Geophysics*, *3*, 391–446. https://doi.org/10.1016/B978-044452748-6.00059-6

Snoke, J. A. (2003). FOCMEC: FOCal MEChanism determinations. *International Geophysics*, *81*(PART B), 1629–1630. https://doi.org/10.1016/S0074-6142(03)80291-7

Stab, M., Bellahsen, N., Pik, R., Quidelleur, X., Ayalew, D., & Leroy, S. (2016). Modes of rifting in magma-rich settings: Tectono-magmatic evolution of Central Afar. *Tectonics*, *35*(1), 2–38. https://doi.org/10.1002/2015TC003893

Stein, S., & Wysession, M. (2009). *An Introduction to Seismology, Earthquakes, and Earth Structure*.

Taylor, B., Goodliffe, A., Martinez, F. (2009). Initiation of transform faults at rifted continental margins. Competes Rendus Geoscience, 349, 428-438. https://doi.org/10.1016/j.crte.2008.08.010

Tarantola, A., & Valette, B. (1982). Inverse problems = quest for information. *Journal of Geophysics - Zeitschrift Fur Geophysik*, *50*(3), 159–170.

Tesfaye, S., Harding, D. J., & Kusky, T. M. (2003). Early continental breakup boundary and migration of the Afar triple junction, Ethiopia. *Bulletin of the Geological Society of America*, *115*(9), 1053–1067. https://doi.org/10.1130/B25149.1

Tryggvason, E. (1984). Widening of the Krafla Fissure Swarm During the 1975-1981 Volcano-tectonic Episode. *Bulletin Volcanologique,* 47, 47–69. https://doi.org/10.1007/BF01960540

USGS National Earthquake Information Center (NEIC). https://www.usgs.gov/natural-hazards/earthquake-hazards/earthquakes

Varet, J., 1978. Geology of Central and Southern Afar (Ethiopia and Djibouti Republic) F. Gasse for Chapter IV on Sedimentary Formation. Eds. CNRS, France, Paris, p. 118.

Vidal, P., Deniel, C., Velluntini, P. J., Piguet, P., Coulon, C., Vincent, J., & Audin, J. (1991). CHANGES OF MANTLE SOURCES IN THE COURSE OF A RIFF EVOLUTION: THE AFAR CASE. *Geophysical Research Letters*, *18*(10), 1913–1916. https://doi.org/https://doi.org/10.1029/91GL02006

Vidale, J. E., & Shearer, P. M. (2006). A survey of 71 earthquake bursts across southern California: Exploring the role of pore fluid pressure fluctuations and aseismic slip as drivers. *Journal of Geophysical Research: Solid Earth*, *111*(5), 1–12. https://doi.org/10.1029/2005JB004034

Vigny, C., de Chabalier, J. B., Ruegg, J. C., Huchon, P., Feigl, K. L., Cattin, R., et al. (2007). Twenty-five years of geodetic measurements along the Tadjoura-Asal rift system, Djibouti, East Africa. *Journal of Geophysical Research: Solid Earth*, *112*(6), 1–12. https://doi.org/10.1029/2004JB003230

Volcano Discovery project, https://www.volcanodiscovery.com

Waldhauser, F. (2001). hypoDD: A computer program to compute double-difference hypocenter locations. *U.S. Geol. Surv. Open File Rep.*, *01–113*, 25 pp.

Waldhauser, F., & Ellsworth, W. L. (2000). A Double-difference Earthquake location algorithm: Method and application to the Northern Hayward Fault, California. *Bulletin of the Seismological Society of America*, *90*(6), 1353–1368. https://doi.org/10.1785/0120000006

Wang, H., Wright, T. J., & Biggs, J. (2009). Interseismic slip rate of the northwestern Xianshuihe fault from InSAR data. *Geophysical Research Letters*, *36*(3), 1–5. https://doi.org/10.1029/2008GL036560

Wang, H., Wright, T. J., Yu, Y., Lin, H., Jiang, L., Li, C., & Qiu, G. (2012). InSAR reveals coastal subsidence in the Pearl River Delta, China. *Geophysical Journal International*, *191*(3), 1119–1128. https://doi.org/10.1111/j.1365-246X.2012.05687.x

Wang, H., Elliott, J. R., Craig, T. J., Wright, T. J., Liu-Zeng, J., & Hooper, A. (2014). Normal

faulting sequence in the Pumqu-Xainza Rift constrained by InSAR and teleseismic body-wave seismology. *Geochemistry Geophysics Geosystems*, *15*, 2947–2963. https://doi.org/10.1002/2014GC005369

Wetzel, L. R., Wiens, D. A., & Kleinrockt, M. C. (1993). Evidence from earthquakes for bookshelf faulting at large non-transform ridge offsets. *Nature*, *362*(March), 235–237. https://doi.org/10.1038/362235a0DO

White, R., & McKenzie, D. (1989). Magmatism at rift zones: the generation of volcanic continental margins and flood basalts. *Journal of Geophysical Research*, *94*(B6), 7685–7729. https://doi.org/10.1029/JB094iB06p07685

Wintsch, R. P., Christoffersen, R., & Kronenberg, A. K. (1995). Fluid-rock reaction weakening of fault zones. *Journal of Geophysical Research*, *100*(B7). https://doi.org/10.1029/94jb02622

Wittlinger, G., Herquel, G., & Nakache, T. (1993). Earthquake location in strongly heterogeneous media. *Geophysical Journal International*, *115*(3), 759–777. https://doi.org/10.1111/j.1365-246X.1993.tb01491.x

Wolfenden, E., Ebinger, C., Yirgu, G., Deino, A., & Ayalew, D. (2004). Evolution of the northern Main Ethiopian rift: Birth of a triple junction. *Earth and Planetary Science Letters*, *224*(1–2), 213–228. https://doi.org/10.1016/j.epsl.2004.04.022

Wolfenden, E., Ebinger, C., Yirgu, G., Renne, P. R., & Kelley, S. P. (2005). Evolution of a volcanic rifted margin: Southern Red Sea, Ethiopia. *Bulletin of the Geological Society of America*, *117*(7–8), 846–864. https://doi.org/10.1130/B25516.1

Wright, T., Ebinger, C., Biggs, J., Ayele A., Yirgu, G., Keir, D., & Stork A. (2006) Magma-maintained rift segmentation at continental rupture in the 2005 Afar dyking episode. *Nature,* 442, 291–294. https://doi.org/10.1038/nature04978

Wright, T. J., Parsons, B., & Fielding, E. (2001). Measurement of interseismic strain accumulation across the North Anatolian Fault by satellite radar interferometry. *Geophysical Research Letters*, *28*(10), 2117–2120. https://doi.org/10.1029/2000GL012850

Wright, T. J., Lu, Z., & Wicks, C. (2003). Source model for the Mw 6.7, 23 October 2002, Nenana Mountain Earthquake (Alaska) from InSAR. *Geophysical Research Letters*, *30*(18), 30–33. https://doi.org/10.1029/2003GL018014

Wright, T. J., Lu, Z., & Wicks, C. (2004). Constraining the slip distribution and fault geometry of the Mw7.9, 3 November 2002, Denali fault earthquake with

Interferometric Synthetic Aperture Radar and Global Positioning System data. *Bulletin of the Seismological Society of America*, *94*(6 SUPPL. B), 175–189. https://doi.org/10.1785/0120040623

Wright, T. J., Ebinger, C., Biggs, J., Ayele, A., Yirgu, G., Keir, D., & Stork, A. (2006). Magma-maintained rift segmentation at continental rupture in the 2005 Afar dyking episode. *Nature*, *442*(7100), 291–294. https://doi.org/10.1038/nature04978

Wright, T. J., Sigmundsson, F., Pagli, C., Belachew, M., Hamling, I. J., Brandsdóttir, B., et al. (2012). Geophysical constraints on the dynamics of spreading centres from rifting episodes on land. *Nature Geoscience*, *5*(4), 242–250. https://doi.org/10.1038/ngeo1428

Xu, W., Rivalta, E., & Li, X. (2017). Magmatic architecture within a rift segment: Articulate axial magma storage at Erta Ale volcano, Ethiopia. *Earth and Planetary Science Letters*, *476*, 79–86. https://doi.org/10.1016/j.epsl.2017.07.051

Yague-Martinez, N., Prats-Iraola, P., Gonzalez, F. R., Brcic, R., Shau, R., Geudtner, D., et al. (2016). Interferometric Processing of Sentinel-1 TOPS Data. *IEEE Transactions on Geoscience and Remote Sensing*, *54*(4), 2220–2234. https://doi.org/10.1109/TGRS.2015.2497902

Yamada, T., Yukutake, Y., Terakawa, T., Arai R. (2015). Migration of earthquakes with a small stress drop in the Tanzawa Mountains, Japan. *Earth, Planets and Space*, 67 (175), https://doi.org/ 10.1186/s40623-015-0344-6

Yoshida, K., Hasegawa, A. (2018). Hypocenter Migration and Seismicity Pattern Change in the Yamagata-Fukushima Border, NE Japan, Caused by Fluid Movement and Pore Pressure Variation. *Journal of Geophysical Research: Solid Earth,* 123, 5000–5017. https://doi.org/10.1029/2018JB015468

Zebker, H. A., & Lu, Y. (1998). Phase unwrapping algorithms for radar interferometry: residue-cut, least-squares, and synthesis algorithms. *Journal of the Optical Society of America A*, *15*(3), 586. https://doi.org/10.1364/josaa.15.000586

Zwaan, F., Corti, G., Keir, D., & Sani, F. (2020a). A review of tectonic models for the rifted margin of Afar: implications for continental break-up and passive margin formation. *Journal of African Earth Sciences*, 103649. https://doi.org/10.1016/j.jafrearsci.2019.103649

Zwaan, F., Corti, G., Sani, F., Keir, D., Muluneh, A., Illsley-Kemp, F., & Papini, M. (2020b). Structural analysis of the Western Afar Margin, East Africa: evidence for multiphase rotational rifting. *Tectonics*, e2019TC006043. https://doi.org/10.1029/2019tc006043

Zwaan, F., Corti, G., Keir, D., Sani, F., Muluneh, A., Illsley-Kemp, F., Papini, M., (2020c). Geological data from the Western Afar Margin, East Africa. GFZ Data Services. http://doi.org/10.5880/fidgeo.2020.017